Probing the Cosmic Microwave Background : Maps and Noise Covariance Matrices

Sirviö, Anna-Stiina

University of Helsinki

2016-05-26

Sirviö , A-S 2016 , ' Probing the Cosmic Microwave Background : Maps and Noise Covariance Matrices ' , University of Helsinki , Helsinki . <
http://urn.fi/URN:ISBN:978-951-51-1583-6 >

http://hdl.handle.net/10138/233219

publishedVersion

UNIVERSITY OF HELSINKI REPORT SERIES IN PHYSICS

HU-P-D238

Probing the Cosmic Microwave Background — Maps and Noise Covariance Matrices

Anna-Stiina Suur-Uski

Department of Physics
Faculty of Science
University of Helsinki
Finland

ACADEMIC DISSERTATION

To be presented, with the permission of the Faculty of Science of the University of Helsinki, for public criticism in the Small Auditorium (E204) at Physicum, Gustaf Hällströmin katu 2A, Helsinki, on the 26th of May 2016 at 12 o'clock.

Helsinki 2016

ISBN 978-951-51-1582-9 (print)
ISSN 0356-0961
ISBN 978-951-51-1583-6 (pdf)
http://ethesis.helsinki.fi
Unigrafia Oy
Helsinki 2016

Contents

A.-S. Suur-Uski: Probing the Cosmic Microwave Background — Maps and Noise Covariance Matrices, University of Helsinki, 2016, 81 pages + appendices. University of Helsinki Report Series in Physics, HU-P-D238, ISNN 0356-0961, ISBN 978-951-51-1582-9 (printed version), ISBN 978-951-51-1583-6 (pdf version).
Keywords: cosmology, cosmic microwave background, Planck satellite, data analysis, map-making, noise covariance matrix

Abstract

The cosmic microwave background carries a wealth of cosmological information. It originates from the roughly 380,000-year-old Universe, and has traversed through the entire history of the Universe since. The observed radiation contains temperature anisotropies at the level of few times 10^{-5} across the sky. By mapping out these temperature anisotropies, and their polarisation over the full sky, we can unravel some fundamental mysteries of our Universe.

The cosmic microwave background was discovered by chance in 1965. Ever since the first discovery cosmologists have strived to measure its properties with increasing precision. The latest satellite mission to map the cosmic microwave background has been the European Space Agency's Planck satellite. Planck measured the cosmic sky for four years from 2009 to 2013 with unprecedented combination of sensitivity, angular resolution and frequency coverage. Planck's observations confirm the basic ΛCDM model, which is the most elementary model explaining the observed properties of the Universe.

As the precision of measurements has improved, the data volumes have grown rapidly. Modern-sized datasets require sophisticated algorithms to tackle the challenges in the data analysis. In this thesis we will discuss two data analysis themes: map-making and residual noise estimation. Specifically, we will answer the following questions: how to produce sky maps, and low-resolution maps with corresponding noise covariance matrices from the Planck Low Frequency Instrument data. The low-resolution maps and the noise covariance matrices are required in the analysis of the largest structures of the microwave sky.

The sky maps for the Stokes I, Q, and U components from the Planck Low Frequency Instrument data are built using the `Madam` map-maker. `Madam` is based on the generalised destriping principle. In the destriping the correlated part of the instrumental noise is modelled as a sequence of constant offsets, called baselines. Further, a generalised destriper is able to employ prior information on the instrumental noise properties to enhance the accuracy of noise removal. We achieved nearly optimal noise removal by destriping the data at the `HEALPix` resolution of $N_{\rm side} = 1024$ using 0.25 s baselines for the 30 GHz channel, and 1 s baselines for the 44 and 70 GHz channels — provided that a destriping mask, horn-uniform weighting and horn-uniform flagging was applied.

For the low-ℓ analysis we also provide maps at the resolution of $N_{\rm side} = 16$. These low-resolution maps were downgraded from the high-resolution maps using a noise-weighted downgrading scheme combined with the Gaussian smoothing for the temperature component. The resulting maps were adequate for the Planck 2015 data release, but for the final round of Planck data analysis the downgrading scheme will need to be revised.

The estimated maps will always contain some degree of residual noise. The analysis steps after the map-making, component separation and power spectrum estimation, require solid understanding of those residuals. We have three complementary methods at our disposal: half-ring noise maps, noise Monte Carlo simulations, and the noise covariance matrices. The half-ring noise maps characterise the residual noise directly at the map level, while the other

methods rely on noise estimates. The noise covariance matrices describe pixel-pixel correlations of the residual noise, and they are needed especially in the low-ℓ likelihood analysis. Hence, it is sufficient to calculate them at the highest feasible resolution of $N_{\rm side} = 64$, and subsequently downgrade them to the target resolution of $N_{\rm side} = 16$ using the same downgrading scheme as for the maps. The different residual noise estimates seem to show good agreement.

Acknowledgements

This thesis is based on research carried out in the Department of Physics at the University of Helsinki, and in the Helsinki Institute of Physics. I gratefully acknowledge the funding I have received from the Vilho, Yrjö, and Kalle Väisälä foundation, the Jenny and Antti Wihuri foundation, the Mikael Björnberg memorial fund and the Academy of Finland projects 121703 and 257989. The Magnus Ehrnrooth Foundation, the Chancellor's travel grant and the PAPU Doctoral programme are thankfully acknowledged for enabling my frequent travels. For computational resources, I thank CSC — the IT Center for Science Ltd. (Finland), the PRACE project, and NERSC — the National Energy Research Scientific Computing Center (USA).

The results in this thesis are based on observations obtained with Planck[1] satellite, an ESA science mission with instruments and contributions directly funded by ESA Member States, NASA, and Canada. I thank all the members of the Planck collaboration for the productive, interesting and enlightening years of working together.

As a member of the Planck team, I have had the pleasure of using both publicly and internally available software to enable my work. I especially thank Dr. Elina Keihänen for the `Madam` map-maker, and Dr. Reijo Keskitalo for providing the various tools used in the covariance matrix production. Throughout the work the `HEALPix` (Górski et al. 2005) package is used to either pixelise the maps, or to perform harmonic analysis of them. The Planck `Level-S` (Reinecke et al. 2015) simulation package and `TOAST` (Time Ordered Astrophysics Scalable Tools) have been used frequently, and the theoretical angular power spectra have been calculated with the `CAMB` software[2].

I wish to thank my supervisors, Dr. Hannu Kurki-Suonio and Dr. Elina Keihänen, for their guidance and support during my years in the Planck group. In the local Planck team I have also had the pleasure of collaborating with Dr. Reijo Keskitalo, Dr. Matti Savelainen, Dr. Jussi Väliviita, Kimmo Kiiveri and Valtteri Lindholm. Similarly, I would like to thank the pre-examiners of this thesis, Dr. Ingunn Kathrine Wehus and prof. Jonathan Sievers, for their careful reading of the manuscript.

I would also like to express my warmest thanks to my friends from various aspects of life. Your encouragement has been vital, especially during the frantic times of finalising the thesis. Further, I would like to thank my parents, Salme and Jarmo, and the entire extended family for their continuous support throughout my studies. Special thanks are due to my mother Salme and sister Eeva-Kaisa for their invaluable help — of which babysitting is not the least.

Finally, I would like to express my most sincere gratitude to Ville, Liina and *Pikkuveli*. You have, literally, grasped every opportunity to keep me in touch with the most important things in life. I love you.

Helsinki, May 2016

Anna-Stiina Suur-Uski

[1] `http://www.esa.int/Planck`
[2] `http://camb.info`

List of included publications

This PhD thesis contains six research papers and an introductory part describing the cosmic microwave background, the Planck satellite, and map-making along with the means of characterising residual noise in the map products.

I H. Kurki-Suonio, E. Keihänen, R. Keskitalo, T. Poutanen, A.-S. Sirviö, D. Maino, and C. Burigana,
Destriping CMB temperature and polarization maps,
Astron. Astophys. 506, 1511–1539 (2009)

II E. Keihänen, R. Keskitalo, H. Kurki-Suonio, T. Poutanen, and A.-S. Sirviö,
Making cosmic microwave background temperature and polarization maps with MADAM,
Astron. Astophys. 510, A57 (2010)

III A. Zacchei, D. Maino, C. Baccigalupi, et al.,
Planck early results V: The Low Frequency Instrument data processing,
Astron. Astophys. 536, A5 (2011)

IV Planck Collaboration: N. Aghanim, C. Armitage-Caplan, M. Arnaud, et al.,
Planck 2013 results. II. Low Frequency Instrument data processing,
Astron. Astophys. 571, A2 (2014)

V Planck Collaboration: P. A. R. Ade, N. Aghanim, M. Ashdown, et al.,
Planck 2015 results. II. Low Frequency Instrument data processing,
Accepted for publication in Astron. Astophys.,
DOI 10.1051/0004-6361/201525818 [arXiv:1502.01583]

VI Planck Collaboration: P. A. R. Ade, N. Aghanim, M. Ashdown, et al.,
Planck 2015 results. VI. LFI mapmaking,
Accepted for publication in Astron. Astophys.,
DOI 10.1051/0004-6361/201525813 [arXiv:1502.01585]

Author's contribution

Paper I: This paper extends the destriping principle to polarised data, and studies the residual error in output maps. The present author performed the necessary analysis for the section: Maps from shorter survey segments.

Paper II: This paper describes the `Madam` map-making code. The present author took part in the validation of the code, and polishing the paper.

Paper III: This paper describes the Planck Low Frequency Instrument data processing pipeline associated with the Early release. The present author was involved in the map-making, and performed the noise Monte Carlo simulations. The present author wrote the section on noise

Monte Carlo simulations.

Paper IV: This paper describes the Planck Low Frequency Instrument data processing pipeline associated with the 2013 data release. The present author took part in the map-making, was involved in the noise Monte Carlo simulations and was responsible for calculating the low-resolution products. The present author wrote the section about the low-resolution dataset, and produced the corresponding images. The present author also made the residual noise estimate comparison in figures 13 and 14.

Paper V: This paper describes the Planck Low Frequency Instrument data processing pipeline associated with the 2015 data release. The present author produced the low-resolution dataset.

Paper VI: This paper describes in detail the map-making procedure applied to the Planck Low Frequency Instrument data, already outlined in the paper [**V**]. The paper also illustrates the production of the low-resolution versions of the maps, and the corresponding noise covariance matrices. The present author was responsible for the production of the low-resolution dataset, and wrote the first version of the corresponding sections. The paper was polished jointly, and the present author was in charge especially of the images.

Chapter 1

Introduction

The Universe is intriguing. Countless generations before us have pursued to explain fundamentals about our Universe — its origin and fate. Further, literature is rich in culture-bounded symbolic narratives, one being the Finnish national epic Kalevala, portraying how the world came into existence. The Kalevala, compiled from our ancestors' oral folklore and mythology, depicts how the fragments of a teal's egg grow into the Earth and the heavenly bodies surrounding it:

One egg's lower half transformed
And became the earth below,
And its upper half transmuted
And became the sky above;
From the yolk the sun was made,
Light of day to shine upon us;
From the white the moon was formed,
Light of night to gleam above us;
All the colored brighter bits
Rose to be the stars of heaven
And the darker crumbs changed into
Clouds and cloudlets in the sky.

However, our thirst for knowledge about the Universe is not quenched by folklores, but rather by scientific research. The field of cosmology, the study of the Universe as a whole, seeks answers to questions such as: *How did the Universe begin? What is it made of? And how will it evolve?* Equally important is to ask: *How do we know?* This thesis, for one, aims to enlighten how we have gained the contemporary understanding of the Universe.

To do science we need observations and measurements. But how to study the beginning of the Universe? The key is the constancy of speed of light [1]. The light travels mere 299 792 458 meters per every second through space [2]. Thus, we see the Sun as it was eight minutes ago, and the Andromeda Galaxy as it was two million years ago. By extrapolating the idea, the oldest light in the Universe would simply originate from the infancy of the cosmos.

A faint glow of ancient light, the cosmic microwave background (CMB), was discovered by chance in 1965 [3, 4] — the year 2015, the International Year of Light, celebrated the jubilee of the major discovery. This relic radiation dates back to the roughly 380,000-year-old

Universe, and its detection is deemed to be one of the most vital discoveries in the field of physics during the twentieth century.

The CMB fills the entire sky and is remarkably isotropic — uniform in all directions. However, the existence of rich structures in the present day Universe lead to theoretical reasoning that the CMB should possess tiny temperature anisotropies [5, 6, 7]. The first detection of the anisotropies in 1992 [8] matched the importance of the initial discovery in 1965. The CMB is of fundamental significance to observational cosmology, as the early history of the Universe is imprinted in the radiation. It has enabled the shift of cosmology from a speculative discipline to precision science.

The radiation that once emerged as hot and bright as the surface of a star has travelled for about 13.8 billion years [9], the approximate age of the Universe. The Universe has, however, expanded [10, 11] by a factor of a thousand thereafter. The wavelength of the light has stretched, i.e. redshifted, with the expansion to microwave wavelengths. As the wavelength increases, the CMB cools to its present-day temperature of about 2.7 K above absolute zero [12].

With optical telescopes the background space between stars and galaxies appears completely dark. Thus, to detect the faint primordial light delicate instruments are needed, such as the European Space Agency's Planck satellite [13]. The Planck satellite measured the CMB for four years in chase of more subtle signatures — beyond the primordial temperature anisotropies — it carries. The ever increasing precision of measurements, however, drives the data volumes to grow rapidly. The modern-sized datasets require special care and sophisticated algorithms to tackle the challenges in the data analysis.

1.1 Objectives and scope

This thesis focuses, after a more general introduction to the field of CMB science and the Planck satellite, to a few specific data analysis themes: map-making and residual noise estimation. We will further limit ourselves to analysing the data from the Planck satellite's Low Frequency Instrument, as both instruments on board have a dedicated team to perform the data analysis. The present author has been an active member of the Planck Low Frequency Instrument Core Team.

This thesis will answer the following research questions.

1. How to produce the sky maps from the Planck Low Frequency Instrument data?

2. How to produce the low-resolution versions of the maps and corresponding noise covariance matrices, required in the analysis of the largest structures of the microwave sky, from the Planck Low Frequency Instrument data?

The included publications contain extended descriptions and explanations, and the main results are summarised with necessary motivations in the introductory part of the thesis. The articles can be divided into three categories, as illustrated in Figure 1.1. Paper **I** forms the basis for the thesis by studying the chosen map-making method, destriping, itself with polarised data, while papers **II** and partly **VI** discuss one particular implementation of the destriping algorithm, the `Madam` map-maker. Papers **III–V** and partly **VI** describe applications of the `Madam` map-maker to the actual measured data as an answer to the first research question. Papers **IV–VI** answer also to the second research question. The present author's task has not

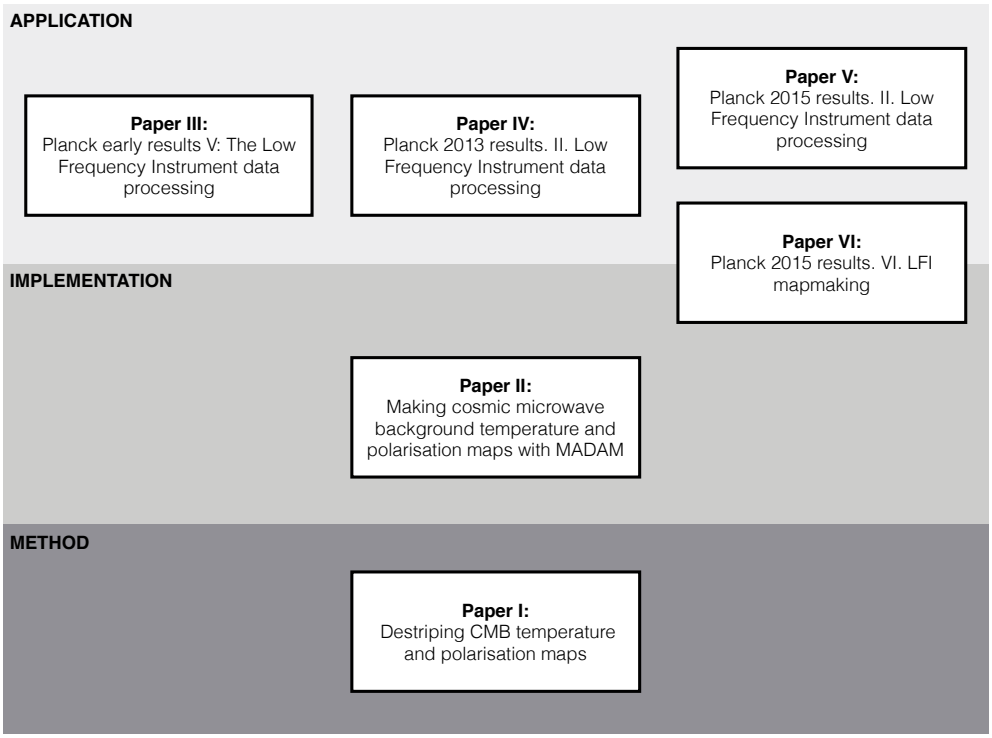

Figure 1.1: Article relations. Paper **I** forms a basis for the thesis by studying the destriping method with polarised data. Papers **II** and partly **VI** discuss one particular implementation of the destriping algorithm, the `Madam` map-maker. Papers **III**–**V** and partly **VI** put the methods into practice.

been to develop new map-making algorithms or implementations, but rather to validate, to improve and to apply them in practice.

1.2 Structure of the thesis

This thesis is organised as follows. In Chapter 2 we review the features of the CMB, and what information it carries about fundamental physics. Chapter 3 introduces the Planck satellite: both the spacecraft itself and the main results from the mission are discussed. Chapter 4 concentrates on the map-making, and hence mainly on the first and partly on the second research question. Chapter 5 covers how we model residual noise in maps, and answers to the noise modelling part of the second research question. In Chapter 6 we draw conclusions.

Chapter 2

Cosmic sky

Practically everything we know about the Universe derives from studying the light emitted or reflected by objects in space. The light reveals information about objects' chemical compositions, temperatures, and distances to name a few. However, only a fraction of the electromagnetic spectrum is visible to the human eye. While X-rays and gamma rays carry information about high energy phenomena, the longer wavelengths, from infrared to radio, unveil for example regions of star birth, cool dusty regions of space, and the cosmic microwave background radiation.

The CMB serves as an open window to the early Universe, since it provides the most direct observational link to the earliest times. As the light takes nearly 14 billion years to reach us, it additionally records information about the evolution and history of the Universe. In this Chapter we begin with an introduction to the standard model of cosmology and continue the discussion with the description of the CMB. We will review what the patterns of the CMB radiation reveal about fundamental physics, and at the same time motivate the field of CMB science. We will conclude with a brief discussion of astrophysical sources of microwave emissions and the pre-Planck status of observations.

2.1 Standard paradigm

The early Universe was hot, dense, and rapidly expanding [14, 15, 3]. Primordial plasma filled the Universe, and frequent scatterings maintained the photons and particles in a thermal equilibrium. As the Universe expanded – the evolution dictated by general relativity [16] – the temperature of primordial plasma fell.

When the Universe was a few minutes old, its temperature had fallen enough ($T \sim 10^9$ K) for the formation of nuclei of light elements. A process known as Big Bang Nucleosynthesis produced roughly 75 %[1] of ^{1}H, 25 % of ^{4}He, 10^{-4} % of ^{2}H, 10^{-4} % of ^{3}He and 10^{-9} % of ^{7}Li [17, 18, 19].

The Universe stayed completely ionised, and hence opaque, until the temperature was cold enough for the formation of neutral atoms. When the temperature had fallen to about 3000 K, hydrogen was finally formed. This era, roughly 380,000 years after the Big Bang, is known as either recombination, decoupling or last scattering. As the cosmic ionised gas, made

[1] Numbers are given as mass fractions of the total mass in ordinary matter.

of electrons and protons, combined to neutral hydrogen, there were no longer free charges to scatter the photons. The mean free path of photons rapidly increased, and the Universe became transparent. The stream of free photons is observed today as the cosmic microwave background [14, 20, 3, 4]. Due to the expansion of the Universe, the temperature of the CMB has decreased by a factor of 1100 to $T_0 = 2.725$ K today [12, 21]. A snapshot of the infant Universe is preserved in the CMB.

This picture forms the standard framework of modern cosmology, the Hot Big Bang model. The model stands on three solid observational foundations: the redshift of distant galaxies [15], the Big Bang Nucleosynthesis, and the cosmic microwave background. However, the model does not provide a valid description of the Universe all the way to the very beginning. Neither does it explain the initial state of the Universe, nor the origin of all the rich structures observable in the cosmos.

A period of an exponential expansion, called inflation, lasting a fraction of a second in the infant Universe was introduced to explain the initial conditions: flatness, homogeneity and isotropy of the Universe [22, 23, 24]. Inflation itself is not a physical theory but rather a generic idea about events occurring before the standard Hot Big Bang, without disturbing it. Additionally, inflation provides a source for the observed large scale structure [25, 26, 27]. Inflation stretched quantum fluctuations to macroscopic ones, and they were imprinted on the Universe as density fluctuations.

The small fluctuations in the initial conditions have evolved through gravitational instability to the complex non-linear structures in the present Universe. First galaxies and stars were forming after a few hundred million years [28]. They emitted intense radiation that reionised the surrounding Universe. This reionisation left a detectable signature in the CMB [29, 30].

To complete the standard picture of the Universe, we need two additional components: dark matter [31, 32, 19] and dark energy [33, 34, 19]. Dark matter is essential in aiding the structure formation, and dark energy is needed to explain the observed accelerated expansion of the late Universe. Dark matter, a nonstandard[2] form of matter, interacts only through gravity. It is thought to be cold, i.e. non-relativistic, at the era of structure formation. While dark energy could be either a new form of energy or a modification to general relativity, cosmologists tend to refer to it generically as dark energy.

All the above ingredients are combined to form the standard model of cosmology, the ΛCDM model. The Λ denotes cosmological constant, which is the simplest possible form of dark energy as its energy density remains constant both in space and time, and the CDM stands for cold dark matter. The ΛCDM model is the most elementary model, that explains rather well the observed properties of the Universe:

- the existence and structure of the CMB,
- the abundances of light elements,
- the large scale structure, and
- the accelerated expansion of the Universe.

Figure 2.1 illustrates a brief summary of the most important epochs in the cosmological standard model during the entire history of the Universe.

[2]Nonstandard in the particle physics sense.

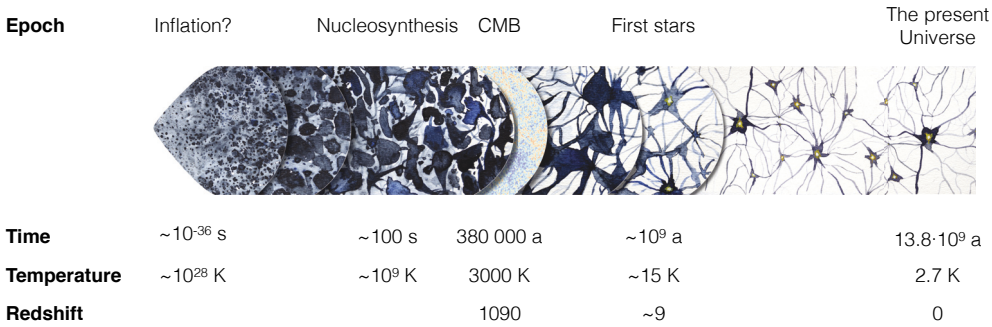

Figure 2.1: A brief history of the Universe. Figure is built on an image by European Space Agency.

2.2 Cosmic microwave background

The cosmic microwave background is a goldmine for cosmologists. Fundamental physics governing the evolution of the Universe imprints its subtle signatures on the radiation — and it is our mission to uncover its mysteries.

The CMB radiation is highly isotropic, uniform in all directions [3, 8]. This implies that everything in the observable Universe was in thermal equilibrium in the distant past. And furthermore, the observed CMB electromagnetic spectrum reveals that the Universe was still in thermal equilibrium at the time of photon decoupling, at redshift $z \sim 1100$. The CMB spectrum is well described with the thermal black-body function,

$$B_\nu(T_0) = \frac{2h\nu^3}{c^2} \frac{1}{e^{\frac{h\nu}{k_B T_0}} - 1}, \tag{2.1}$$

which has only one free parameter, the temperature today T_0, whose best fit value is 2.725 ± 0.001 K [12, 21]. The expansion of the Universe has shifted the temperature to colder values, but in the absence of non-equilibrium interactions the spectrum itself has not changed. However, the observed CMB radiation is only nearly, not perfectly, isotropic: across the sky, its temperature contains anisotropies at the level of few times 10^{-5} [8]. These minute differences reflect the lumpiness of the Universe at the time of last scattering, and are essential for the formation of complex structures in the later Universe. All these features — the electromagnetic spectrum, the isotropy, and the tiny temperature anisotropies — support the inflationary paradigm of accelerated expansion in the very early Universe. The extremely rapid expansion disconnected regions initially in causal contact and turned quantum fluctuations into nearly scale-invariant CMB inhomogeneities.

We begin with a description of primary temperature fluctuations that are intrinsic at the last scattering surface, and continue the discussion with the CMB's another property: polarisation. As secondary effects also process the CMB signal during the photon's journey to us, we introduce them in Section 2.2.4. We conclude the introduction to the CMB by summarising the cosmological parameters in Section 2.2.5.

2.2.1 Temperature anisotropy

At the time of decoupling, there are perturbations at each scale. However, the scales that are in causal contact, sub-horizon, behave differently than those which are super-horizon. The CMB anisotropies at super-horizon scales arise from gravitational redshifting of photons climbing out of potential wells at the last scattering surface, called the Sachs-Wolfe effect [5]. On smaller scales gravitational instability, seeded by the primordial perturbations, induce steadily growing perturbations in the gravitational potential dominated by the CDM. However, the photon pressure will try to push the compressed regions to re-expand. This sets up acoustic oscillations in the photon-baryon fluid. The state of the fluid at the time of decoupling is imprinted on the CMB as small-scale temperature anisotropies.

The temperature anisotropy $\delta T(\theta, \phi)$ forms a two-dimensional function on the sphere. Most commonly, these anisotropies are expressed as a spherical harmonic expansion,

$$\delta T(\theta, \phi) = \sum_{\ell=0}^{\infty} \sum_{m=-\ell}^{\ell} a^{\mathrm{T}}_{\ell m} Y_{\ell m}(\theta, \phi), \tag{2.2}$$

that isolates the contributions from different angular scales. Since the spherical harmonics $Y_{\ell m}$ form an orthonormal set of functions over the sphere, the multipole coefficients $a^{\mathrm{T}}_{\ell m}$ are obtained as

$$a^{\mathrm{T}}_{\ell m} = \int Y^{*}_{\ell m}(\theta, \phi) \delta T(\theta, \phi) \mathrm{d}\Omega. \tag{2.3}$$

The multipole ℓ describes the angular size of the anisotropy pattern, while the order m denotes its angular orientation. By examining the different multipoles separately, we can clarify their meaning.

- **Monopole**, $\ell = 0$. The CMB has a mean temperature of $T_0 = 2.72548 \pm 0.00057K$ K [12, 21, 35], which can be regarded as the monopole component of a CMB map. The monopole term in equation (2.2) must be $a^{\mathrm{T}}_{00} = 0$ for a quantity representing a deviation from average.

- **Dipole**, $\ell = 1$. The largest anisotropy is dominated by the Doppler shift caused by the solar system motion with respect to the last scattering surface. This solar dipole has an amplitude of 3.3645 ± 0.002 mK [36], and the underlying fainter cosmological dipole is difficult to extract. Hence, we are mostly interested in the $\ell \geq 2$ part of the expansion.

- **Higher order multipoles**, $\ell \geq 2$. The anisotropies at higher multipoles are mostly due to density perturbations in the early Universe, that are imprinted on the CMB at the last scattering surface. By measuring them we can, for example, constrain some key parameters describing our Universe. Some of the fundamental physics derivable from measuring these anisotropies are identified in Sections 2.2.3 and 2.2.4.

If the CMB anisotropy is from statistically isotropic Gaussian random fluctuations, all the statistical information in the CMB is fully characterised by its theoretical angular power spectrum

$$C_\ell \equiv \left\langle |a^{\mathrm{T}}_{\ell m}|^2 \right\rangle = \frac{1}{2\ell + 1} \sum_{m=-l}^{l} \left\langle |a^{\mathrm{T}}_{\ell m}|^2 \right\rangle, \tag{2.4}$$

where the angle brackets denote an ensemble average over skies with the same cosmology. Due to the isotropic nature of the random process generating the perturbations, there is no

preferred direction in the Universe, and the angular power spectrum is independent of m — only the angular scale of the anisotropy matters, not its orientation.

Equation (2.4) is then all we can predict from theory. However, we can only make observations from a single realisation of the random process, i.e. from our Universe observed from our location. The observed angular power spectrum can be defined as

$$\hat{C}_\ell = \frac{1}{2\ell+1}\sum_m |a^{\mathrm{T}}_{\ell m}|^2. \tag{2.5}$$

Its expectation value is equal to the theoretical one, $\left\langle \hat{C}_\ell - C_\ell \right\rangle = 0$, but the actual value is not. Cosmic variance,

$$\langle (\hat{C}_\ell - C_\ell)^2 \rangle = \frac{2}{2\ell+1} C_\ell^2, \tag{2.6}$$

poses a fundamental limit on determining the underlying theoretical power spectrum. The variance is smaller for higher ℓ, because for each ℓ we have $2\ell+1$ samples available. At large scales, i.e. small ℓ, the accuracy of constraints from the CMB observations is limited by the cosmic variance.

2.2.2 Polarisation

The CMB polarisation is a fundamental ingredient in any cosmological model [37]. The presence of temperature anisotropies and free electrons at the last scattering surface will polarise the radiation, since the Thomson scattering thermalising the primordial plasma has a polarisation-dependent differential cross-section [38],

$$\frac{d\sigma}{d\Omega} \propto |\hat{\epsilon}_{\mathrm{in}} \cdot \hat{\epsilon}_{\mathrm{out}}|^2, \tag{2.7}$$

where $\hat{\epsilon}_{\mathrm{in}}$ and $\hat{\epsilon}_{\mathrm{out}}$ are the incident and scattered polarisation directions. The scattered radiation intensity peaks when $\hat{\epsilon}_{\mathrm{in}} \parallel \hat{\epsilon}_{\mathrm{out}}$, i.e. in the direction parallel to the incident polarisation, and is non-existent when $\hat{\epsilon}_{\mathrm{in}} \perp \hat{\epsilon}_{\mathrm{out}}$.

Figure 2.2 illustrates incoming rays from two directions. The electromagnetic field oscillates transversely to the direction of wave propagation $\boldsymbol{k}$. Scattering allows all radiation polarised perpendicularly to both the incoming and outgoing directions to pass trough completely, while blocking any radiation polarised parallel to the outgoing direction. If the incident radiation is isotropic or has only a dipolar temperature variation, the scattered light would be unpolarised, as the intensity along the two transverse directions are equal. However, if the incident radiation has a quadrupolar temperature pattern, i.e. the incident radiation from perpendicular directions have different intensities, the scattering would result in a net polarisation aligned with the direction of cold spots. Quadrupole anisotropy around the scattering centre will lead to linear polarisation, even if the incident radiation is unpolarised.

The temperature anisotropy has two distinct sources: scalar and tensor perturbations [39]. The scalar perturbations of the spacetime metric are primordial density perturbations, while the tensor perturbations of the metric are gravitational waves. In consequence, the CMB polarisation is also sourced by both the scalar and the tensor perturbations. For scalar perturbations the local temperature quadrupole develops when photons decouple from electrons, just before the last scattering. If the transition from opaque to transparent Universe happens instantaneously, the temperature quadrupole would have no time to form, and no CMB polarisation would emerge. The local quadrupole anisotropy arises from velocity gradients as

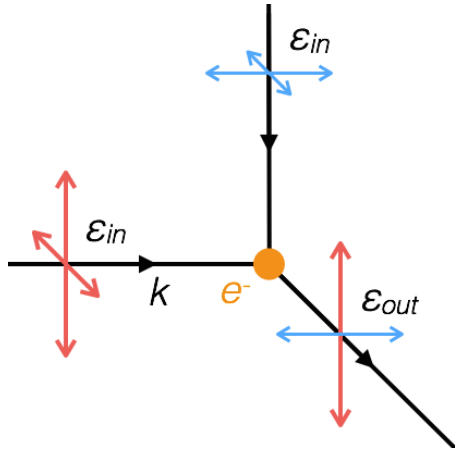

Figure 2.2: Generation of CMB polarisation. Quadrupole temperature anisotropy at the last scattering surface generates linear polarisation through Thomson scattering. Red lines represent radiation from hot spots and blue lines from cold spots. The resulting polarisation is in the direction of cold spots.

the photon-baryon fluid tends to compress in over dense regions, while the radiation pressure pushes the high-density regions to re-expand. On the other hand, the primordial gravitational waves, presumably generated during inflation, stretch and squeeze space in orthogonal directions, as illustrated in Figure 2.3. They serve as a natural source of temperature quadrupoles. Both kinds of perturbations predict slightly different polarisation patterns, which can be distinguished and studied with detailed measurements.

The polarisation signal and its cross-correlation with temperature anisotropies provide a crucial consistency check for the ΛCDM model. Moreover, as the scattering of photons from free electrons is a necessity for the CMB polarisation, its generation is well localised in time. Hence, by measuring the CMB polarisation, we can directly probe the last scattering events.

Polarisation Observables

The polarisation state of light is completely described by the Stokes parameters: I, Q, U, and V [38]. The I parameter is the total intensity, and Q and U describe linear polarisation, while V measures the circular polarisation. In cosmology the primordial $V = 0$, since the Thomson scattering is unable to generate circular polarisation. In terms of the Stokes Q and U parameters, polarisation amplitude P and direction α are given as

$$\begin{aligned} P &= \sqrt{Q^2 + U^2}, \text{ and} \\ \alpha &= \frac{1}{2}\tan^{-1}\left(\frac{U}{Q}\right). \end{aligned} \tag{2.8}$$

The Q and U Stokes parameters are coordinate-dependent quantities. In a coordinate rotation by an angle ψ they transform as

$$\begin{aligned} Q' &= Q\cos(2\psi) + U\sin(2\psi), \text{ and} \\ U' &= -Q\sin(2\psi) + U\cos(2\psi). \end{aligned} \tag{2.9}$$

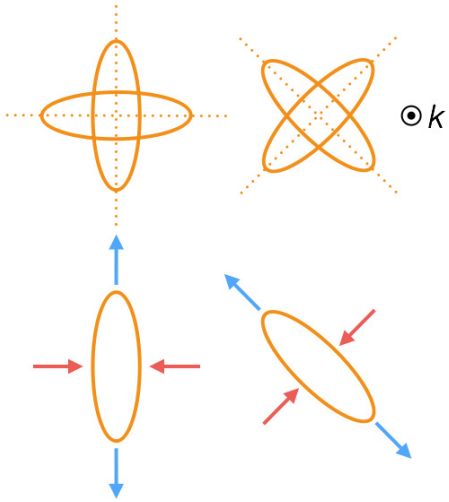

Figure 2.3: *Top row:* The two modes $(+, \times)$ of gravitational waves. *Bottom row:* A gravitational wave induces a temperature quadrupole by stretching (redshifting) and compressing (blueshifting) space in perpendicular directions.

Equation (2.8) implies that the polarisation amplitude P is invariant under rotation, while the angle α transforms to $\alpha - \psi$ defining a constant orientation of the polarisation. The transformation rules of equation (2.9) can be written in a more concise form as

$$(Q \pm iU)'(\theta, \phi) = e^{\mp i2\psi}(Q \pm iU)(\theta, \phi), \tag{2.10}$$

suggesting that $Q \pm iU$ form spin-2 fields on the sphere. We expand them in terms of the spin-2 spherical harmonics, ${}_{\pm 2}Y_{\ell m}(\theta, \phi)$, forming a complete and orthonormal system of tensor functions on the sphere, as in [40],

$$(Q \pm iU)(\theta, \phi) = \sum_{\ell \geq 2} \sum_{m=-\ell}^{\ell} a_{\pm 2, \ell m} \, {}_{\pm 2}Y_{\ell m}(\theta, \phi). \tag{2.11}$$

An alternative approach using tensor harmonics has been presented in [41]. Although the formalism used there differs notably from ours, the results in the end are naturally equivalent. We can further decompose the polarisation field into curl-free and divergence-free parts, called E- and B-mode, respectively:

$$\begin{aligned} E(\theta, \phi) &= \sum_{\ell \geq 2} \sum_{m=-\ell}^{\ell} a^E_{\ell m} Y_{\ell m}(\theta, \phi), \\ B(\theta, \phi) &= \sum_{\ell \geq 2} \sum_{m=-\ell}^{\ell} a^B_{\ell m} Y_{\ell m}(\theta, \phi), \end{aligned} \tag{2.12}$$

where

$$\begin{aligned} a^E_{\ell m} &= -\frac{1}{2}(a_{2, \ell m} + a_{-2, \ell m}), \\ a^B_{\ell m} &= \frac{i}{2}(a_{2, \ell m} - a_{-2, \ell m}). \end{aligned} \tag{2.13}$$

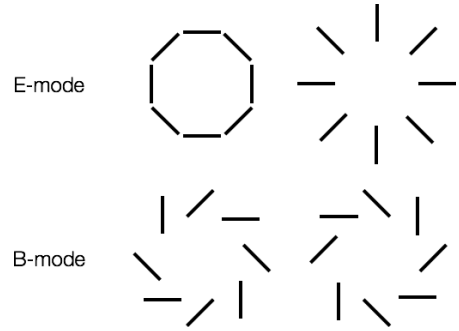

Figure 2.4: Typical E- and B-mode polarisation patterns. The E-mode is either radial or tangential, while the B-mode has a curly pattern. The B-mode is not invariant under reflections.

The E- and B-modes are more fundamental than the polarisation Q and U fields on the sky. Both polarisation modes have characteristic patterns on the sky, as illustrated in Figure 2.4. The E-mode is characterised with radial or tangential polarisation vectors, while the B-mode polarisation vectors have vorticity. The E-mode polarisation is observed to be directed radially around temperature cold spots and tangentially around temperature hot spots [42]. As Figure 2.4 implies, the two modes behave differently under parity transformations: the E-mode remains unchanged whereas the B-mode changes sign. Also the primordial scalar perturbations cannot produce B-mode polarisation, as long as the perturbations evolve linearly. Only gravitational waves, in the linear theory, can generate primordial B-mode polarisation. Due to its origin, the B-mode may contain unique information about the inflationary era of the Universe.

2.2.3 Angular power spectra

To characterise fully the statistics of the Gaussian CMB perturbations only four angular power spectra are needed: C_ℓ^{TT}, C_ℓ^{EE}, C_ℓ^{BB} and C_ℓ^{TE}. The angular power spectra are defined as

$$C_\ell^{XY} = \frac{1}{2\ell+1} \sum_{m=-\ell}^{\ell} \left\langle a_{\ell m}^{X*} a_{\ell m}^{Y} \right\rangle, \tag{2.14}$$

where $X, Y = T, E, B$. The C_ℓ^{TB} and C_ℓ^{EB} cross-spectra are expected to vanish due to parity conservation. Examples of the theoretical angular power spectra for a set of parameters describing the cosmological standard model is illustrated in Figures 2.5 and 2.6.

The peaks and troughs in the angular power spectra reveal the underlying physics of oscillating sound waves in the coupled baryon-photon fluid driven by the dark matter perturbations. Apart from competing gravitation and radiation pressures inducing the sound waves in the fluid, other effects giving rise to unique signatures in the spectra are inflation, baryon density, and photon diffusion to name a few. Inflation establishes the amplitude and tilt of the spectrum, while the asymmetry in the peak heights of odd and even peaks is mostly accounted by baryon density. Photon diffusion, on the other hand, causes exponential damping of the oscillatory pattern at high ℓ [6].

The horizon scale at decoupling extends roughly 1° on the sky. Only smaller regions had time to compress, and hence we expect to see a peak in the TT spectrum at a corresponding

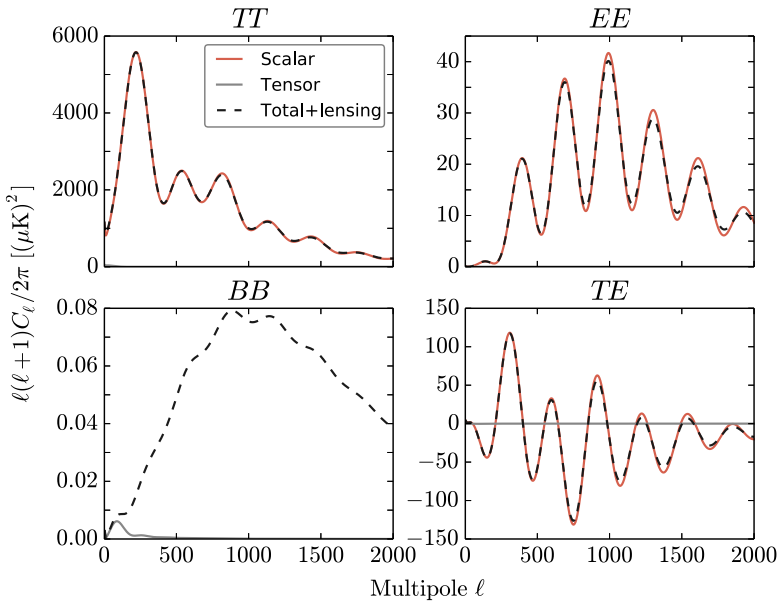

Figure 2.5: Four observable angular power spectra calculated using the publicly available code `CAMB` (`http://camb.info`) for a set of cosmological parameters ($\tau = 0.09$ and $r = 0.1$). Angular power spectra due to scalar perturbations are plotted in red, tensor perturbations in grey, and their combination with additional effect from gravitational lensing in black (dashed line).

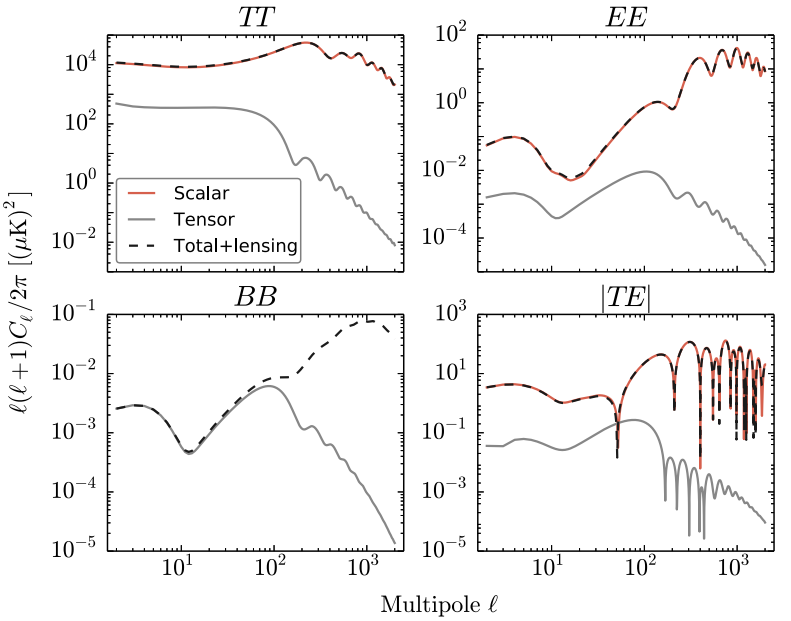

Figure 2.6: Same as in Figure 2.5, but plotted in logarithmic scale. Since the TE spectrum contains both positive and negative values, we illustrate its absolute values.

scale. Anisotropies at larger scales did not have time to evolve substantially revealing the initial conditions, the Sachs-Wolfe Plateau, at $\ell \lesssim 100$ corresponding to almost scale-invariant perturbations. The position of the first TT peak also reveals the flat geometry of the Universe. The intermediate and high multipoles show the acoustic peaks and damping tail. On sufficiently small scales the photon-baryon fluid underwent acoustic oscillations giving rise to the distinct shape of the power spectrum. Because of photon diffusion, however, the oscillatory pattern does not keep up without a bound. Polarisation EE spectrum is seen to peak at higher ℓ values and to anti-correlate with TT: between every peak in the TT there is one in the EE, and between the TT and EE peaks there is one for TE. This is because the polarisation anisotropies are sourced by the fluid velocity. The BB spectrum is expected to peak around the horizon scale at decoupling, and to be damped on scales $\ell \gtrsim 100$.

2.2.4 Secondary anisotropies

En route from the last scattering surface, the CMB signal is processed due to both scattering events and gravitational effects. With ever increasing precision of measurements, these secondary anisotropies allow us to unravel puzzles of the evolving Universe at $z \ll 1000$. We will briefly consider effects including the Sunyaev-Zel'dovich effect, reionisation, integrated Sachs-Wolfe effect and gravitational lensing.

The Sunyaev-Zel'dovich effect

The Sunyaev-Zel'dovich effect (SZ) arises from the Compton scattering of the CMB photons by hot electron gas in galaxy clusters [43, 44]. The scattering creates a distinct spectral distortion by transferring energy from the electrons to photons. The shift in the CMB temperature is of the form

$$\frac{\Delta T}{T} = y f(x), \tag{2.15}$$

with the Compton y-parameter being $y = \int_{\text{l.o.s}} \mathrm{d}l \sigma_{\mathrm{T}} n_e \frac{k_{\mathrm{B}} T_e}{m_e c^2}$, and function $f(x) = x \coth(\frac{x}{2}) - 4$ describes the frequency dependence, since $x = \frac{h\nu}{k_{\mathrm{B}} T_{\mathrm{CMB}}}$ [45]. Here σ_{T} is the Thomson cross-section, n_e is the electron number density, T_e is the electron temperature, k_{B} is the Boltzmann constant, $m_e c^2$ is the electron rest mass energy, and the integration is along the line of sight. The temperature distortion vanishes at a frequency of $\nu = 217$ GHz for the measured CMB temperature, $T_{\mathrm{CMB}} = 2.725$ K [46]. Hence, below 217 GHz the SZ effect produces a temperature decrement and above an increment. An additional temperature shift, the kinetic SZ effect, arises from the bulk motion of the cluster, that is typically smaller than the thermal SZ effect [45].

The thermal SZ effect can be used, for example, to detect individual galaxy clusters, and to constrain some cosmological parameters such as the equation of state of the dark energy and the Hubble constant. It is especially powerful in the search for new galaxy clusters, since the temperature shift is redshift independent.

Reionisation

As the initially small inhomogeneities in the Universe grow to the first highly nonlinear gravitationally collapsed regions, the first generation of stars and quasars, their intense radiation reionises the neutral hydrogen almost completely. Once again there are free electrons that

scatter the CMB photons. The effect of reionisation on the CMB is visible both at small angular scales, where it attenuates both the temperature and polarisation anisotropies, and at large angular scales, where it is another source of polarisation [47]. Reionisation will enhance the TE, EE and BB spectra at the lowest ℓ values, seen as bumps at scales $\ell < 10$ in Figure 2.6. These signatures will allow the measurement of the optical depth τ, the expectation value of how many times a CMB photon scatters between the decoupling and today, and the search for primordial gravitational waves.

Integrated Sachs-Wolfe effect

The ordinary Sachs-Wolfe effect [5] arises from the gravitational redshift at the last scattering surface: photons released from either under- or over-dense regions fall down potential hills or climb out of potential wells, while gaining or losing energy. This is manifested as blue- or redshifted photon wavelengths, respectively. Whereas the integrated Sachs-Wolfe (ISW) effect [5, 48, 49] originates from the temporal variation of the gravitational potentials along the line of sight. A decaying potential well induces a temperature increment for a CMB photon traversing through a supercluster, and conversely a deepening potential will lead to a temperature decrement. Accelerated expansion due to the dark energy in the late Universe causes potential wells (superclusters) and hills (voids) to decay giving rise to the ISW contribution at large angular scales, seen as a modest rise in Figure 2.6 at the smallest multipoles in the TT spectrum (scales $\ell < 10$). The ISW effect can be used to test the growth of structures in the Universe, the nature and evolution of dark energy, and the theory of general relativity.

Gravitational lensing

Gravitational lensing affects both the temperature and polarisation fields. Inhomogeneities particularly at the late Universe distort the appearance of the CMB, as predicted by general relativity. The bending of light implies that one is not looking exactly at the point on the last scattering surface one assumes. Lensing does not generate new temperature anisotropy, but merely shifts the existing fluctuations around. On the temperature and E-mode polarisation power spectra, it will leave the lowest multipoles unchanged, while smoothing the acoustic peak structure on intermediate to small scales and creating power at the smallest scales [50]. Lensing will have the largest effect on the polarisation B-mode, since even though it preserves the brightness of the radiation, it does not preserve the nature of E- and B-modes. The lensing will result in a shift of power from E to B at scales $\ell > 100$ [50], shown as a large bump in the BB spectrum in Figure 2.5. The CMB maps can be used to reconstruct the intervening matter distribution via the lensing effect [51].

2.2.5 Cosmological parameters

The CMB anisotropy pattern is determined by the physics at decoupling, and it is processed as the CMB travels through the Universe. Accordingly, the shape of the angular power spectra depends on cosmological parameters. The state-of-the-art cosmological data are adequately fitted by only a handful of independent parameters [52, 9], while others are either fixed at their natural values or derived from the independent ones.

Conventionally, the cosmological standard model is parametrised with just six basic parameters, and the Universe is fixed to be spatially flat [53, 19]. Four of them (A_s, n_s, ω_b, and ω_m) characterise the physics at decoupling, while two others (Ω_Λ and τ) describe the

post-decoupling Universe. These independent parameters are summarised in Table 2.1, along with their possible physical origin. Their values are mostly not predicted by the current theories. For example, the relative fractions of baryons, dark matter and dark energy are governed by the physics beyond the Standard Model of particle physics. Table 2.1 also lists the fixed parameters and a few examples of the derived parameters.

The chosen set of cosmological parameters is neither unique nor is their number fixed. For the ΛCDM model different choices of parameters are possible within the 6-dimensional parameter space. But care must be taken, since different variables may affect the CMB features in a similar way. Such parameters are called degenerate. Increase in the data quality and volume will allow to extend the parameter space in the future. Some of the possible directions for extensions are the currently fixed parameters along with a few extended parameters listed in Table 2.1. A number of the extended parameters relate to the inflationary era, hence ever tighter constraints on them will allow us to rule out classes of inflationary models. Including additional variables in the parameter estimation will generally increase their uncertainties and may shift parameter values slightly.

2.3 Foregrounds

Until now, we have only discussed the CMB, which is packed with cosmological information. But when observing the sky at microwave frequencies, there are also other significant sources of radiation: the Milky Way and other galaxies beyond our own. These foregrounds set a challenge to our thirst for understanding the primordial Universe. As the CMB originates beyond all other light sources, we must acknowledge that the background signal we are interested in could well be smaller than the contaminating foreground signals.

Galactic foregrounds

The main source of foreground contamination arises from our galaxy. Three distinct mechanisms have been identified: dust emission, synchrotron radiation and free-free emission [54, 55, 56, 57].

- **Dust emission.** Interstellar dust consisting of small matter particles of various shapes and sizes (from a few nm to some μm) emit thermal grey-body[3] radiation that is dominant at higher frequencies ($\nu > 100$ GHz). Properties of the dust emission is determined by the grain size and dust temperature. The intensity is modelled as a power law $T \propto T_0 \nu^\beta$ within the observed range of frequencies, with the temperature T_0 and spectral index $\beta \approx 2$ varying over the sky. Observations also suggest the presence of another dust correlated emission at frequencies below 30 GHz that could derive from spinning dust grains. The dust emission is slightly polarised.

- **Synchrotron radiation.** Relativistic cosmic-ray electrons spiralling in magnetic fields emit synchrotron radiation that is a major contaminant at lower frequencies ($\nu < 70$ GHz). The intensity is modelled as a power law $T \propto \nu^{-\beta}$, with a position and frequency dependent spectral index that varies between 2 and 3. The galactic magnetic field breaks the local spatial isotropy, i.e. the galactic field specifies a direction at each location,

[3] Grey-body radiation has a similar spectrum as black-body radiation, but with lower emissivity ($\epsilon \leq 1$). Thus a grey-body absorbs and emits less energy than a black-body at the same temperature.

Table 2.1: Cosmological parameters. The parameters labelled *independent* define the minimal set of parameters, whose measured values characterise the observed Universe. Since the present-day data is not yet descriptive enough to constrain further variables, they are kept *fixed* at their natural values. Using the independent and fixed parameters one can determine values of the *derived* parameters. In the future, the parameter space of the cosmological standard model is likely to be *extended* beyond the six basic parameters, or by letting the fixed parameters to vary.

	Label	Definition	Physical Origin
Independent	A_s	Amplitude of scalar perturbations[a]	Inflation
	n_s	Spectral index of scalar perturbations	Inflation
	ω_b	Physical baryon density[b]	Baryogenesis
	ω_m	Physical matter density[c]	Beyond-SM physics
	Ω_Λ	Cosmological constant	Unknown
	τ	Optical depth[d]	First stars
Fixed	Ω_0	Total density parameter[e]	Inflation
	$\frac{\mathrm{d}n_\mathrm{s}}{\mathrm{d}\ln k}$	Scale dependence of the spectral index[f]	Inflation
	r	Relative amplitude of tensor perturbations[g]	Inflation
	w	Dark energy equation of state parameter[h]	Unknown
Derived	H_0	Hubble constant	Cosmological epoch
	t_0	Age of the Universe	Cosmological epoch
Extended	$\sum m_{\nu_i}$	Neutrino masses	Beyond-SM physics
	n_T	Spectral index of tensor perturbations	Inflation
	f_NL	Non-Gaussianity	Inflation

[a] The primordial density perturbation power spectrum is parametrised by $A_\mathrm{s}(k/k_*)^{n_\mathrm{s}-1}$, where k_* is a chosen reference scale.

[b] Physical density, $\omega_i \equiv \Omega_i h^2$, is the density parameter Ω_i multiplied by the square of the reduced Hubble constant h. The density parameter is defined as $\Omega_i \equiv \rho_i/\rho_\mathrm{c}$, i.e. density ρ_i divided by the critical density $\rho_\mathrm{c} = 3H_0^2/8\pi G$. The reduced Hubble constant is defined by the equation $H_0 = 100h$ (km/s)/Mpc.

[c] The physical matter density is the sum of physical baryon and dark matter densities, $\omega_\mathrm{m} = \omega_\mathrm{b} + \omega_\mathrm{cdm}$.

[d] The optical depth gives the expectation value of how many times a CMB photons scatters between the decoupling and today.

[e] The total density parameter, $\Omega_0 = \Omega_\mathrm{m} + \Omega_\Lambda$, is fixed to $\Omega_0 = 1$.

[f] The scale dependence of spectral index, running of the spectral index, is fixed to $\frac{\mathrm{d}n_\mathrm{s}}{\mathrm{d}\ln k} = 0$.

[g] The relative amplitude of tensor perturbations, $r = A_\mathrm{T}/A_\mathrm{s}$, where A_T is the amplitude of tensor perturbations, is fixed to $r = 0$.

[h] The dark energy equation of state parameter is fixed to $w = -1$ implying the case of the cosmological constant.

leading to polarised synchrotron radiation. Theoretically, a high degree of polarisation is expected.

- **Free-free emission.** Free-free emission, or more commonly know as bremsstrahlung, arises from electron-ion scattering. The name free-free refers to the unbound state of the incoming and outgoing electron. The ions decelerate free electrons leading to thermal radiation. The intensity is modelled as a power law $T \propto \nu^{-\beta}$, with spectral index $\beta \approx 2$. Free-free emission does not dominate at any frequency, but is most evident at lower frequencies. Free-free emission is not anticipated to be polarised, because the scattering directions are random.

Extra-galactic point sources

In addition to the galactic foregrounds, extragalactic point sources affect the CMB anisotropy data. Point sources are objects whose angular size is much smaller than the angular resolution of the experiment, therefore they appear in the data as point-like objects convolved with the beam of the instrument. Known point sources are well-localised contaminants and easily removable from the maps, but care must be taken with unresolved ones. Point sources influence the CMB measurements at high angular scales and low frequencies, and do not significantly contaminate polarisation measurements [56, 58].

2.4 Status of observations before Planck

Ever since the initial discovery of the cosmic microwave background by Penzias and Wilson in 1965 [3], there has been intense activity to probe the cosmic microwave sky in greater detail. Shortly after the first report was out, the hunt for characterising the CMB spectrum and its anticipated anisotropies began. The CMB dipole was only, however, verifiably detected in the 1970s [59, 60, 61], and the conclusive evidence for the thermal CMB spectrum and the higher order anisotropies flooded in as late as 1990 and 1992, respectively, from the NASA Cosmic Background Explorer (COBE) [62] observations [12, 8]. The first anisotropy measurements were later supported and complemented by the results from number of ground-based and balloon-borne experiments [63, 64, 65] as well as by the first results from the NASA Wilkinson Microwave Anisotropy Probe (WMAP) [66] in 2003 [67]. These were subsequently revised by the analysis of the 3- to 9-year WMAP data [68, 69, 70, 71], and supplemented by small scale experiments such as the Atacama Cosmology Telescope (ACT) [72] and the South Pole Telescope (SPT) [73]. All these missions not only unveiled the temperature anisotropies with high precision, but also the tiny polarisation signal first detected by the Degree Angular Scale Interferometer (DASI) in 2002 [74].

The Far Infrared Absolute Spectrophotometer (FIRAS) instrument onboard the COBE satellite measured the CMB spectrum with unprecedented accuracy. The observations are well fitted by a black-body function with temperature [12, 21, 35]

$$T_0 = 2.72548 \pm 0.00057\,\mathrm{K}. \tag{2.16}$$

Additionally, any deviations from the thermal spectrum have very stringent limits according to the FIRAS findings [75]. No other satellite mission, since the COBE measurements in the early 1990s, has re-examined the CMB spectrum, which would open a fascinating window to the early Universe. The Primordial Inflation Explorer (PIXIE) [76] is one of the proposed

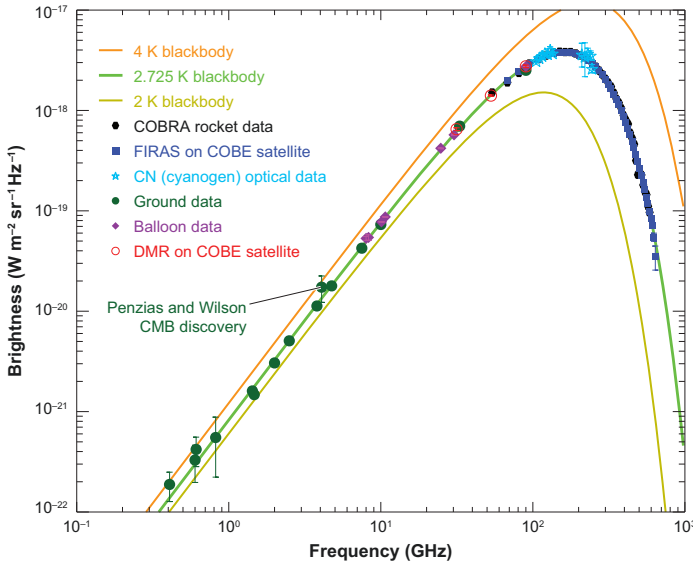

Figure 2.7: The CMB spectrum: measured flux as a function of frequency. Theoretical black-body curves are superimposed for $T = 2$ K, $T = 2.725$ K, and $T = 4$ K. The figure is reproduced from [56].

satellites to probe the CMB spectrum in greater detail. Figure 2.7 displays the CMB spectrum data to date, and it is in remarkable agreement with the theoretical black-body spectrum.

The WMAP 9-year data served as the state-of-the-art dataset for the CMB anisotropy measurements before the Planck data releases. Figure 2.8 illustrates the WMAP 9-year temperature and polarisation amplitude maps over the full sky for each five frequency bands. The slightly warmer regions in the temperature maps are depicted with reddish colours, while the slightly cooler regions have bluish tones. The colour scale of the polarisation maps, on the other hand, runs from negligible polarisation in the blue end of the scale to moderate in the red end. The CMB appears as the mottled background in the temperature maps, while the polarisation maps show hardly any CMB polarisation. The bright Milky Way clearly dominates all map images in the Galactic plane. In the WMAP 9-year analysis the Galactic foregrounds are decomposed into the synchrotron, the free-free, the thermal dust, and the spinning dust like components for the temperature measurements [52], whereas for the polarised foregrounds its enough to take into account the synchrotron and the thermal dust emissions [77]. There still remains room for experimental and theoretical improvements alike to gather a more profound understanding of the foregrounds and their impact on the CMB research. The full sky CMB map constructed from the WMAP 9-year data is shown in Figure 2.9 revealing the tiny temperature fluctuations originating from the early Universe.

Figure 2.10 unveils the pre-Planck understanding of the angular power spectra. The TT spectrum is most evidently outlined by the WMAP 9-year data combined with the ACT and SPT results, while the TE and EE power spectra are formed by data from numerous experiments, including WMAP and QUaD[4] [78]. Every spectrum features rather apparently several

[4]QUaD stands for QUEST (QU Extragalactic Survey Telescope) at DASI (Degree Angular Scale Interferometer).

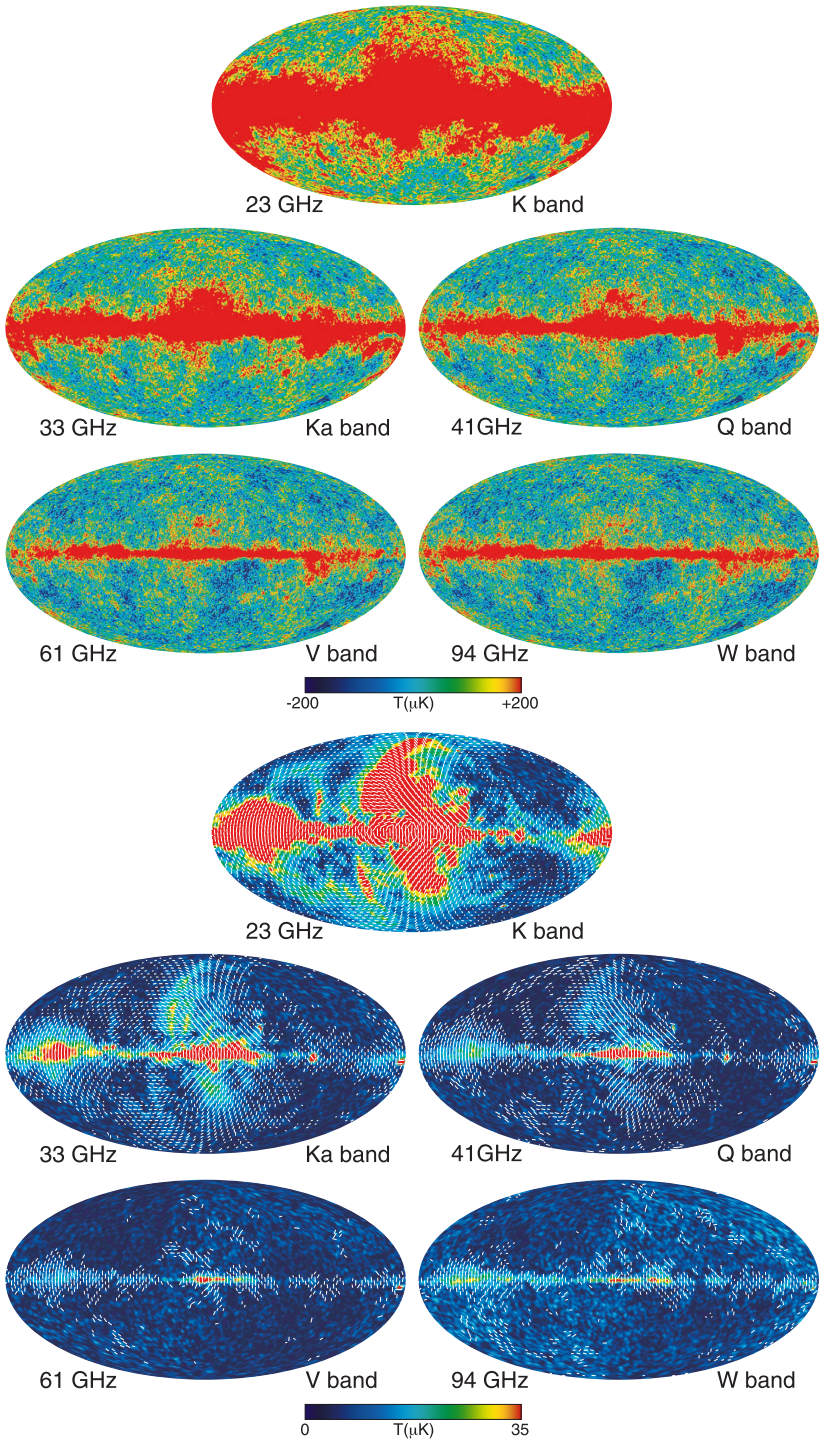

Figure 2.8: WMAP 9-year temperature (*upper*) and polarisation amplitude $P = \sqrt{Q^2 + U^2}$ (*lower*) maps in Galactic coordinates shown with a Mollweide projection. The temperature and the polarisation maps have been smoothed with 0.2° and 2.0° Gaussian beams, respectively. The faint white lines in the lower maps show polarisation angles for `HEALPix` $N_{\rm side} = 16$ pixels where the signal-to-noise exceeds 1. The figures are reproduced from [52].

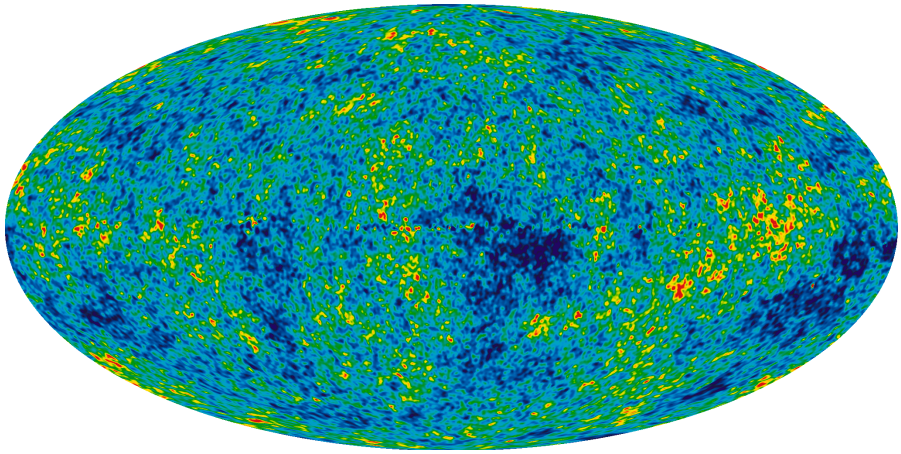

Figure 2.9: The CMB map constructed from the WMAP 9-year data. The image reveals temperature fluctuations at ±200 μK scale, shown as colour differences. Image: NASA/WMAP Science Team.

peaks and throughs caused by the acoustic oscillations before the photon decoupling, and the TE anti-correlation, as expected in the cosmological standard model, is fairly visible. As shown in [52], the TE spectrum reveals some excess signal at the lowest multipoles ($\ell < 10$) compared to expectations from the temperature only analysis showing evidence for the early reionisation.

As the polarisation anisotropies are very weak and demanding to measure, only upper limits on the underlying BB spectrum existed. The first indications of the lensing BB signal came from the SPT [79] in 2013, and later from POLARBEAR [80, 81]. The first controversial claims of the direct detection of the BB power spectrum were released by the BICEP2 [82] collaboration in 2014 [83].

The most robust constraints for the cosmological parameters, before any Planck cosmology data was released, could be derived from the WMAP 9-year observations. The data were fitted well with the simplest six-parameter model, the ΛCDM model, for which we list the best-fit values in Table 2.2 [71]. The dataset did not show any convincing evidence for deviations from the ΛCDM model, and was compatible with various other cosmological datasets [71]. According to the observations, the Universe is comprised of ordinary matter (4.6 ± 0.1%), dark matter (24.0 ± 0.9%) and dark energy consistent with cosmological constant (71.4 ± 1.0%). The geometry of the Universe is flat within the limits of the observations, and it is roughly 13.77 ± 0.06 billion years old. The primordial fluctuations were found to be Gaussian and adiabatic with a slight power-law scale dependence in agreement with the simplest models of inflation.

Throughout the years, the continuous improvements in the quality of CMB data has ultimately provided a firm footing for the standard model of cosmology. In combination with other astrophysical data, the CMB anisotropy measurements have been able to constrain cosmological parameters with high accuracy.

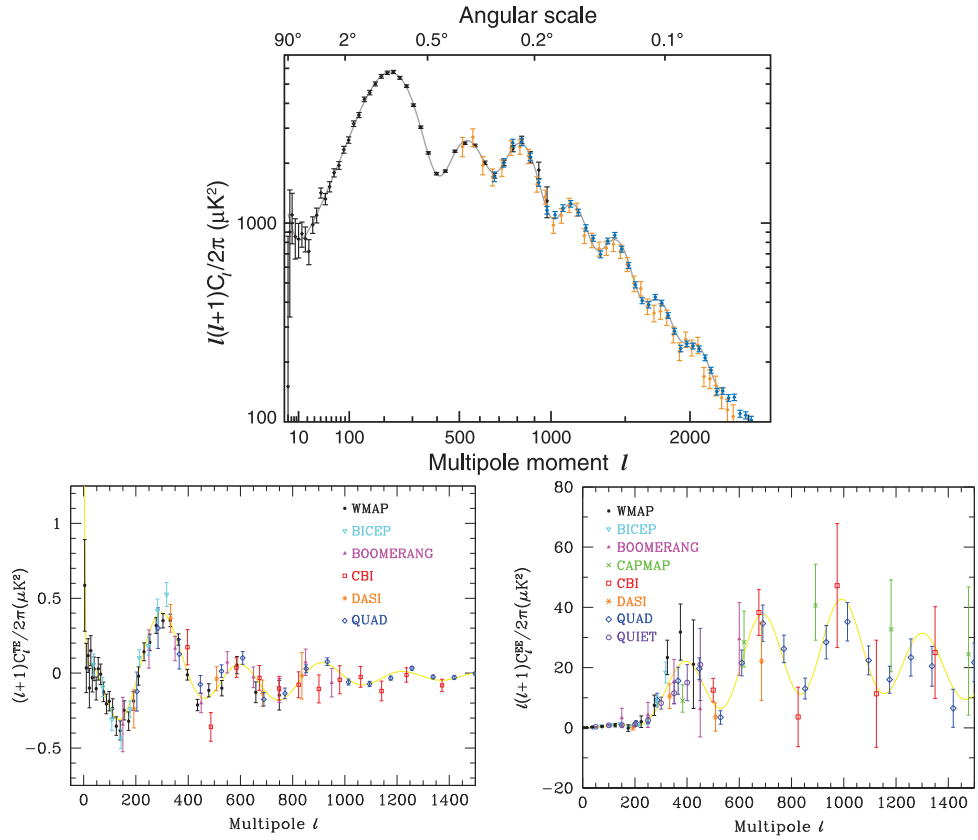

Figure 2.10: *Top: TT* power spectrum estimates from the WMAP (in black), SPT (blue) and ACT (orange) experiments. ΛCDM model fitted to the WMAP data is shown in grey. Image: NASA/WMAP Science Team. *Bottom: TE* and *EE* power spectra estimates from WMAP (black), BICEP (cyan), BOOMERANG (magenta), CBI (red), DASI (orange), QUaD (blue), CAPMAP (green), and QUIET (purple). The best-fit model curve (light yellow) is based on Planck's temperature observations, but as the intention is to show the pre-Planck status of polarisation data, the image serves its purpose well. Figures are reproduced from [19].

Table 2.2: Cosmological parameters estimated for the ΛCDM model from the WMAP 9-year data in combination with external datasets [52]: the ACT and SPT CMB data, baryon acoustic oscillation data and H_0 measurements [71].

	Label	Value
Independent	A_s	$(2.464 \pm 0.072) \times 10^{-9}$
	n_s	0.9608 ± 0.0080
	ω_b	0.02223 ± 0.00033
	ω_m	0.1376 ± 0.0020
	Ω_Λ	$0.7135^{+0.0095}_{-0.0096}$
	τ	0.081 ± 0.012
Derived	H_0	69.32 ± 0.80 (km/s)/Mpc
	t_0	13.772 ± 0.059 Gyr
Extended	$r_{0.002}$	< 0.13

Chapter 3

The Planck mission

The cosmic microwave background is accessible both from ground and space, but observations with ground-based or balloon-borne experiments are limited by the atmosphere and the available field of view. Although being more complex, space-borne mission are desired to overcome these limitations.

The European Space Agency's Planck satellite [13] is the successor of the NASA Cosmic Background Explorer (COBE) [62] and Wilkinson Microwave Anisotropy Probe (WMAP) [66]. The unprecedented combination of sensitivity, angular resolution and frequency coverage with full sky measurements make Planck the most powerful CMB experiment realised so far. The major milestones of the Planck mission are summarised in Table 3.1. The long development process culminated in launch on 14 May 2009, and the Planck collaboration has prepared three major data releases since. The Planck satellite was deactivated on 23 October 2013, and it was placed into a heliocentric orbit to prevent the endangering of future missions. The final results are expected in 2016.

In this Chapter we outline the main objectives of the Planck mission and briefly describe the satellite itself. We continue by summarising the data analysis pipeline, and conclude by reviewing scientific highlights from the mission.

3.1 Objectives

The cosmic microwave background radiation is the single most important source of cosmological information. Planck was designed to study the early Universe and its subsequent evolution. Planck provides answers to the key questions in modern science: how did the Universe begin, how did it evolve in the past, and how will it continue to evolve in the future? The ultimate goal of the Planck collaboration is to determine the geometry and contents of the Universe, and radically limit the space of viable theories describing the earliest stages and subsequent evolution of the Universe [13]. Additionally, Planck provides a wealth of data for a broad range of astrophysics [13].

During its lifetime, Planck

- measured the CMB temperature fluctuations with an accuracy set by fundamental astrophysical limits,
- measured the CMB polarisation, and

Table 3.1: The Planck mission timeline.

Planck mission conceived	1992
Initial COBRAS[a] and SAMBA[b] proposals presented to ESA	1993
ESA accepts the joint COBRAS/SAMBA[c]	1996
Launch	May 2009
Observations commence	Aug 2009
End of nominal mission	Nov 2010
First data release (ERCSC)	Jan 2011
End of HFI operations	Jan 2012
Second data release	Mar 2013
Spacecraft deactivated	Oct 2013
Third data release	Feb – Jul 2015
Final results expected	2016

[a] COsmic Background Radiation Anisotropy Satellite
[b] SAtellite for Measurement of Background Anisotropies
[c] Later the mission was renamed in honour of the German scientist and Nobel prize winner Max Planck (1858-1947).

- extracted valuable information on the properties of extragalactic sources as well as about the dust and gas in the Milky Way.

These measurements allow cosmologists, for example, to determine the values of the fundamental parameters describing our Universe, to test the different inflationary models, and to measure the Sunyaev-Zel'dovich effect in thousands of galaxy clusters.

3.2 Spacecraft

Figure 3.1 illustrates the key components of the Planck satellite, and Table 3.2 summarises the main characteristics of the spacecraft. Planck was built around two modules: one was devoted for the payload and the other for service electronics [84]. The payload module consisted of

- a telescope with a projected diameter of 1.5 m,
- two instruments, the Low Frequency Instrument (LFI) operating at 20 K and the High Frequency Instrument (HFI) operating at 0.1 K, for scientific measurements located on the focal plane,
- a telescope baffle providing both straylight shielding and radiative cooling, and
- three conical "V-groove" shields providing thermal isolation.

The service module, on the other hand, contained warm electronics, a solar panel, cryocoolers, an on-board computer, telecommand receivers, telemetry transmitters and an attitude control system. During scientific operations the solar panel faced the Sun placing everything else into a shadow.

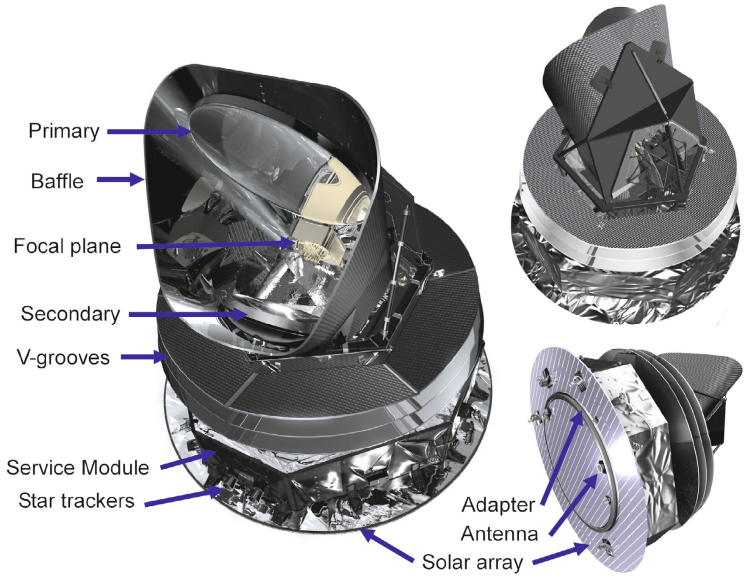

Figure 3.1: The main parts of the Planck satellite. The focal plane contains the instruments for scientific measurements. Figure is reproduced from [84].

Table 3.2: The Planck satellite characteristics.

Diameter	4.2 m
Height	4.2 m
Total mass at launch	1912 kg
Payload mass	205 kg
Electrical power demand	1300 W
Operational lifetime	53 months
On-board data storage capacity	32 Gbit
Data transmission rate to ground (max)	1.5 Mbps
Daily contact period	3 h
Overall cost[a]	700 M€

[a] Overall cost includes the spacecraft, launch, mission expenses, and science operations.

3.2.1 Instruments

Planck observed the microwave sky at nine frequency bands divided between two scientific instruments. The Low Frequency Instrument made measurements at frequency bands nominally centred around 30, 44, and 70 GHz, while the High Frequency Instrument covered regions around 100, 143, 217, 353, 545, and 857 GHz. The frequency coverage was designed to enclose both the peak of the CMB spectrum and the spectra of the Galactic foregrounds sufficiently broadly to allow for an accurate component separation. Figure 3.2 sketches the footprint of the Planck focal plane on the sky, where black crosses mark the orientation of

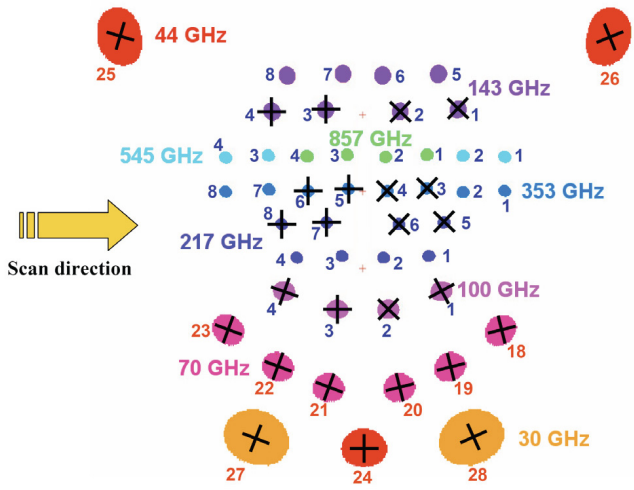

Figure 3.2: The footprint of the Planck focal plane on the sky. Each spot represents the beam shape at the full width at half maximum. The black crosses mark the orientation of linearly polarised detectors within each horn. The yellow arrow indicates the scan direction. Image: ESA and the Planck Collaboration.

the linearly polarised detectors within each horn. Table 3.3 summarises the main instrumental characteristics of both instruments.

The LFI included 22 pseudo-correlation radiometers connected to 11 corrugated feedhorns [84]. All LFI radiometers were sensitive to one linear polarisation direction. The two orthogonally-polarised radiometers in a horn are referred to as M and S radiometers. The feedhorns guided the collected radiation from the telescope to the radiometers, which amplified the signal using highly sensitive cryogenically cooled amplifiers. To suppress $1/f$-type noise behaviour[1] induced by the amplifiers, a pseudo-correlation method was adopted [85]: the amplifiers simultaneously processed the sky signal and a signal from the stable 4 K reference load. For each radiometer, both the sky and load time-ordered data were separately reconstructed and transmitted to the ground.

The HFI consisted of 52 bolometers fed by corrugated feedhorns [84]. In a bolometer radiation is absorbed on a spider web or grid like surface for total power and polarisation-sensitive measurements, respectively. The absorbed radiation heats the bolometer slightly and changes its electrical resistance, while readout electronics monitor the resistance to record a signal. The intensity of the incoming radiation dictates the amount of temperature change in the bolometer, which in turn forces the shift in resistance. The HFI bolometers required extremely low operating temperature of 0.1 K to minimise thermal noise in them. Only the four lowest frequency channels were capable of measuring the polarisation of incoming radiation, while the two higher bands were only sensitive to the total power [13].

Even though the LFI and HFI were build from the state of the art components to do outstanding observations on their own, it is the combination of the two instruments that give the Planck satellite its extraordinary powers, the redundancy along with the control over system-

[1] Chapter 3.5.2 discusses the LFI noise properties.

Table 3.3: The Planck instrument characteristics.

Instrument	Channel [GHz]	Detectors[a]	Detectors in the analysis	Sampling rate [Hz]	Resolution[b] [arcmin]	Ellipticity[c]
LFI	30	4	4	32.5	32.29	1.32
	44	6	6	45	27.00	1.04
	70	12	12	76.8	13.21	1.22
HFI	100	8 / 8	8	200	9.68	1.186
	143	12 / 8	11	200	7.30	1.040
	217	12 / 8	12	200	5.02	1.169
	353	12 / 8	12	200	4.94	1.166
	545	4	3	200	4.83	1.137
	857	4	4	200	4.64	1.336

[a] For the polarised HFI channels numbers are: the total number of bolometers / the number of polarised bolometers.
[b] Effective angular resolutions from [36].
[c] Effective beam ellipticity from [36].

atics and foregrounds alike, required to achieve the scientific objectives of the mission.

3.2.2 Cooling system

To achieve the planned science goals, the instruments on board Planck satellite needed extremely low operating temperatures. The LFI radiometers operated at 20 K, while the HFI bolometers required as low temperature as 0.1 K. These conditions were achieved as a series of temperature steps using a combination of passive and active cooling systems [13, 84]. Passive cooling system consisted of the V-groove shields and the telescope baffle shown in Figure 3.1. The active cooling system relied on the vital pre-cooling provided by the passive cooling system. The active stage comprised of three different coolers that ultimately reached the final operating temperature of the HFI [13, 84].

3.3 Operations

The Planck satellite made its observations from the second Lagrangian, L2[2], point of the Sun-Earth system. The location at the L2 minimised the amount of contamination from the solar, terrestrial and lunar emissions to maintain the thermal stability of the systems. But Planck did not sit still at L2, rather it orbited the Lagrangian point on a Lissajous trajectory, a quasi-periodic orbital trajectory around a Lagrangian point, with an average amplitude of about 400 000 km and a 6 month period. Had it stayed exactly at L2, Planck would have been almost

[2]L2 is a meta-stable point in the Sun-Earth system. It is located 1.5 million kilometres away from the Earth, and orbits the Sun at the same rate as the Earth.

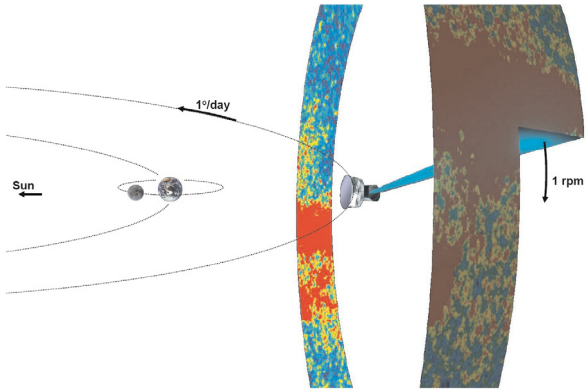

Figure 3.3: Illustration of Planck scanning the sky. The Planck satellite is placed on orbit around L2, and its field-of-view rotates at 1 rpm about the spin axis. The spin axis is turned daily 1° to maintain the anti-sun direction of the scientific instruments. Figure is reproduced from [84].

completely in the Earth's shadow, and as a consequence its solar panels would have been left unfunctional.

Planck accumulated data continuously during the mission. The collected data, roughly 13 Gbit per day, was downlinked daily to the ground over a three-hour contact period. The on-board memory had capacity to store at least two days of data in case of a missed contact period to secure continuity in the data at our disposal.

3.4 Scanning strategy, sampling and hits

Scanning strategy denotes the pattern how Planck's focal plane scanned the sky. Planck was continuously spinning around its principal axis at a rate of 1 rpm, the rate set immediately after the launch. As the focal plane traced the sky at an angle of about 85° from the spin axis, the field-of-view of the satellite followed nearly great circles on the sky. Additionally, the spin axis was shifted 1° per day in 2′ steps to maintain the anti-Sun direction of the satellite [84]. Figure 3.3 illustrates how the field-of-view rotates around the spin axis gradually scanning the whole cosmic sky. Such a scanning strategy does not, however, ensure full sky observations. The Planck scanning strategy adopted a further cycloidal precession (7.5° amplitude, a 6-month period) of the spin axis [86], which allowed Planck to cover the full sky in roughly six to eight months, and twice in a year. In the data analysis we divide the entire duration of the mission into six-month periods, called surveys, covering nearly the full sky. For the Planck LFI we have eight surveys to analyse in total.

Planck's spin axis was repointed on average every 45 minutes. The time between two consecutive repointings is called a pointing period. One detector covers the same circle repeatedly on the sky during one pointing period to high accuracy. Some pointing periods have been either temporarily lengthened or shortened, for example, to observe more closely Jupiter and the Crab nebula. A repointing manoeuvre took typically around 5 minutes. The satellite pointing during the manoeuvres is not considered known accurately enough for scientific work, and

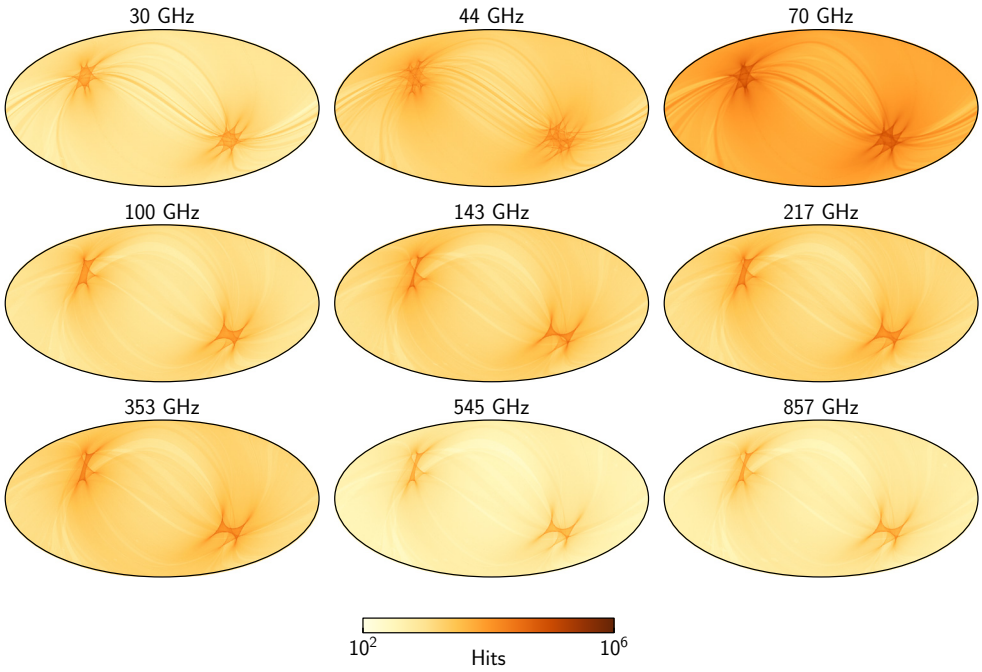

Figure 3.4: Number of observations per pixel, *hitmaps*, for Planck full mission data. Resolution in the LFI maps is $N_{\mathrm{side}} = 1024$, while for the HFI maps it is $N_{\mathrm{side}} = 2048$. Maps are shown in Galactic coordinates and in logarithmic colour scale.

these data are omitted in the data analysis. Planck's scanning strategy enables also observations from the same regions of the sky over various time scales and with sufficiently different scanning directions to allow e.g. for a stable map solution for all three Stokes components.

A detector integrates signal for a time interval, whose inverse is the sampling rate of the detector. Consecutive samples are collected with frequency f_{sample} (see Table 3.3). We further divide the sky into pixels using the Hierarchial Equal Area isoLatitude Pixelization (`HEALPix`) scheme [87]. The `HEALPix` map resolution is defined by an N_{side} parameter. The total number of pixels in a `HEALPix` map is $N_{\mathrm{pix}} = 12N_{\mathrm{side}}^2$. One sample assigned entirely to a single pixel on the `HEALPix` grid is called a hit. Figure 3.4 shows the full mission hitmaps, the number of observations per pixel, at all Planck frequency channels. The chosen scanning strategy resulted in a significantly inhomogenous distribution of hits across the sky: the areas near the ecliptic poles were observed more thoroughly than the others. Observations falling on the same map pixels at different times are called crossing points.

3.5 Systematics

The understanding of instrumental noise properties along with insight into other sources of systematics is essential for the success of any scientific measurement. Systematics hinder our ability to study the cosmological and astrophysical signals. They include effects such

as uncertainty in the pointing reconstruction, thermal fluctuations in the satellite's cooling systems and glitches in the data caused by cosmic ray particles hitting the detectors. For a thorough discussion of systematics affecting Planck see [88] and [89], and references therein. Next we consider two systematic effects that are especially relevant for the remainder of the thesis: the instrumental noise properties of the LFI and bandpass mismatch.

3.5.1 Bandpass mismatch

Polarisation is measured from the difference of two orthogonally-polarised radiometers within a horn. The two radiometers have nearly identical frequency responses, bandpasses, to the incoming radiation. A slight mismatch in the radiometer bandpasses would cause leakage of foreground total intensity into a spurious polarisation signal. Whereas the CMB, whose temperature is not frequency dependent, produces no spurious polarisation. For an in-depth discussion see [90].

3.5.2 Noise

A detailed knowledge of the noise properties is not only used as a key ingredient in several stages of the Planck data analysis, but also to monitor the system health. Any degradation or damage would show as an evolution of the noise properties in time.

For a radiometer the noise in the detected signal consists of two independent components: white (uncorrelated) and $1/f$ (correlated) noise [91]. The noise is assumed to have Gaussian distribution and zero mean. A non-zero mean would manifest itself just in the Stokes I monopole component, which does not have significance in the CMB anisotropy analysis.

The power spectral density (PSD) of the noise is approximately [91, **II**]

$$P(f) = \begin{cases} \frac{\sigma^2}{f_{\rm sample}} \left[1 + \left(\frac{f_{\rm knee}}{f}\right)^{\alpha}\right] & (f \geq f_{\rm min}), \\ \frac{\sigma^2}{f_{\rm sample}} \left[1 + \left(\frac{f_{\rm knee}}{f_{\rm min}}\right)^{\alpha}\right] & (f \leq f_{\rm min}), \end{cases} \tag{3.1}$$

where the flat part represents the white noise and the power-law term, $P(f) \propto f^{-\alpha}$, the correlated noise. In the above equation σ^2 is the white noise sample variance and $f_{\rm sample}$ is the sampling frequency. The correlated noise is modelled with three parameters $f_{\rm knee}$, α, and $f_{\rm min}$, which are knee frequency, slope, and minimum frequency, respectively. At the knee frequency the two noise components contribute equally to the total power of noise. The minimum frequency $1/f_{\rm min}$ sets the time scale over which the noise is correlated, and below $f_{\rm min}$ the spectrum becomes flat. As the noise estimation is performed by pointing periods, the longer correlations are absent, and we have three free parameters to characterise the noise properties: σ, α and $f_{\rm knee}$. The analytical noise model is illustrated in Figure 3.5 for the LFI 28M radiometer with Planck 2015 noise parameters.

The understanding of LFI's noise properties have been refined throughout the entire mission [**III**,**IV**,**V**, 92]. For the 2015 Planck analysis two different sets of noise estimates were derived from the flight data: the DPC ones [**V**] and estimates especially intended for full focal plane 8 (FFP8) simulations [92], hereafter called the FFP8 estimates. These both use the analytic 3-parameter model as a baseline, but one describes the entire mission with a single set of noise parameters while the other lets them evolve in time. Table 3.4 lists the LFI DPC noise estimates for each radiometer extending over the full duration of observations, and the estimation procedure is described in [**IV**, **V**]. This simple model is adequate in many applications, but for instance noise simulations require more refined noise description. The most

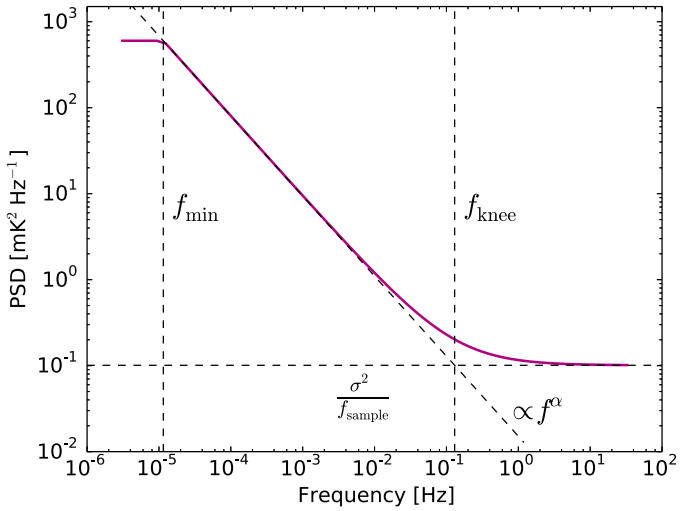

Figure 3.5: Analytic noise model for LFI 28M radiometer. Shape of the curve is defined by three parameters: the white noise level, $\sigma = 1.812$ mK; the slope, $\alpha = -0.931$; and the knee frequency, $f_{\rm knee} = 130.08$ mHz.

representative characterisation is provided by the FFP8 estimates comprising of daily fits, described in [92], to the analytic model. Figure 3.6 illustrates the two white noise σ estimates for the LFI 18M radiometer.

3.6 Planck analysis pipeline

The downlinked data was transferred via the mission operations centre (MOC) in Germany to the two Data Processing Centres (DPC) in Italy and France. The raw data flows through a long data analysis chain, illustrated schematically in Figure 3.7, reaching ultimately the long-awaited cosmological parameters. The data analysis pipeline is characterised by a tremendous compression in the data volume, while preserving as much cosmological information as possible. The intermediate data products, maps and power spectra, are necessary to maintain the computations feasible.

- **Pre-processing.** The pre-processing step converts the raw data into timelines usable in the subsequent analysis steps. The raw data is cleaned of all major systematic effects, and calibrated to astrophysical units [42, 36]. The contribution from the solar and orbital dipoles are also removed, and samples unusable for science are flagged. The pre-processing also provides the noise estimates, as well as the pointing information.

- **Map-making.** The map-making step compresses the timelines into sky maps. After the pre-processing, the timelines contain still a contribution from low-frequency noise, which is removed by an appropriate map-making algorithm (see Chapter 4). The products are pixelised maps of the Stokes I, Q and U components, along with the description of residual noise in them (see Chapter 5).

Table 3.4: Planck 2015 noise parameters for LFI radiometers as estimated by the LFI DPC.

		Knee frequency f_{knee} [mHz]		Slope α		White noise[a] σ [mK]	
	Radiometer	M	S	M	S	M	S
70 GHz	LFI-18	14.82	17.78	1.060	1.180	4.553	4.146
	LFI-19	11.72	13.71	1.207	1.111	5.144	4.926
	LFI-20	7.96	5.67	1.198	1.298	5.212	5.507
	LFI-21	37.89	13.27	1.247	1.205	4.003	4.971
	LFI-22	9.68	14.80	1.424	1.237	4.356	4.715
	LFI-23	29.65	59.03	1.073	1.211	4.476	4.790
44 GHz	LFI-24	26.78	88.30	0.942	0.908	3.159	2.734
	LFI-25	20.07	46.37	0.845	0.904	2.834	2.698
	LFI-26	64.42	68.19	0.918	0.758	3.295	2.887
30 GHz	LFI-27	174.53	108.79	0.927	0.907	1.605	1.729
	LFI-28	130.08	43.08	0.931	0.900	1.812	1.633

[a] $\sigma = \sqrt{f_{sample}} \cdot \mathrm{NET}_{RJ}$, where NET_{RJ} is the white noise sensitivity.

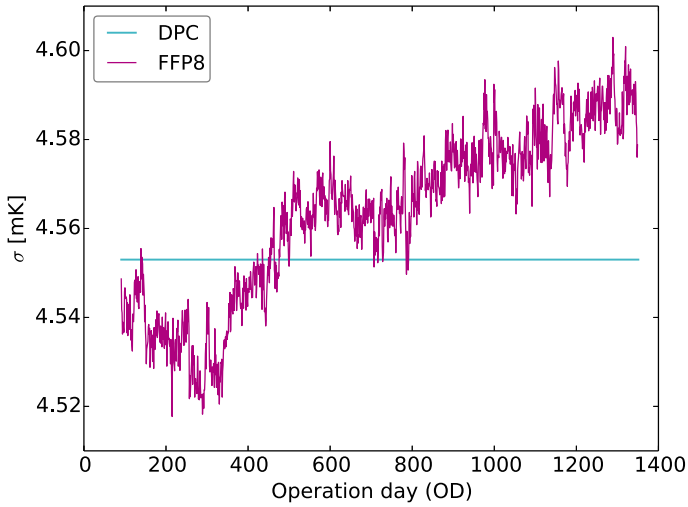

Figure 3.6: The Planck 2015 estimates of the white noise σ for the LFI 18M radiometer. The Planck LFI data processing centre (DPC) estimate is fit as a time-independent constant, while the full focal plane 8 simulation (FFP8) estimate evolves in time. The mean of the FFP8 σ is higher than the DPC value: 4.563 mK compared to 4.553 mK.

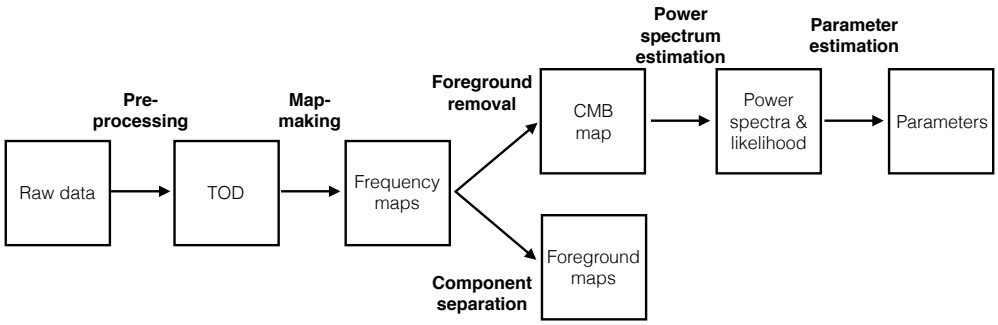

Figure 3.7: Schematic illustration of the data flow in the Planck analysis pipeline.

- **Component separation.** The Planck maps do not only contain signal from the CMB, but a number of other astrophysical sources of microwave emission. The component separation step aims to either remove or separate different foreground components from the CMB signal in order to provide clean maps for subsequent analysis steps. The separation is enabled by the multi-frequency observations, and therefore relies on different spatial and spectral characteristics of the emissions. Various methods, based on either physical models of components or statistical methods, have been developed to achieve the separation and to characterise remaining residuals [93, 94].
- **Power spectrum estimation.** Theoretical predictions of the CMB anisotropy are statistical in nature. In the linear regime, anisotropies predicted by most inflationary models generate Gaussian fluctuations. Thus, the complete cosmological information in a sky map is contained in its power spectra: all the information from Planck dataset can be compressed into just a few thousand numbers. To be able to exploit the achieved reduction in the data volume in the last analysis step, we construct additionally a likelihood function describing the probabilities of theoretical models in light of the observed data [95].
- **Parameter estimation.** Once the full likelihood function is available, it can be used to constrain the cosmological parameters. In the Markov Chain Monte Carlo (MCMC) approach a random walk through the parameter space converges iteratively to the most likely parameter values [96].

3.7 Scientific highlights from Planck

The Planck collaboration has made available three major data releases to the scientific community. The first released dataset consisted of the Early Release Compact Source Catalogue (ERCSC) — a list of unresolved and compact sources extracted from the first complete all sky survey [97]. The early release of the data facilitated follow ups using ground- or space-based observatories. The second data release was based on the first 15 months of temperature data, *nominal mission*, and included the first cosmology results from Planck [42]. The third data release was based on the entire Planck mission, *full mission*, on both temperature and polarisation data [36]. The final results from the Planck collaboration are expected in 2016, and

improvements are anticipated especially due to the revised treatment of low-ℓ systematics. The published data to date is available via the Planck Legacy Archive[3], and science products include:

- Cleaned and calibrated timelines for each detector,
- Frequency maps,
- CMB maps,
- Angular power spectra,
- Likelihood,
- Foreground maps[4],
- Lensing potential map,
- Compact source catalogues of both Galactic and extragalactic sources,
- Catalogue of Galactic cold clumps,
- SZ source catalogue,
- Cosmological parameters,
- Constraints on B-modes[5],
- Higher order statistics,
- Simulations[6], and
- Noise covariance matrices and corresponding low-resolution maps.

Figures 3.8–3.13 illustrate various science products from the 2015 data release: the intensity and polarisation maps for each frequency channel, the foregrounds maps, a CMB map, and the lensing potential map. All the depicted full sky maps highlight the unique combination of Planck's sensitivity, angular resolution and frequency coverage compared to the preceding missions. Both the temperature and polarisation maps in Figures 3.8 and 3.9 show significant foreground contamination, which is strongly frequency dependent. The recent Planck data combined with auxiliary datasets, the WMAP 9-year observations [52] and a 408 MHz survey map [99], revealed the most detailed description of the astrophysical sky at Planck frequencies, depicted in Figures 3.10 and 3.11 [94]. The present data allowed the reconstruction of six primary emission mechanisms in temperature: the CMB, the synchrotron, the free-free, the spinning dust, the thermal dust and CO line emissions [94]. Additionally, the thermal SZ emission around two pre-chosen regions, the Coma and Virgo clusters, and a molecular line emission between 90 and 100 GHz were identified from the temperature data [94]. The polarisation data is described by three primary emission mechanisms: the CMB, the synchrotron and the thermal dust [94]. Further, the Planck's view on polarised dust emission over the full-sky is the first of its kind [94]. The full-sky image of the CMB in Figure 3.12 emphasises especially the precision of Planck's instruments: the extracted temperature anisotropy map presents in practice every detail there is extractable within the astrophysical limits. The full-sky lensing potential map in Figure 3.13 is another pioneering data product from the Planck collaboration.

After the recent Planck data release, the astrophysical sky is now known down to one percent accuracy [94]. Figure 3.14 summarises our knowledge of microwave emissions from another perspective: it illustrates the spectra of main microwave emissions for temperature and polarisation alike. For the first time the polarisation spectra are are based on observations

[3] http://archives.esac.int/pla2

[4] Planck collaboration has released following component maps: thermal dust (both T and P), synchrotron (T and P), free-free emission, spinning dust and CO emission.

[5] In collaboration with BICEP2/Keck Array [98].

[6] The complete set of simulations can be accessed from `http:crd.lbl.gov/cmb-data`.

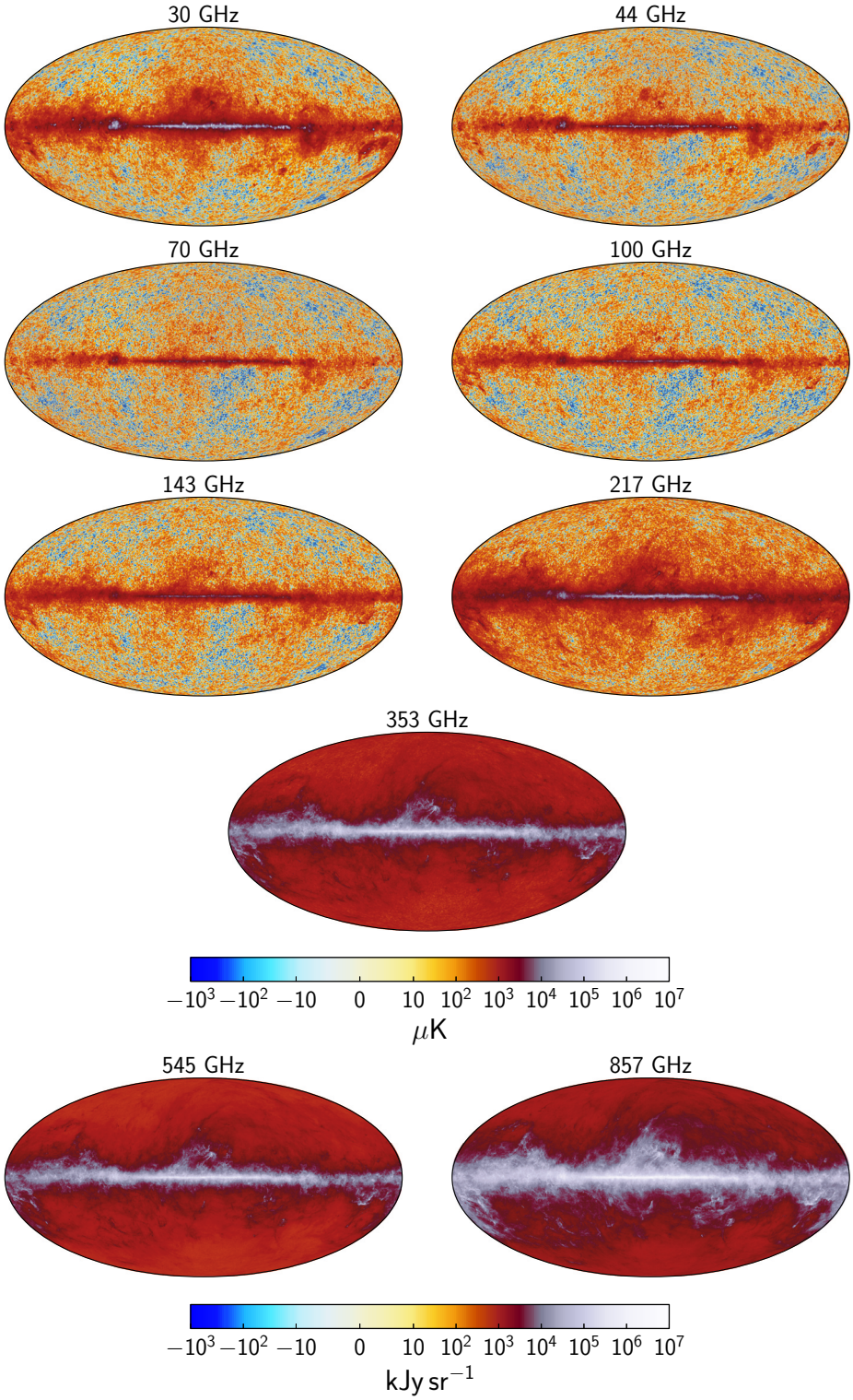

Figure 3.8: The Planck 2015 temperature maps in Galactic coordinates. The colour scale is designed to show the full dynamic range of the maps.

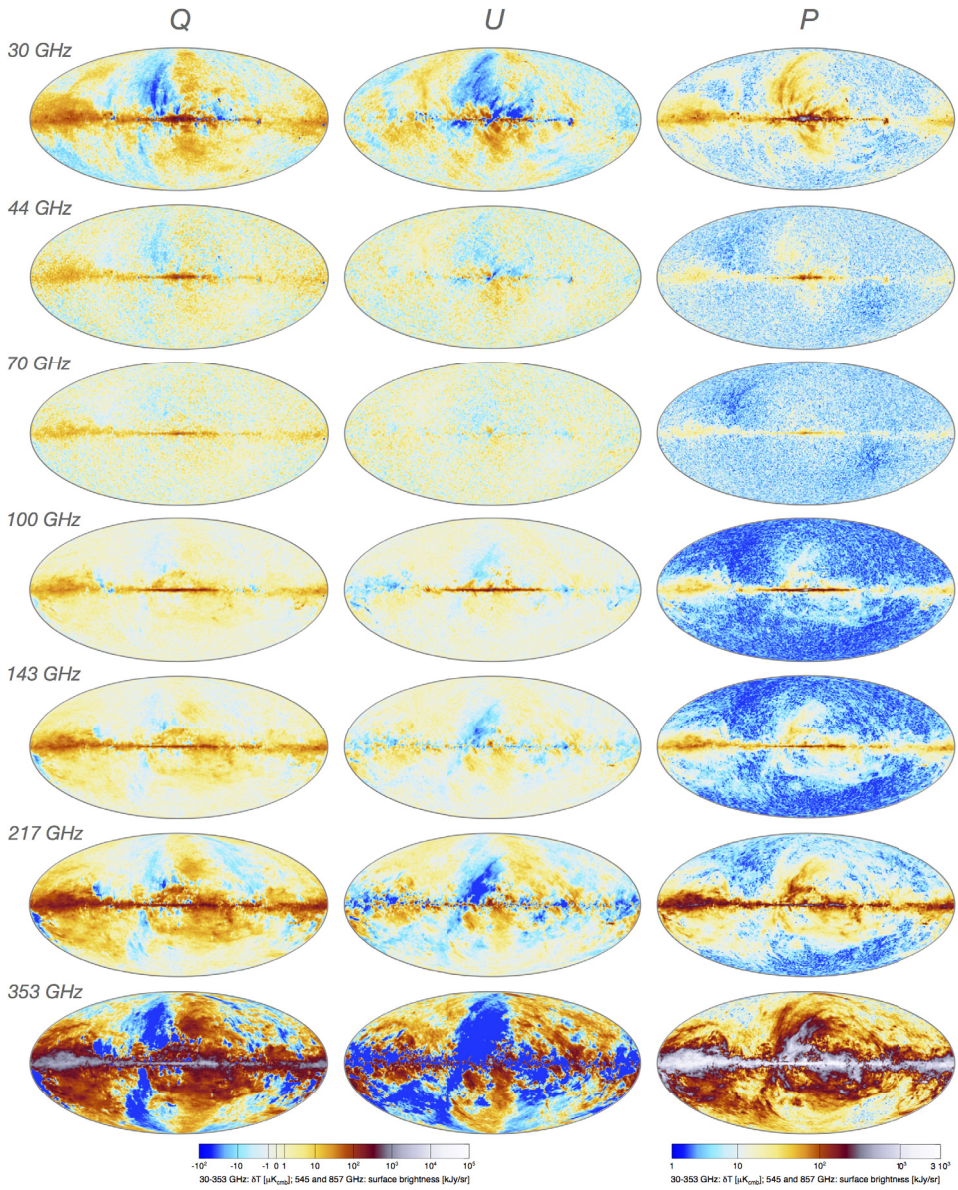

Figure 3.9: The Planck 2015 polarisation maps for all polarisation sensitive channels, 30 to 353 GHz, in Galactic coordinates. Columns from *l*eft to *r*ight are the Stokes Q and U components, and the total polarisation amplitude P. Bandpass correction has been applied to the HFI maps (100 to 353 GHz), while the LFI ones are not corrected. Image: ESA and the Planck Collaboration.

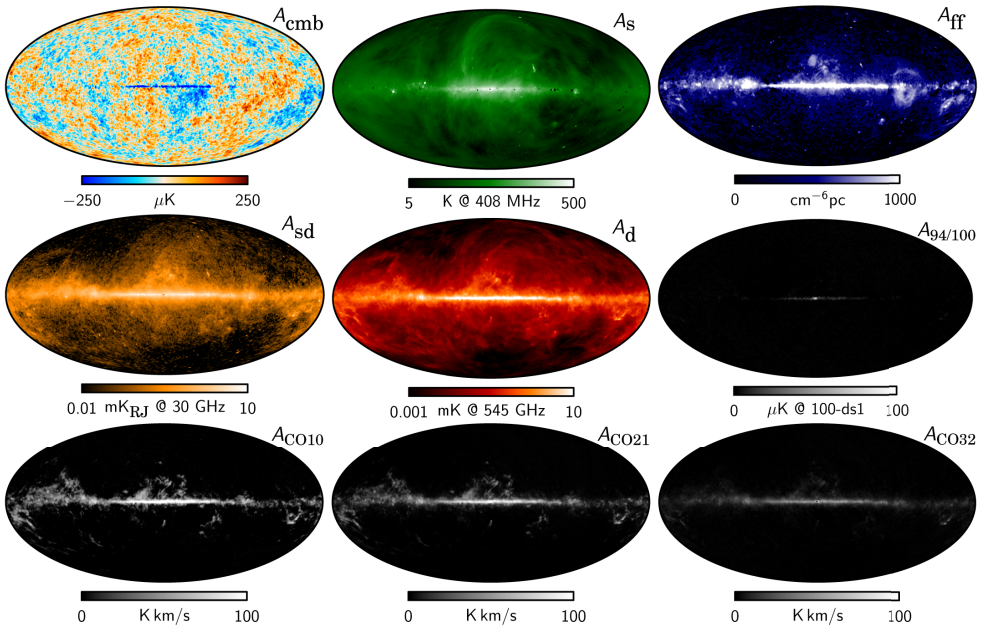

Figure 3.10: The Planck 2015 component maps for temperature observations in Galactic coordinates. From *left* to *right*, *top* to *bottom*: CMB, synchrotron, free-free, spinning dust, thermal dust, line emission around 90 GHz, and CO line emissions. Images: ESA and the Planck Collaboration.

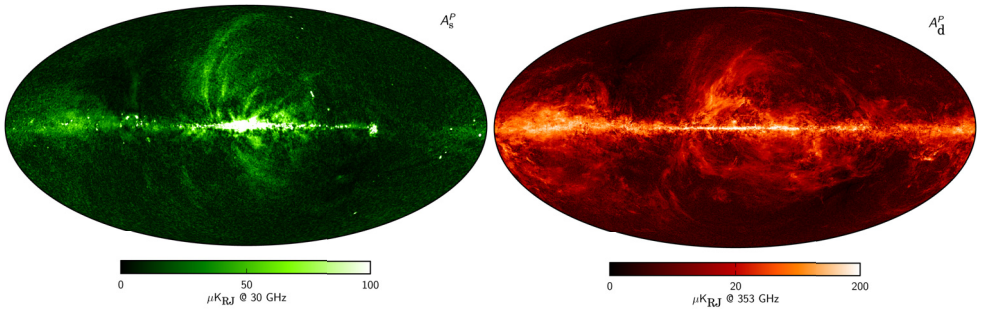

Figure 3.11: The Planck 2015 polarisation amplitude, $P = \sqrt{Q^2 + U^2}$, maps at 30 GHz for synchrotron radiation (*left*) and at 353 GHz for dust emission (*right*) in Galactic coordinates. Images: ESA and the Planck Collaboration.

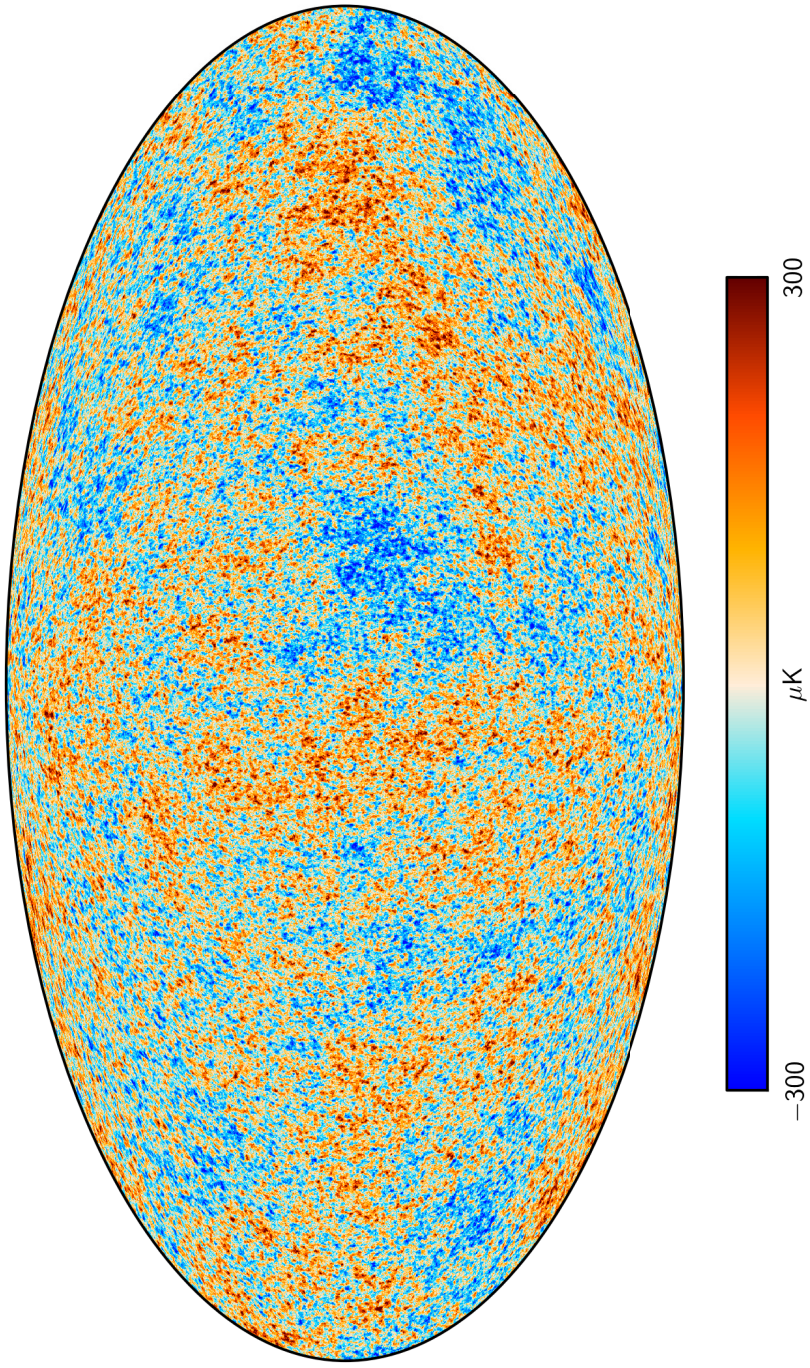

Figure 3.12: The Planck 2015 all sky temperature map in Galactic coordinates. On the Galactic plane 1.6% of the sky is artificially filled with a constrained realisation having the same statistical properties as the rest of the sky. Image: ESA and the Planck Collaboration.

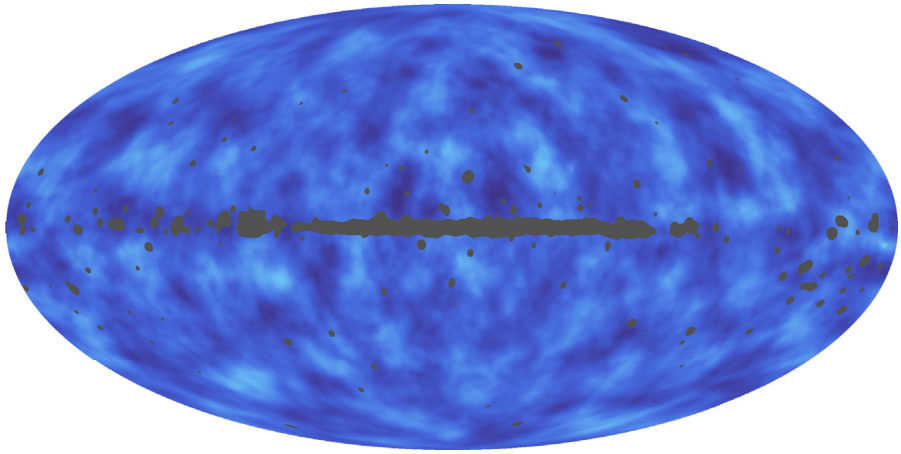

Figure 3.13: Lensing potential map in Galactic coordinates. Colour differences in the map highlight the distribution of matter in the Universe as seen projected on the sky. Grey areas are masked due to bright foregrounds. Image: ESA and the Planck Collaboration.

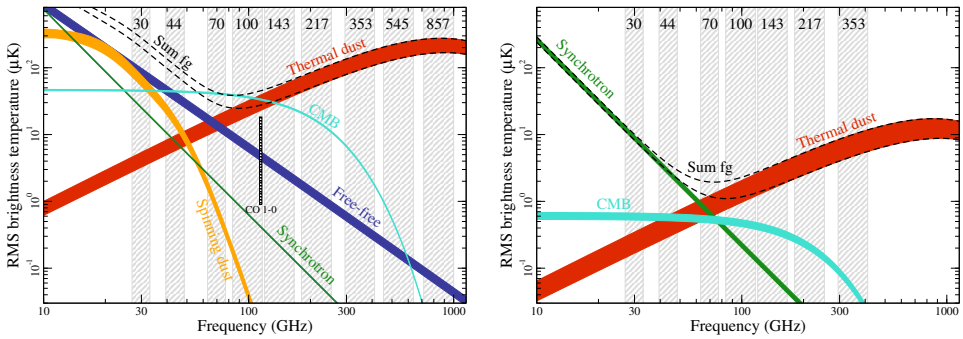

Figure 3.14: Planck 2015 microwave emission spectra for temperature (*left*) and polarisation (*right*). Images: ESA and the Planck Collaboration.

alone [94]. These agree broadly with the WMAP 9-year results presented in [52], but differ for example in the relative amplitudes of synchrotron and spinning dust components [94]. Moreover, Planck polarisation data indicates that for the primordial B-mode searches no region of the sky can be treated as dust-free [100]

The 2015 Planck data remains in excellent agreement with the ΛCDM model. The measured angular power spectra for TT, TE and EE are shown in Figure 3.15 along with the best-fit ΛCDM theoretical spectra — fitted only to the Planck temperature and low-ℓ polarisation data. The used low-ℓ polarisation data derives from the LFI 70 GHz observations cleaned with synchrotron and dust templates from 30 and 353 GHz channels, respectively. The Planck data has reduced clearly the scatter of data, and every power spectrum now features beautifully several peaks and troughs. The residuals are still larger than expected indicating the presence of some unaccounted systematics [36].

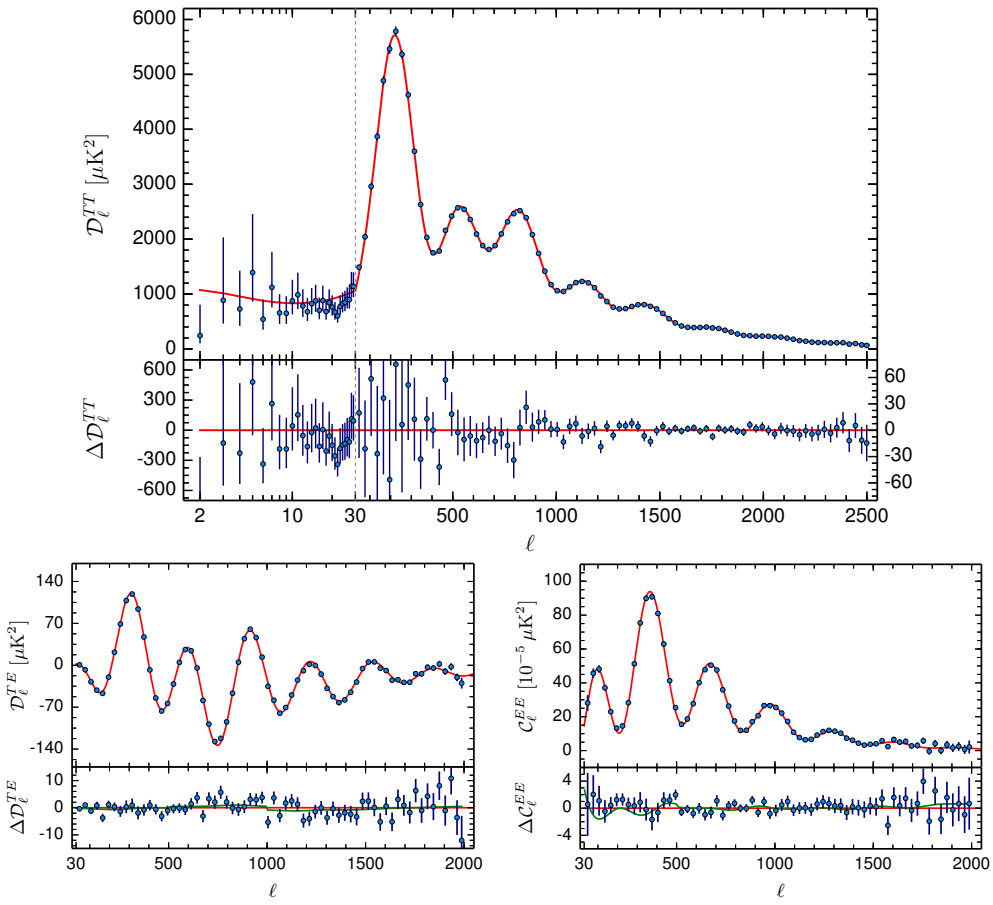

Figure 3.15: Planck 2015 CMB power spectra for TT (*top*), TE (*lower left*) and EE (*lower right*). The best-fit ΛCDM model is plotted in red in the upper panels, while residuals with respect to the model are shown in the lower panels. Images: ESA and the Planck Collaboration.

Table 3.5: Cosmological parameters estimated from the Planck 2015 data for the ΛCDM model [9]. The dataset consists of temperature, gravitational lensing and low-ℓ polarisation data.

	Label	Value
Independent	A_s	$(2.139 \pm 0.063) \times 10^{-9}$
	n_s	0.9677 ± 0.0060
	ω_b	0.02226 ± 0.00023
	ω_m	0.1415 ± 0.0019
	Ω_Λ	0.692 ± 0.012
	τ	0.066 ± 0.016
Derived	H_0	67.8 ± 0.9 (km/s)/Mpc
	t_0	13.799 ± 0.038 Gyr
Extended	$r_{0.002}$	< 0.11

Table 3.5 lists the Planck 2015 best-fit cosmological parameters for the combined temperature, gravitational lensing and low-ℓ polarisation data. Lensing is an essential ingredient in the soup — Planck has detected it with the highest significance so far [51]. The Planck observations confirm the basic ΛCDM model by reducing the uncertainties of the key cosmological parameters and constraining deviations even further [9]. The data does not indicate any need for new physics, nor extensions to the 6-parameter model. According to Planck, the Universe contains 4.9% of ordinary matter, 25.9% of dark matter and 69.2% of dark energy, and its age is 13.8 billion years old. The simplest model of inflation is still favoured: Planck data is consistent with an adiabatic, power-law spectrum of primordial density fluctuations, whose spectral index is significantly different from unity. The recent data also indicates a lower optical depth, than inferred earlier from the WMAP 9-year data, implying a lower reionisation redshift [9, 52]. Hence, the first stars have more than 100 million extra years to form. Although the high-ℓ polarisation data has been omitted in the formal parameter estimation, it does provide encouraging support for the official analysis [9].

The primordial gravitational waves have still remained elusive. A joint analysis of the Planck polarisation data and BICEP2/Keck Array observations revealed that significant part of the reported BICEP2 signal [83] is explained by polarised dust emission [98]. Combined data from the two experiments has pushed the upper limit on primordial gravitational waves down to $r_{0.002} < 0.09$ [9][7].

The final legacy of the Planck mission remains to be seen, but already Planck has achieved its scientific objectives. Planck's contribution to the understanding of the foregrounds has been substantial. The foreground legacy will remain as a baseline for future experiments in the long term. Planck has also taken the precision cosmology to the next level: main parameters are known to great accuracy, and availability of low-ℓ polarisation data begin to pin down the optical depth and the tensor-to-scalar ratio. Systematics, suspected anomalies, and tensions with some astrophysical data will keep the worldwide community engaged for years to come.

[7]The most recent results on combined BICEP2/Keck and Planck data place even tighter upper limit, namely $r_{0.005} < 0.07$ [101], where $r_{0.005} \approx 1.12 r_{0.002}$ for small r [9].

Chapter 4

Map-making

Maps are common objects. We see and use them on a daily basis. Hence, the most intuitive way of illustrating the collected CMB data visually is to project the data onto pixelised maps of the sky. But these maps serve an even greater purpose: they act as a orders-of-magnitude compression in the data volume to be analysed further.

Systematics and instrumental noise are present in every experiment, even if their minimisation has been the driving force in the instrumental design. The Planck Low Frequency Instrument data are contaminated by a slowly varying $1/f$ noise, which will alter the statistical properties of the maps — if left untreated. The correlated noise is most optimally handled during the map-making process. Thus, in addition to simply visualising and compressing the data, a proper map-making algorithm aims at removing the $1/f$ noise, while processing the CMB signal and white noise as little as possible.

In this Chapter we begin with an introduction to the map-making, and continue the discussion with more sophisticated map-making algorithms, namely with destriping and generalised destriping principles. Later we will consider low-resolution maps: why they are needed and how they are produced. We will conclude the Chapter by describing the map-making procedure for the Planck Low Frequency Instrument.

4.1 The map-making problem

The sky is scanned according to a chosen scanning strategy with a detector, and measured samples are returned with the sampling rate of f_{sample}. Each recorded measurement is a sum of signal s and noise n, where the signal observed by a detector sensitive to one linear polarisation direction is

$$s = I + Q\cos(2\psi) + U\sin(2\psi). \tag{4.1}$$

Above, ψ is the orientation of polarisation sensitivity, that depends both on the momentary orientation of the spacecraft, and on the detector's orientation on the focal plane. Further, the stream of data from the instrument is gathered in a time-ordered data (TOD) vector $\boldsymbol{d}$ of N_{TOD} elements,

$$\boldsymbol{d} = \boldsymbol{s} + \boldsymbol{n}. \tag{4.2}$$

We model the sky signal $\boldsymbol{s}$ as a pixelised map $\boldsymbol{m}$ of N_{pix} pixels, while for a polarisation sensitive experiment a given map contains one submap for each Stokes parameter: I, Q and

U. Hence, the total number of elements in a map is $3N_{\rm pix}$. A pointing matrix P of size ($N_{\rm TOD}$, $3N_{\rm pix}$) encodes a linear transformation between $\boldsymbol{s}$ and $\boldsymbol{m}$,

$$\boldsymbol{s} = \mathsf{P}\boldsymbol{m}, \tag{4.3}$$

by relating each sample to the corresponding pixel on the sky. P is a sparse matrix: it has only three non-vanishing elements (1, $\cos 2\psi$, $\sin 2\psi$) on each row, as each sample is sensitive to only one pixel, defined by the beam centre, of the sky. For observations with multiple detectors, the full TOD vector can be obtained by appending TODs from individual detectors end-to-end. The full data model becomes

$$\boldsymbol{d} = \mathsf{P}\boldsymbol{m} + \boldsymbol{n}. \tag{4.4}$$

Estimating the map $\boldsymbol{m}$ from the TOD vector $\boldsymbol{d}$ in equation (4.4) is the heart of the map-making problem.

In reality the sky is observed through an instrumental beam. In this context we assign each sample entirely to a pixel hit by the beam centre, but the true underlying sky signal is convolved with the instrumental beam. Observing with a symmetric beam will smooth all pixels equally, but a non-symmetric beam will introduce unique smoothing pattern to each pixel, that depends on the beam and the scanning strategy. We do not attempt to deconvolve the instrumental beam during the map-making process, but such approaches have been discussed in the literature [102, 103, 104, 105].

We also implicitly assume that the signal has a constant value across each pixel. This is a good approximation when the pixel size is smaller than the beam. For the Planck LFI the chosen map resolution corresponds to the average pixel size of 10–25% of the beam full width at half maximum (FWHM) [**VI**]. By replacing $\boldsymbol{s}$ with $\mathsf{P}\boldsymbol{m}$, we will lose information on scales smaller than the pixel size. All angular scales will affect the signal, but only the scales larger than the pixel size are supported by the map. This loss of sub-pixel structure is called pixelisation noise.

In addition to pixelisation noise, real data contain also other sources of signal variations that are not captured by the signal model in equation (4.3). These include the bandpass mismatch, beam shape mismatch, and in-pixel differences in the detector pointing, to name a few. Therefore, when a given pixel is observed with a different radiometer, with a different orientation of the beam, or the beam centre pointing in a slightly different position within the pixel, our measurement will yield a slightly different signal. We refer to these signal variations as signal error.

Once we have the observed data $\boldsymbol{d}$, a map is most intuitively constructed by averaging all the data falling into each pixel. In matrix notation, we can write the operation as

$$\tilde{\boldsymbol{m}} = \left(\mathsf{P}^{\mathsf{T}}\mathsf{P}\right)^{-1}\mathsf{P}^{\mathsf{T}}\boldsymbol{d}, \tag{4.5}$$

where P^{T} projects the data into the right pixel, and a diagonal matrix $\mathsf{P}^{\mathsf{T}}\mathsf{P}$ counts how many times each pixel is observed. As the real experiments contain noise, we are more interested of the weighted average,

$$\tilde{\boldsymbol{m}} = \left(\mathsf{P}^{\mathsf{T}}\mathsf{W}^{-1}\mathsf{P}\right)^{-1}\mathsf{P}^{\mathsf{T}}\mathsf{W}^{-1}\boldsymbol{d}, \tag{4.6}$$

where the weights are expressed as a diagonal weight matrix W. This is what we call binning. In the absence of correlated noise, it is the most accurate map available. However, as the noise is correlated in reality, it is necessary to develop more versatile map-making algorithms.

4.2 Maximum likelihood map-making

Statistical properties of the noise $\boldsymbol{n}$ may or may not be known prior to the map-making. Without loss of generality, we can assume that the noise vector has a zero mean, $\langle \boldsymbol{n} \rangle = 0$, with the noise covariance matrix C_n,

$$\mathsf{C}_n = \langle \boldsymbol{n}\boldsymbol{n}^\mathsf{T} \rangle. \tag{4.7}$$

In addition, we assume that the noise has a Gaussian distribution with a probability density function $P(\boldsymbol{n})$,

$$P(\boldsymbol{n}) = (2\pi \det \mathsf{C}_n)^{-\frac{1}{2}} \exp\left(-\frac{1}{2}\boldsymbol{n}^\mathsf{T}\mathsf{C}_n^{-1}\boldsymbol{n}\right). \tag{4.8}$$

Assuming no prior knowledge of the sky signal or the input map, and inserting $\boldsymbol{n} = \boldsymbol{d} - \mathsf{P}\boldsymbol{m}$ from equation (4.4) into equation (4.8), the likelihood of getting the input map given the data is

$$\mathcal{L}(\boldsymbol{m}|\boldsymbol{d}) = P(\boldsymbol{d}|\boldsymbol{m}) = (2\pi \det \mathsf{C}_n)^{-\frac{1}{2}} \exp\left(-\frac{1}{2}\left(\boldsymbol{d} - \mathsf{P}\boldsymbol{m}\right)^\mathsf{T} \mathsf{C}_n^{-1} \left(\boldsymbol{d} - \mathsf{P}\boldsymbol{m}\right)\right). \tag{4.9}$$

Maximising the likelihood in equation (4.9) with respect to $\boldsymbol{m}$ is equivalent to minimising the log-likelihood function,

$$\chi^2 = -2 \ln \mathcal{L}(\boldsymbol{m}|\boldsymbol{d}) = \left(\boldsymbol{d} - \mathsf{P}\boldsymbol{m}\right)^\mathsf{T} \mathsf{C}_n^{-1} \left(\boldsymbol{d} - \mathsf{P}\boldsymbol{m}\right), \tag{4.10}$$

which yields the maximum-likelihood map (e.g. [53, 106])

$$\tilde{\boldsymbol{m}} = \left(\mathsf{P}^\mathsf{T}\mathsf{C}_n\mathsf{P}\right)^{-1} \mathsf{P}^\mathsf{T}\mathsf{C}_n^{-1}\boldsymbol{d}. \tag{4.11}$$

The maximum-likelihood estimate $\tilde{\boldsymbol{m}}$ leads to the minimum variance of the residual map, $\Delta\boldsymbol{m} = \tilde{\boldsymbol{m}} - \boldsymbol{m}$, and is lossless in the sense that it contains ideally all the cosmological information from the original TOD [107]. Such a map-making algorithm has been applied in the COBE [108] and the ACT [109] experiments. For the modern-sized datasets, such as Planck data, the maximum likelihood map-making is a computationally demanding task. We need less resource intensive algorithms for faster turnround.

4.3 Destriping

The destriping method [110, 91, 111, 112, 113, **I**] is motivated by the presence of correlated low-frequency noise in the data. The noise vector $\boldsymbol{n}$ is further divided into two components: correlated noise and white noise. In the destriping approach we model the correlated noise component by a sequence of constant offsets, called baselines. The same offset applies for N_base adjacent samples, as illustrated in Figure 4.1. Thus, we write our noise model as

$$\boldsymbol{n} = \mathsf{F}\boldsymbol{a} + \boldsymbol{w}, \tag{4.12}$$

where the vector $\boldsymbol{w}$ represents white noise, the vector $\boldsymbol{a}$ contains unknown baseline amplitudes, and the matrix F of size $(N_\mathrm{TOD}, N_\mathrm{base})$ projects them into the TOD. We can write the matrix F explicitly as

$$\mathsf{F} = \begin{pmatrix} \mathbb{1}_{N_\mathrm{base}\times 1} & 0 & 0 & \dots \\ 0 & \mathbb{1}_{N_\mathrm{base}\times 1} & 0 & \dots \\ 0 & 0 & \mathbb{1}_{N_\mathrm{base}\times 1} & \dots \\ \vdots & \vdots & \vdots & \ddots \end{pmatrix}. \tag{4.13}$$

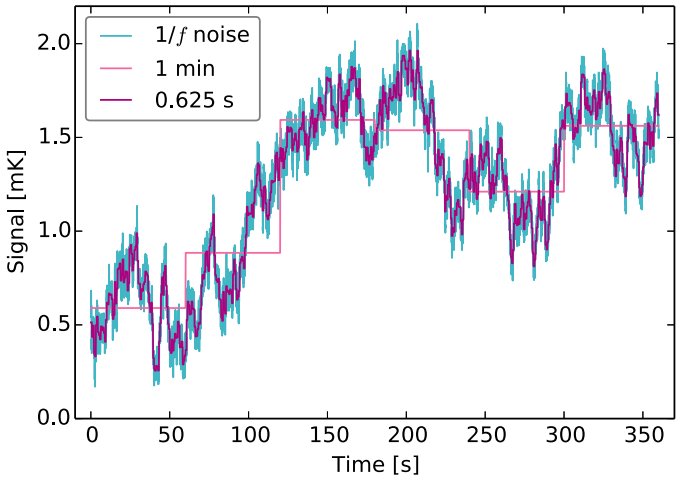

Figure 4.1: A six-minute slice of simulated $1/f$ noise from papers [**I**,**II**] along with 1 min and 0.625 s baselines. The baseline length, N_{base}, equals 4608 and 48 samples, respectively. The shorter baselines mimic the $1/f$ noise pattern more closely.

No prior knowledge of the baseline amplitudes is required in the destriping approach.

We can express the destriping method in the maximum likelihood form as well [113]. The white noise is assumed to be the result of a Gaussian random process and uncorrelated,

$$\langle w_t w_{t'} \rangle = \sigma_t^2 \delta_{tt'}, \tag{4.14}$$

with diagonal white noise covariance matrix,

$$\mathsf{C}_w = \langle \boldsymbol{w}\boldsymbol{w}^{\mathsf{T}} \rangle = \mathrm{diag}\left(\sigma_1^2, \sigma_2^2, \dots\right). \tag{4.15}$$

Therefore, the probability of the TOD vector $\boldsymbol{d}$ given the input map $\boldsymbol{m}$ and the baseline amplitudes $\boldsymbol{a}$ is

$$P(\boldsymbol{d}|\boldsymbol{m},\boldsymbol{a}) = (2\pi \det \mathsf{C}_w)^{-\frac{1}{2}} \exp\left(-\frac{1}{2}\boldsymbol{w}^{\mathsf{T}}\mathsf{C}_w^{-1}\boldsymbol{w}\right), \tag{4.16}$$

where $\boldsymbol{w} = \boldsymbol{d} - \mathsf{P}\boldsymbol{m} - \mathsf{F}\boldsymbol{a}$. We can once again write the function to be minimised as

$$\chi^2 = (\boldsymbol{d} - \mathsf{P}\boldsymbol{m} - \mathsf{F}\boldsymbol{a})^{\mathsf{T}}\, \mathsf{C}_w^{-1}\, (\boldsymbol{d} - \mathsf{P}\boldsymbol{m} - \mathsf{F}\boldsymbol{a}). \tag{4.17}$$

We want to minimise equation (4.17) with respect to both $\boldsymbol{m}$ and $\boldsymbol{a}$.

Minimising equation (4.17) with respect to $\boldsymbol{a}$ yields an equation for baseline amplitudes

$$\mathsf{F}^{\mathsf{T}}\mathsf{C}_w^{-1}\mathsf{Z}\mathsf{F}\tilde{\boldsymbol{a}} = \mathsf{F}^{\mathsf{T}}\mathsf{C}_w^{-1}\mathsf{Z}\boldsymbol{d}, \tag{4.18}$$

where

$$\mathsf{Z} = \mathbb{1} - \mathsf{P}\left(\mathsf{P}^{\mathsf{T}}\mathsf{C}_w^{-1}\mathsf{P}\right)^{-1}\mathsf{P}^{\mathsf{T}}\mathsf{C}_w^{-1}. \tag{4.19}$$

Because the matrix $\mathsf{F}^{\mathsf{T}}\mathsf{C}_w^{-1}\mathsf{Z}\mathsf{F}$ is singular [113, **I**], we cannot solve the baseline amplitudes by directly inverting the equation (4.18). It is commonly solved through the iterative conjugate

gradient method [114, 113]. The matrix Z acts on a TOD by subtracting from each sample the weighted average of all the samples hitting the corresponding pixel. The operation $\mathsf{Z}\boldsymbol{d}$ on the right-hand side of equation (4.18) yields zero for a constant TOD vector, and hence results in a zero baseline solution. Therefore, the destriping cannot determine the absolute monopole of a map. The resulting arbitrary monopoles can be removed from the maps during a post-processing step.

The final destriped map is obtained by minimising equation (4.17) with respect to $\boldsymbol{m}$ for a given set of baseline amplitudes $\tilde{\boldsymbol{a}}$,

$$\tilde{\boldsymbol{m}} = \left(\mathsf{P}^{\mathsf{T}}\mathsf{C}_w^{-1}\mathsf{P}\right)^{-1}\mathsf{P}^{\mathsf{T}}\mathsf{C}_w^{-1}(\boldsymbol{d} - \mathsf{F}\tilde{\boldsymbol{a}}). \tag{4.20}$$

The output map in equation (4.20) can be understood as follows: we first clean the data by subtracting the solved baselines, $\boldsymbol{d} - \mathsf{F}\tilde{\boldsymbol{a}}$, and afterwards bin the processed data to a map. The binning operator, $\left(\mathsf{P}^{\mathsf{T}}\mathsf{C}_w^{-1}\mathsf{P}\right)^{-1}\mathsf{P}^{\mathsf{T}}\mathsf{C}_w^{-1}$, corresponds to the operator in equation (4.6), where the weights are now given by the white noise covariance.

Equations (4.18) and (4.20) summarise the destriping method. It is suitable for Planck-like scanning strategies with enough redundancy from observing the same pixels on the sky at different times. A given pixel must also be sampled with at least three sufficiently different polarisation directions in order to reliably solve for the Stokes I, Q, and U components in it. We asses the goodness of a pixel through the block-diagonal matrix

$$\mathsf{P}^{\mathsf{T}}\mathsf{C}_w^{-1}\mathsf{P}, \tag{4.21}$$

whose each 3×3 block represents the inverse of the white noise covariance within the pixel. If the ratio of the smallest to the largest eigenvalue for a block is below some predetermined limit, we exclude the pixel from our analysis. We should also use short enough baselines to capture correlated noise at frequencies below the knee frequency, as the destriping principle is built on a noise model that ignores correlated noise at frequencies above $1/N_{\mathrm{base}}$. The effect of destriping on simulated data is illustrated in Figure 4.2, where a map from the same dataset is presented with and without destriping.

Further, the two-step approach of destriping allows us to diverge from the maximum-likelihood solution to reduce systematics [**II**,**VI**]. As a consequence, the residual noise will be slightly increased. However, the residual noise is easier to account for in the later analysis steps than remaining systematics. Instead of weighting the different radiometers according to C_w, we can replace the values on the diagonal with horn-uniform weights, for example. They are defined as

$$C_{\mathrm{h}} = \frac{2}{\sigma_{\mathrm{M}}^2 + \sigma_{\mathrm{S}}^2}, \tag{4.22}$$

where σ_{M} and σ_{S} are the white noise sensitivities of M and S radiometers in a horn. This weighting will reduce the leakage from temperature to polarisation due to systematics, as the polarisation map will be solved solely from the difference of the M and S radiometer TODs. The change in the weighting scheme will also induce a modification to equation (4.21). The white noise covariance of a map is now obtained as

$$\left(\mathsf{P}^{\mathsf{T}}\mathsf{C}_{\mathrm{h}}^{-1}\mathsf{P}\right)^{-1}\mathsf{P}^{\mathsf{T}}\mathsf{C}_{\mathrm{h}}^{-1}\mathsf{C}_w\mathsf{C}_{\mathrm{h}}^{-1}\mathsf{P}\left(\mathsf{P}^{\mathsf{T}}\mathsf{C}_{\mathrm{h}}^{-1}\mathsf{P}\right)^{-1}. \tag{4.23}$$

We can also reduce the uncertainty in the baseline determination by applying a destriping mask when solving for the baseline amplitudes, since the signal error is the largest at the Galactic

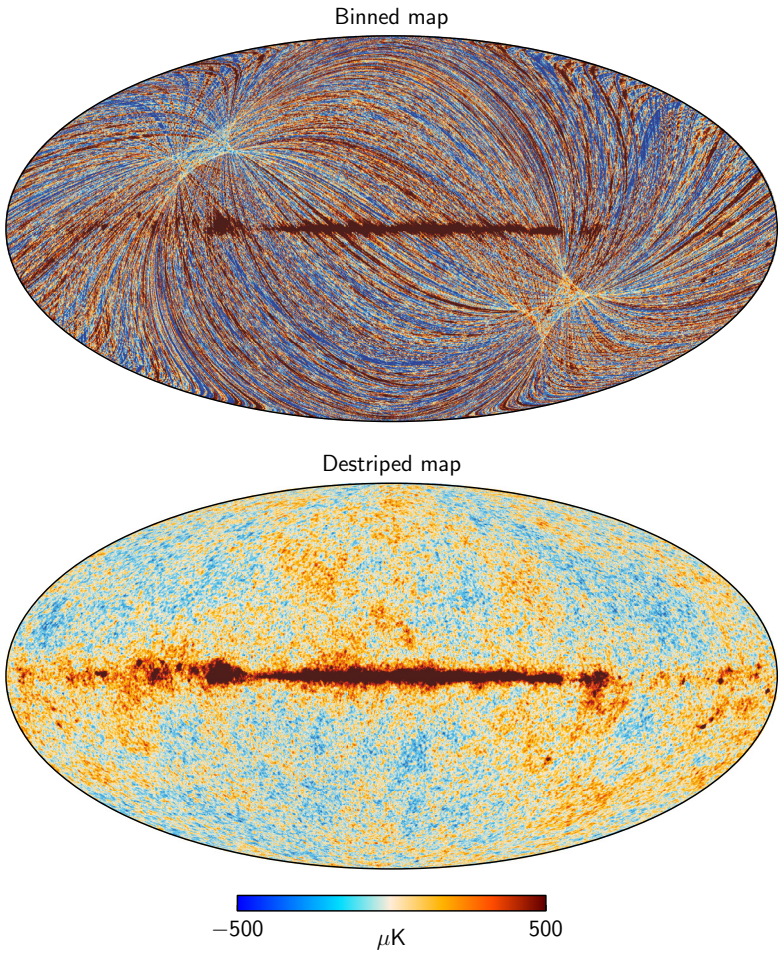

Figure 4.2: The effect of destriping on simulated data from paper [**II**]. *Top:* Binned map. *Bottom:* Destriped map. The binned map appears stripy due the $1/f$ noise, while the destriping brings out the CMB and foreground signals. In reality the binned map is exaggeratedly stripy, as the pre-processing already removes correlations on times scales longer than a pointing period. Maps are shown in Galactic coordinates.

plane. By masking out the strong foreground regions, we reduce the risk of identifying their signal falsely as noise and fitting baselines to those signal patterns. All the samples are again used when binning the final map. The residual noise will increase slightly due to masking.

4.4 Generalised destriping

If the noise spectrum is reliably known prior to the map-making, we can utilise this information to enhance the accuracy of noise removal. From the known noise spectrum $P(f)$, we can

calculate the noise prior C_a,

$$\mathsf{C}_a = \langle \boldsymbol{a}\boldsymbol{a}^\mathsf{T} \rangle, \tag{4.24}$$

to constrain baseline amplitudes. The noise prior contains effectively the correlations of noise sample averages, called reference baselines. The noise prior is constructed from the noise estimates as derived in [**II**].

Since the white noise and correlated noise components are assumed independent, the total noise covariance is

$$\mathsf{C}_n = \langle \boldsymbol{n}\boldsymbol{n}^\mathsf{T} \rangle \approx \mathsf{F}\mathsf{C}_a\mathsf{F}^\mathsf{T} + \mathsf{C}_w. \tag{4.25}$$

This introduces an additional term into equation (4.17) to be minimised,

$$\chi^2 = (\boldsymbol{d} - \mathsf{P}\boldsymbol{m} - \mathsf{F}\boldsymbol{a})^\mathsf{T}\, \mathsf{C}_w^{-1}\, (\boldsymbol{d} - \mathsf{P}\boldsymbol{m} - \mathsf{F}\boldsymbol{a}) + \boldsymbol{a}^\mathsf{T}\mathsf{C}_a^{-1}\boldsymbol{a}. \tag{4.26}$$

As before, we want to minimise equation (4.26) with respect to both $\boldsymbol{m}$ and $\boldsymbol{a}$. The baseline equation (4.18) acquires an extra term due to the noise prior, while the destriped map equation (4.20) remains the same. The baseline amplitudes are now obtained as a solution of

$$\left(\mathsf{F}^\mathsf{T}\mathsf{C}_w^{-1}\mathsf{Z}\mathsf{F} + \mathsf{C}_a^{-1}\right)\tilde{\boldsymbol{a}} = \mathsf{F}^\mathsf{T}\mathsf{C}_w^{-1}\mathsf{Z}\boldsymbol{d}, \tag{4.27}$$

where Z is defined in equation (4.19). Equation (4.27) can be solved through conjugate gradient method.

The extra constraint allows the extension of the destriping algorithm to very short baselines [**II, VI**]. Without the extra constraint, the amount of crossing points is not enough to determine the baseline amplitudes of short baselines. Additionally, the noise prior suppresses uncertainty in the baseline determination due to signal error, which increases rapidly with decreasing baseline length [**II, VI**]. Further, if the total noise covariance is of the form (4.25), the map estimate given by equations (4.27) and (4.20) is equal to the maximum-likelihood map in equation (4.11) [115]. When baseline length approaches the limit of one sample, the output map approaches the maximum-likelihood solution.

4.5 Low-resolution maps

Previous sections have introduced map-making algorithms used to process measured data into sky maps. The maps are commonly produced at resolution $N_{\mathrm{side}} = 1024$ for the Planck LFI to take full advantage of the fine angular resolution of the instruments. These high-resolution maps, however, cannot be utilised by all applications due to the sheer size of the problem at hand. For example, the power spectrum estimation was performed using different methods in the low-ℓ and high-ℓ regions [95]. The low-ℓ approach relies on the availability of noise covariance matrices to be described in Section 5.3. We are able to compute the noise covariance matrices at resolution $N_{\mathrm{side}} = 64$, but for many applications these matrices would be too large for an efficient usage. Therefore, we provide low-resolution maps and the corresponding noise covariance matrices at a target resolution of $N_{\mathrm{side}} = 32$ or lower.

Calculating the low-resolution maps directly at the low target resolution would be the simplest approach. However, this implies that the destriping is also performed at the target resolution, while the map-making methods introduced above are based on an assumption that the pixel substructure is negligible. Noise-wise this direct method would indeed be desirable as it will lead to the lowest residual noise in maps, but the signal error would blow up due to the pixel substructure [**II, VI**]. Hence, the direct method is inapplicable for realistic data,

and we need to downgrade the high-resolution maps to the low resolution. The resolution downgrading can be performed either in pixel or in harmonic domain, and they will lead to different signal and noise characteristics in the resulting maps.

In the map resolution downgrading two unwanted artefacts may arise: aliasing of power and ringing. They can be characterised as follows. Aliasing is related to the discrete nature of samples. Spherical harmonics discretised using the `HEALPix` form a linearly independent system up to $\ell_{\rm max} = 3N_{\rm side} - 1$. Hence, any power beyond $\ell = 3N_{\rm side}$ will be aliased as a power at the scales of interest. Visually ringing appears as wave-like patters in maps near sharp transitions in signal. Sharp cut-offs in harmonic expansions may generate ringing.

Pixel domain

The pixel space methods rely on combining high-resolution subpixels into larger low-resolution ones through weighted sums. Specifically, the downgrading is achieved by applying to the high-resolution map the operation

$$\mathsf{D} = \left(\mathsf{P}_{\rm low}^{\mathsf{T}}\mathsf{W}^{-1}\mathsf{P}_{\rm low}\right)^{-1}\mathsf{X}\left(\mathsf{P}_{\rm high}^{\mathsf{T}}\mathsf{W}^{-1}\mathsf{P}_{\rm high}\right), \tag{4.28}$$

where

$$X_{qp} = \begin{cases} 1, & p \text{ subpixel of } q \\ 0, & \text{otherwise} \end{cases} \tag{4.29}$$

sums the high-resolution pixels to the low-resolution ones, and matrix W describes the weights. The subscripts high and low refer to high- and low-resolution versions of the pointing matrix. The same matrix X is also used to downgrade the pointing matrix, $\mathsf{P}_{\rm low} = \mathsf{P}_{\rm high}\mathsf{X}^{\mathsf{T}}$. Thus, the downgraded map becomes

$$\tilde{\boldsymbol{m}}_{\rm low} = \mathsf{D}\tilde{\boldsymbol{m}}_{\rm high}. \tag{4.30}$$

For polarisation sensitive experiments we must take into account, when averaging the high-resolution pixels, that the polarisation Stokes Q and U vectors are coordinate-dependent quantities. Our implementation of the pixel domain downgrading includes a step of parallel transporting polarisation vectors from the high-resolution subpixels to the low-resolution pixel centres before averaging, which is not yet part of the standard `ud_grade` of `HEALPix` package.

- **Naive downgrading.** The naive method represents a special case of pixel domain methods with uniform weights, $\mathsf{W} = \mathbb{1}$. Concretely, we simply calculate the averages of the high-resolution subpixels. The downside of the approach is aliasing of power from small scales.

- **Noise-weighted downgrading.** In the noise-weighted scheme the weights are given by the white noise covariance, $\mathsf{W} = \mathsf{C}_{\boldsymbol{w}}$ [116]. We explicitly use the pixel space white noise covariance matrices given by equation (4.21) or its variant in the downgrading. The resulting map is analogous to a one that is directly binned onto the low target resolution from the data destriped at the high resolution. Compared to the naive downgrading, the noise-weighted scheme leads to lower residual noise, but stronger signal distortions, if samples are unevenly distributed within the large pixel. The noise-weighted method suffers also from aliasing.

Harmonic domain

Harmonic-space methods include a step of expanding the pixel domain representation of a map as spherical harmonics. Such an expansion can be convolved with a smoothing window to reduce aliasing from angular scales not supported by the target resolution. The smoothed expansion is then synthesised into a low-resolution map by sampling the expansion values at the new pixel centres. Explicitly, we apply to the high-resolution map the operation

$$\mathsf{S} = \mathsf{Y}_{\rm low}^{\dagger}\mathsf{K}\mathsf{Y}_{\rm high}, \tag{4.31}$$

where Y is the matrix that returns the spherical harmonic expansion of a map, $\boldsymbol{a} = \mathsf{Y}\boldsymbol{m}$, and K is the smoothing kernel describing the smoothing operation. Now, the downgraded map becomes

$$\tilde{\boldsymbol{m}}_{\rm low} = \mathsf{S}\tilde{\boldsymbol{m}}_{\rm high}. \tag{4.32}$$

- **Gaussian smoothing.** Gaussian smoothing is defined by a window function [117]

$$K_\ell = e^{-\frac{1}{2}\left[\ell(\ell+1)-s^2\right]\sigma^2}, \tag{4.33}$$

  where spin s is 0 for temperature and 2 for polarisation, and σ is defined through the beam FWHM, FWHM $= \sqrt{8\ln 2}\sigma$. The Gaussian window will provide gradual smoothing. However, it is not exactly zero at any finite ℓ, which may leave some power at scales unsupported by the target resolution. Figure 4.3 illustrates the shape of the Gaussian window for a beam whose FWHM is 440′. The Gaussian window clearly affects every multipole, and is non-zero at $3N_{\rm side}$.

- **Cosine smoothing.** Cosine smoothing limits the effect of window function to a band of multipoles. It is defined as [118]

$$K_\ell = \begin{cases} 1 & \ell \le \ell_1 \\ \frac{1}{2}\left[1 + \cos\left(\frac{(\ell-\ell_1)\pi}{\ell_2-\ell_1}\right)\right] & \ell_1 \le \ell \le \ell_2 \\ 0 & \ell \ge \ell_2, \end{cases} \tag{4.34}$$

  where parameters ℓ_1 and ℓ_2 are used to define the range of damping. Typical choices for the two parameters are $\ell_1 = N_{\rm side}$ and $\ell_2 = 3N_{\rm side}$, where $N_{\rm side}$ is the target resolution. The power is exactly zero above the ℓ_2. The band boundaries can be adjusted to make the smoothing either more gradual to reduce ringing or sharper to confine the window effects. Figure 4.3 illustrates the shapes of the cosine windows for two different ℓ_1 values, $\ell_1 = N_{\rm side}$ or $2N_{\rm side}$, while for both windows $\ell_2 = 3N_{\rm side}$. One provides more gradual smoothing, while the other leaves more multipoles unaffected.

Recap of downgrading methods

Figures 4.4 and 4.5 summarise the effects of different downgrading schemes on a simulated Planck LFI 70 GHz sky map. The input map shown on the top row of Figure 4.4 contains contributions from the CMB, the foregrounds, and the instrumental noise. The target resolution for the downgraded maps is $N_{\rm side} = 16$. Visual inspection of the map images does not reveal large differences within the classes of methods. All the approaches display generally

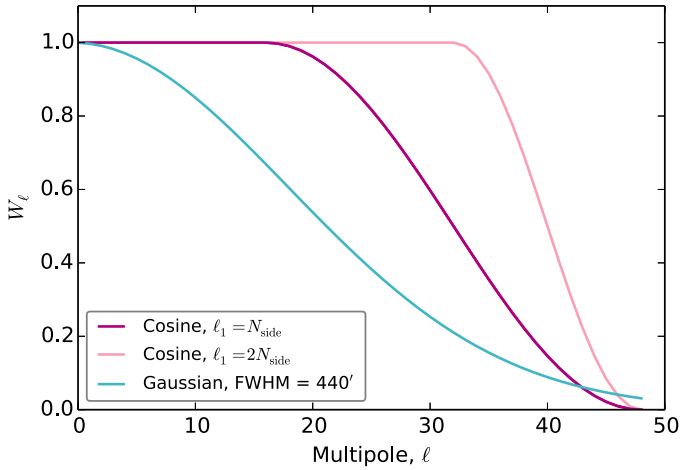

Figure 4.3: Examples of Gaussian and cosine window functions for the resolution $N_{\rm side} = 16$. The Gaussian windows is defined with the beam FWHM= 440′, while the two cosine windows differ by the ℓ_1 (either $\ell_1 = N_{\rm side}$ or $2N_{\rm side}$), but for both $\ell_2 = 3N_{\rm side}$. Gaussian window provides gradual smoothing, but leaves some power even at $\ell = 3N_{\rm side}$. The cosine windows leave a band of multipoles unaffected, and swiftly damp the power between ℓ_1 and ℓ_2.

the same broad features, only the maps downgraded in the harmonic domain appear smoother. The cosine smoothed maps show unexpectedly ringing around the Milky Way, and the ringing does not vanish even when ℓ_1 approaches zero. The used lower bound, $\ell_1 = N_{\rm side}$, was chosen such that the ringing does not appear too striking. The ℓ-space comparison in Figure 4.5, on the other hand, shows larger differences. Both pixel space methods suffer from aliasing above $\ell \sim 10$, while the application of smoothing windows clearly mitigate the problem.

Naturally, we can also combine different downgrading schemes to achieve suitable end products, as we did for the Planck 2015 analysis (see 4.6.2 for details). In the official scheme, we combined the noise-weighted downgrading with the Gaussian smoothing for the temperature component. This led to adequate low-resolution maps for the Planck 2015 publications. Applying the smoothing window to the Stokes Q and U components might be desirable in the future, as they also exhibit significant aliasing. The chosen scheme may lead to shifting of pixel centroids: in the regions where hit counts change rapidly, the large low-resolution pixel acquire a value based on the low-noise sub-pixels. This shifting will affect the frequency channels differently, and confuse the component separation.

Cosine smoothing seems beneficial based on many factors: it is simple, it affects only a band of multipoles, and it alleviates the aliasing effect. We have refrained from changing the official downgrading scheme for the time being. For the final Planck data release the official downgrading scheme will need to be revised.

4.6 Map-making for the Planck LFI

We have considered the different map-making aspects from the theoretical point of view so far. In this Section we will summarise the actual map-making procedure and the official

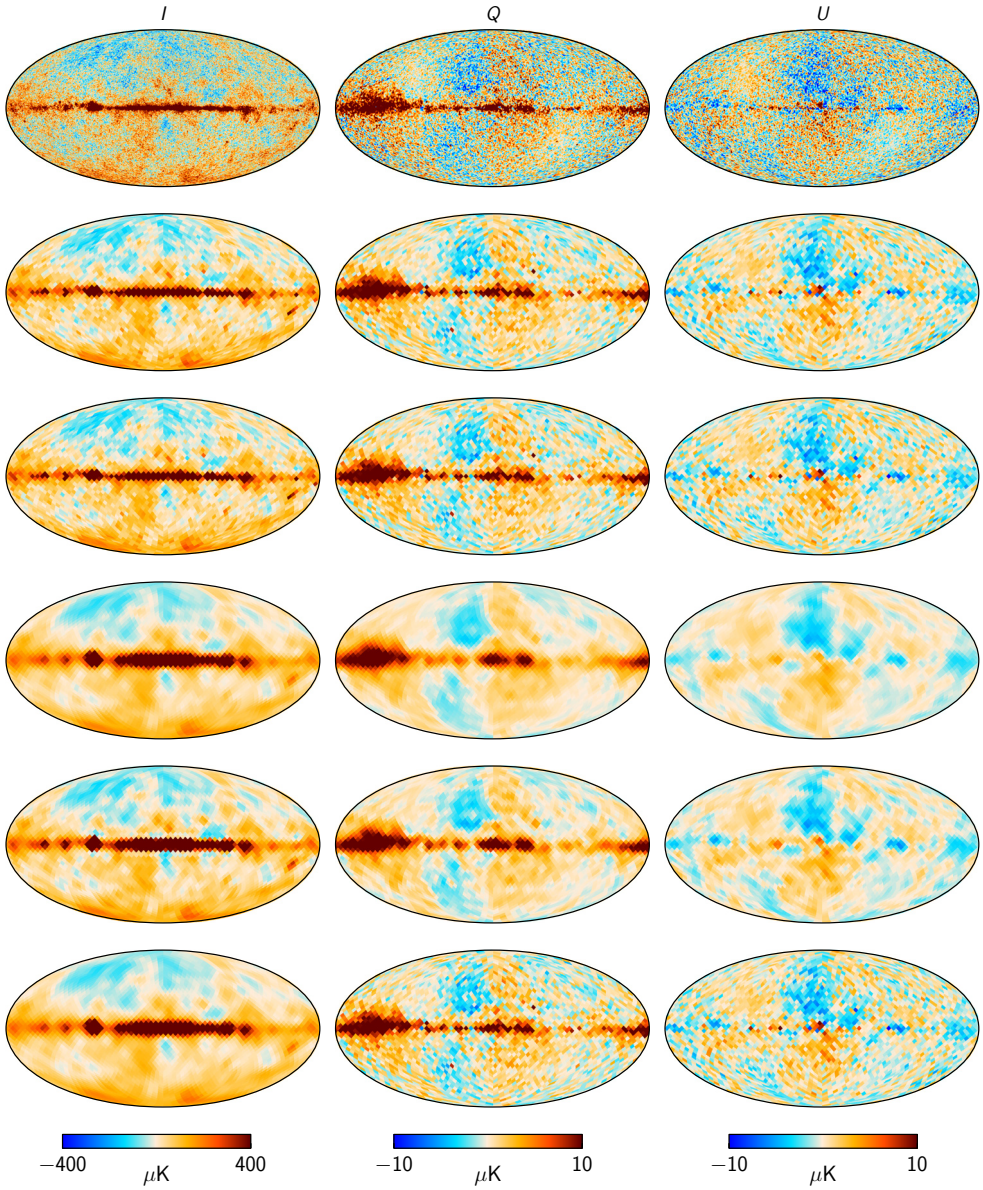

Figure 4.4: The effect of different downgrading methods on a simulated map. *First row:* Simulated high-resolution map for Planck LFI 70 GHz channel, which is used as an input for different downgrading schemes. The input map contains contributions from the CMB, the foregrounds, and the instrumental noise. The target resolution for the downgraded maps is $N_{\rm side} = 16$. *Second row:* Naive downgrading. *Third row:* Noise-weighted downgrading. *Fourth row:* Gaussian smoothing with a FWHM= 440′ beam. *Fifth row:* Cosine window smoothing with $\ell_1 = N_{\rm side}$ and $\ell_2 = 3N_{\rm side}$. *Sixth row:* Offical Planck 2015 downgrading scheme, which comprises of the noise-weighted downgrading and the Gaussian smoothing for the temperature component. The columns are the Stokes I, Q and U, respectively. All maps are shown in Galactic coordinates.

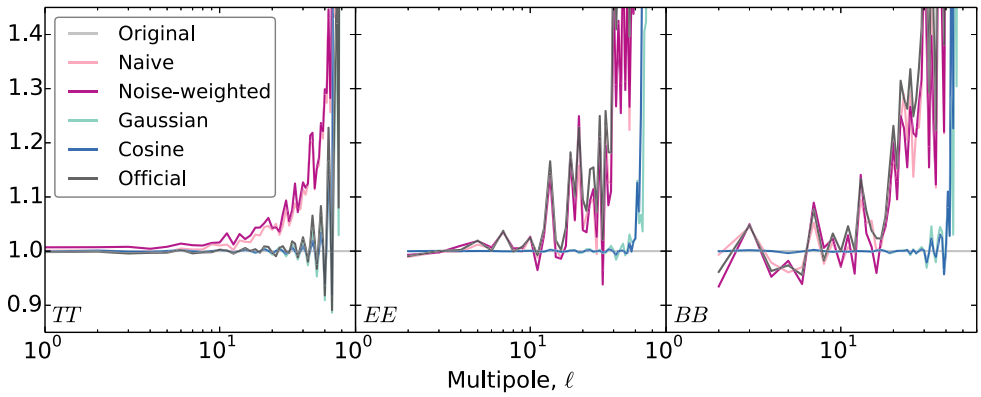

Figure 4.5: The effect of different downgrading methods on a simulated map in ℓ-space. We have first calculated the angular power spectra of each map shown in Figure 4.4 with `Anafast` of `HEALPix` package, and we display ratios for each map C_ℓ with the input map C_ℓ. For a more meaningful comparison we have deconvolved the polarised pixel window functions and possible smoothing windows from the downgraded map spectra. The pixel domain methods show aliasing above $\ell \sim 10$, while the harmonic domain methods leave more multipoles intact.

downgrading scheme applied in the Planck 2015 data release, as described in [**VI**].

4.6.1 High-resolution maps

The high-resolution maps from the Planck LFI data were produced using the `Madam` map-maker [115, **II**] designed for Planck-like experiments. `Madam` is build on the generalised destriping principle, introduced in Section 4.4. It takes as an input the calibrated and preprocessed timelines, the pointing information and the noise estimates, and returns as a primary output the sky maps of the Stokes I, Q and U components.

`Madam` offers us flexibility to control the accuracy of the output maps and the required computational burden through multitude of runtime parameters. As always, we aimed to remove the correlated noise as accurately as possible during the map-making, but also to reduce the effect of systematics to the extent possible during the `Madam` runs. The most critical parameter, the baseline length, controls the noise removal, while for instance the inclusion of a destriping mask and a modified weighting scheme alleviate the systematics. The parameter settings used in the Planck 2015 LFI map-making are justified in papers [**II**,**VI**] based on simulations.

Simulations presented in papers [**II**,**VI**] indicate that the residual noise decreases with decreasing baseline length, and hence it should be set as short as possible, given the finite computational resources. Using the noise prior, built from the noise parameters listed in Table 3.4, allowed us to reduce the baseline length well below one minute for more accurate noise removal. We applied the same prior throughout the entire mission assuming that the noise properties had remained stable enough. The decline of residual noise ceases mostly around 1 second baselines, hence we chose to destripe the 30 GHz maps with 0.25 second baselines, and the 44 and 70 GHz maps with 1 second baselines. The knee frequencies are higher for the 30 GHz channel, hence the shorter baselines. These baselines were found to be short enough

for nearly optimal noise removal.

However, such a short baselines will increase the signal error [**II**,**VI**]. By taking advantage of the `Madam`'s two-step approach, we can use a destriping mask during the baseline determination, even if all samples are used to bin the output maps. As the mask leaves a bit less data for solving the baselines, it will show up as a slightly increased residual noise. The destriping mask covered regions with strong foreground emissions, which additionally reduced errors arising from high signal gradients and the bandpass mismatch between detectors.

Furthermore, we can deviate from the maximum-likelihood estimates of baselines by altering the destriping resolution or the weighting scheme of different radiometers. Using too low destriping resolution will shoot up the signal error [**VI**], while the residual noise will decrease mildly for lower destriping resolutions. We chose to destripe and bin the maps at an equal resolution of $N_{\rm side} = 1024$. The applied horn-uniform weighting scheme, on the other hand, reduces leakage from temperature to polarisation by ensuring that the polarisation map is solved only from the difference of the two orthogonally-polarised radiometers in each horn [**VI**]. This also required the usage of uniform flagging: if a sample from one radiometer of a horn was unusable for science, we dropped the corresponding sample for the other radiometer too. The flagging was achieved by setting the white noise variance to infinity for the sample in question, effectively dropping out the sample from analysis, but maintaining the time sequence and the correct noise correlation properties. Flagged data arose due to the satellite's manoeuvring periods, missing data, gain saturations and the crossing of bright objects. Furthermore, `Madam`'s rcond parameter was used to exclude pixels with insufficient variations in the observing directions, since their signals cannot be decomposed into Stokes I, Q and U components reliably enough. The criterion has been rcond > 0.01, meaning that the ratio of the smallest to the largest eigenvalue of the matrix (4.21) or its variant for the pixel in question cannot exceed the given limit.

The 2015 release of the Planck data includes a large number of sky maps for the LFI channels available from the Planck Legacy Archive. We show examples of the Planck LFI full mission frequency maps in Figure 4.6.2, where the top row contains the intensity maps for each channel, and the two other rows consists of the Stokes Q and U maps, respectively. The spurious monopoles have been removed from all the released maps using the fitting procedure described in [**V**], but the polarisation maps are not corrected for the bandpass mismatch effect.

The LFI high-resolution maps have served as an input for many subsequent analysis steps including the component separation [93, 94] and the construction of a thermal SZ effect map [119].

4.6.2 Low-resolution maps

The Planck LFI low-resolution maps are constructed by downgrading the high-resolution maps described in Section 4.6.1 to the low target resolution. For most applications resolution $N_{\rm side} = 16$ is sufficient, but occasionally low-resolution maps are also used either at resolutions $N_{\rm side} = 8$ or 32.

We chose to downgrade the sky maps using the noise-weighted scheme combined with the Gaussian smoothing of the temperature component [**VI**], as described in Section 4.5. In practice one $N_{\rm side} = 16$ low-resolution map was constructed as follows. The high-resolution map was first noise-weighted to an intermediate resolution of $N_{\rm side,mid} = 32$. And afterwards, the Stokes I component was expanded in spherical harmonics and convolved with a Gaussian beam of FWHM $= 440'$ to prevent aliasing due to high frequency power in the map.

The low-resolution I map was then synthesised at the target resolution. The last step of resolution downgrading for the Stokes Q and U components, however, was performed by the naive averaging of intermediate resolution pixels, to minimise possible signal distortion. The chosen downgrading scheme would leave the corresponding noise covariance matrices, to be described in Section 5.3.6, singular. Hence, we regularised the problem by adding some white noise to both the maps and matrices. Specifically, we add 2 μK for the Stokes I component, and 0.02 μK for the Stokes Q and U.

Figure 4.6.2 illustrates the Planck 2015 full mission low-resolution maps for each LFI frequency channel, both in temperature and in polarisation. These maps contain also the bandpass mismatch effect.

The low-resolution maps for the full mission and a special mission, the full mission except for surveys 2 and 4, are available from the Planck Legacy Archive for each LFI frequency channel. In the Planck 2015 data release the LFI low-resolution maps were used as an input for the low-ℓ polarisation likelihood [95].

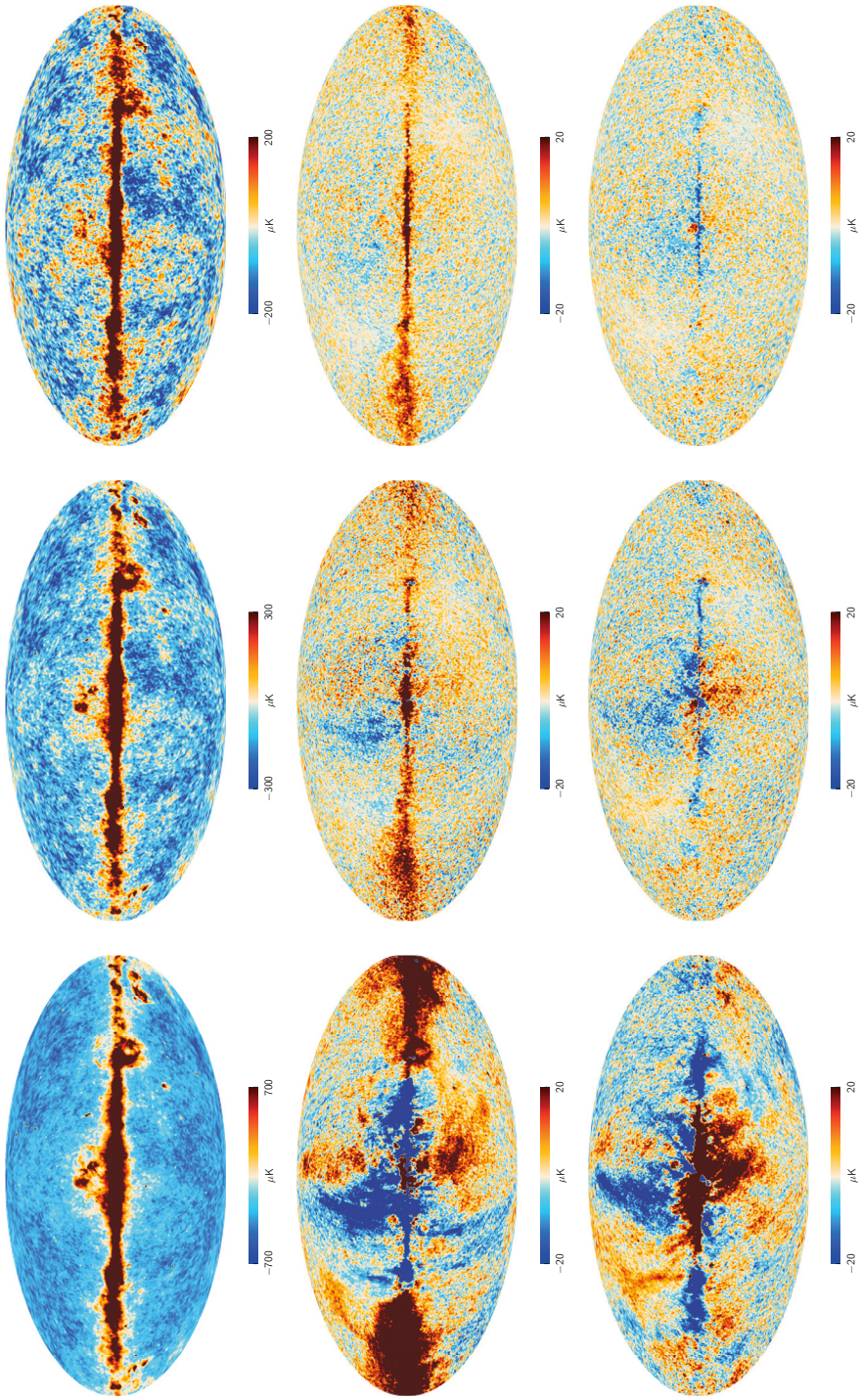

Figure 4.6: Planck 2015 full mission all sky maps at the LFI frequencies. *Left to right:* 30 GHz, 44 GHz and 70 GHz. *Top to bottom:* The Stokes I, Q and U component maps. The intensity maps have resolution $N_{\rm side} = 1024$, while polarisation maps have been downgraded to resolution $N_{\rm side} = 256$ and smoothed with a FWHM = 1° beam. All maps are shown in Galactic coordinates. Images: ESA and the Planck Collaboration.

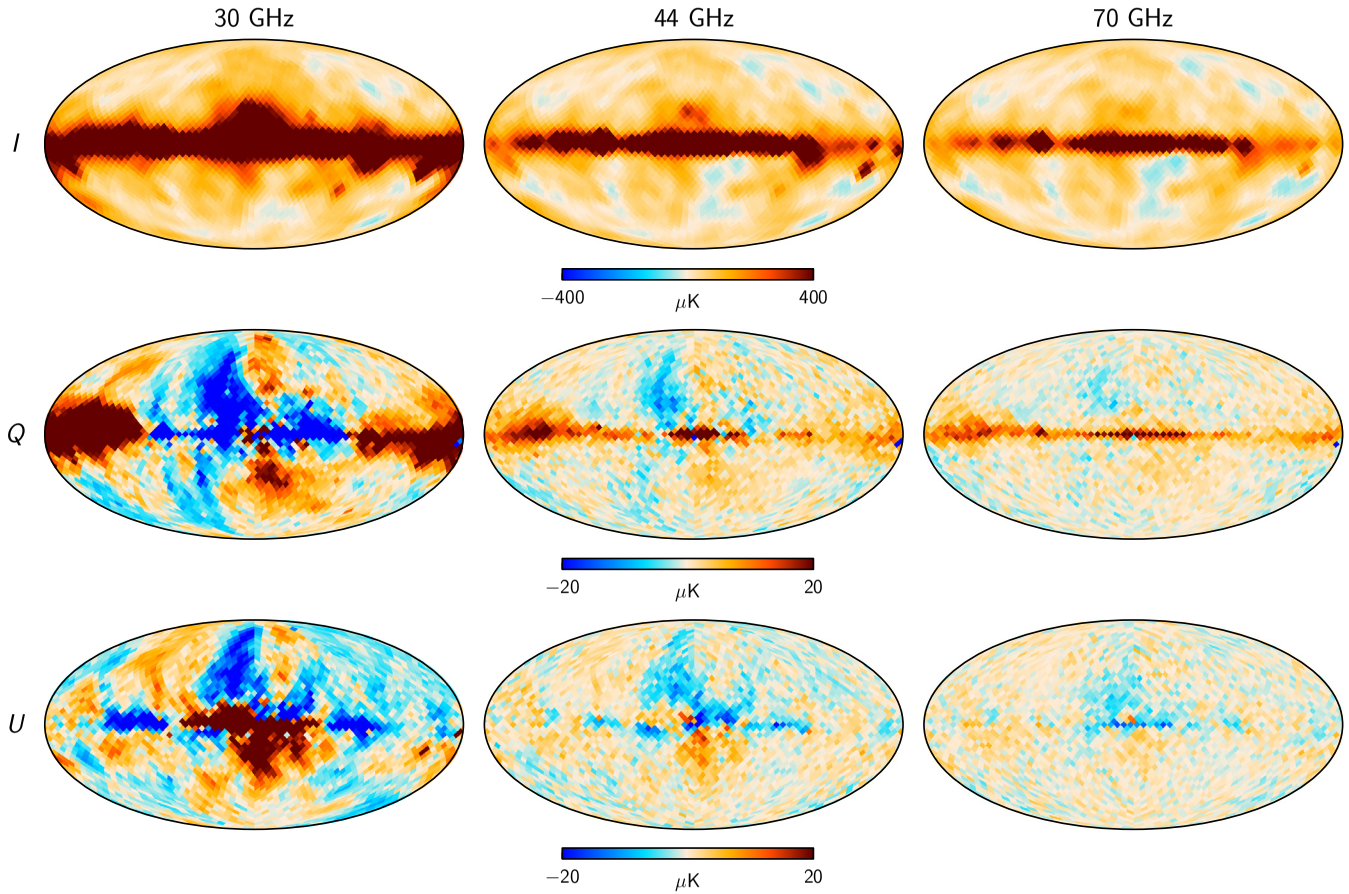

Figure 4.7: Planck 2015 full mission low-resolution maps at the LFI frequencies. *Left to right:* 30 GHz, 44 GHz and 70 GHz. *Top to bottom:* The Stokes I, Q and U component maps. The high-resolution maps have been downgraded to resolution $N_{\mathrm{side}} = 16$. All maps are shown in Galactic coordinates.

Chapter 5

Residual noise characterisation

The estimated map, $\tilde{\boldsymbol{m}}$, will always contain some degree of residual noise. The subsequent analysis steps, the component separation and the power spectrum estimation, require solid understanding of the noise residuals, as they will be critical for the reliability of the analysis.

We define the residual map as the difference between the input map $\boldsymbol{m}$ and the estimated map $\tilde{\boldsymbol{m}}$,

$$\Delta \boldsymbol{m} = \tilde{\boldsymbol{m}} - \boldsymbol{m}. \tag{5.1}$$

The difference is nontrivial, since part of the instrumental noise escapes our noise model, and slips to the resulting map. Destriping will pick out only the correlated noise below the baseline frequency, $f_{\mathrm{base}} = 1/t_{\mathrm{base}} \equiv f_{\mathrm{sample}}/N_{\mathrm{base}}$, and removes the statistically most probable realisation. We take signal errors to be absent, and consider that the difference (5.1) contains only noise residuals.

In this Chapter we will review three methods for modelling the noise residuals in the sky maps described in Chapter 4. The first method, half-ring difference maps, measures most directly the residual noise, while the other approaches, simulations and noise covariance matrices, rely on noise estimates at our disposal. We will conclude the Chapter by summarising the main results.

5.1 Half-ring maps

To characterise the residual noise directly at the map level, we construct half-ring maps from observations. Each pointing period is split in two — the first halves are used to construct one map, while the second halves create the other. If necessary, long pointing periods are first divided into 1 hour chunks at maximum. The two half-ring maps are then calculated using the same map-making pipeline as described in Section 4.6.1.

The resulting half-ring maps contain nearly identical sky signal, but due to instrumental noise they are not equal. The sky signal cancels out in the difference map revealing the residual noise. A given pixel of a half-ring noise map is then constructed as [**III**]

$$m_{\mathrm{hr}} = \frac{m_{\mathrm{hr1}} - m_{\mathrm{hr2}}}{w_{\mathrm{h}}}, \tag{5.2}$$

where m_{hr1} and m_{hr2} are pixel values from the two half-ring maps, and w_{h} is a weighting factor.

The weighting factor is given by [**III**]

$$w_{\rm h} = \sqrt{(h_1 + h_2)\left(\frac{1}{h_1} + \frac{1}{h_2}\right)}, \tag{5.3}$$

where h_1 and h_2 are the hit counts of $m_{\rm hr1}$ and $m_{\rm hr2}$ for the pixel in question, respectively. The weighting factor takes into account the differing hit counts in the two half-ring maps. If the hit counts are equal the weighting factor reduces to $w_{\rm h} = 2$, but for most pixels it is greater than 2.

Since the half-ring noise maps are independent of any noise model and constructed from the same data as the actual maps, they are valuable in characterising the residual noise. As the half-ring noise maps contain noise from the difference of two half-ring maps, the white noise will have correct statistics. But the half-ring noise maps will only capture the noise that is not correlated on time scales longer than the half of a pointing period.

Figure 5.1 shows the two half-ring maps and the corresponding half-ring noise map for the Planck 2015 LFI 70 GHz full mission temperature data as an example. As expected the two half-ring maps appear nearly identical, while the visual impression of the half-ring noise map is dominated by white noise.

5.2 Simulations

Simulations is a catch-all term for mimicking artificially the Planck data. We can simulate the data as truthfully as possible, or by singling out an issue for a refined study. We use the simulations, for example, to validate and verify the data analysis pipelines, to quantify the significance of a given effect, or to evaluate uncertainties in the analysis of the flight data. The Planck data releases have been supported by extensive simulation sets, containing maps of the CMB, the foreground components, the systematic effects and the instrumental noise, to meet the various needs in the data processing. But in this context, in order to estimate the residual noise after map-making, the simulated noise maps are the most vital.

We generate a simulated noise TOD based on the noise estimates described in Chapter 3.5.2. The noise TOD is further processed to a map using the map-making pipeline described in Section 4.6.1. To reduce scatter in results, we produce numerous noise realisations - the largest simulation sets may contain up to 10 000 noise Monte Carlo (MC) realisations. As the residual noise in the sky maps will eventually affect the power spectra estimates, we need to quantify its expected contribution, noise bias N_ℓ,

$$N_\ell^{XY} = \langle C_{\ell,\rm noise}^{XY} \rangle, \quad \text{where } X, Y = T, E \text{ or } B. \tag{5.4}$$

To estimate the noise biases, we compute angular power spectra from each noise MC map using `Anafast` from the `HEALPix` package, and average the spectra over all available realisations.

The Planck 2015 data release is supported with the 8th Full Focal Plane (FFP8) simulation set[1] [92]. The noise Monte Carlo simulations rely on the FFP8 noise estimates, and contain 10 000 realisations for each map type. The maps in the FFP8 set have been calculated with

[1]The simulations can be accessed from `http:crd.lbl.gov/cmb-data`.

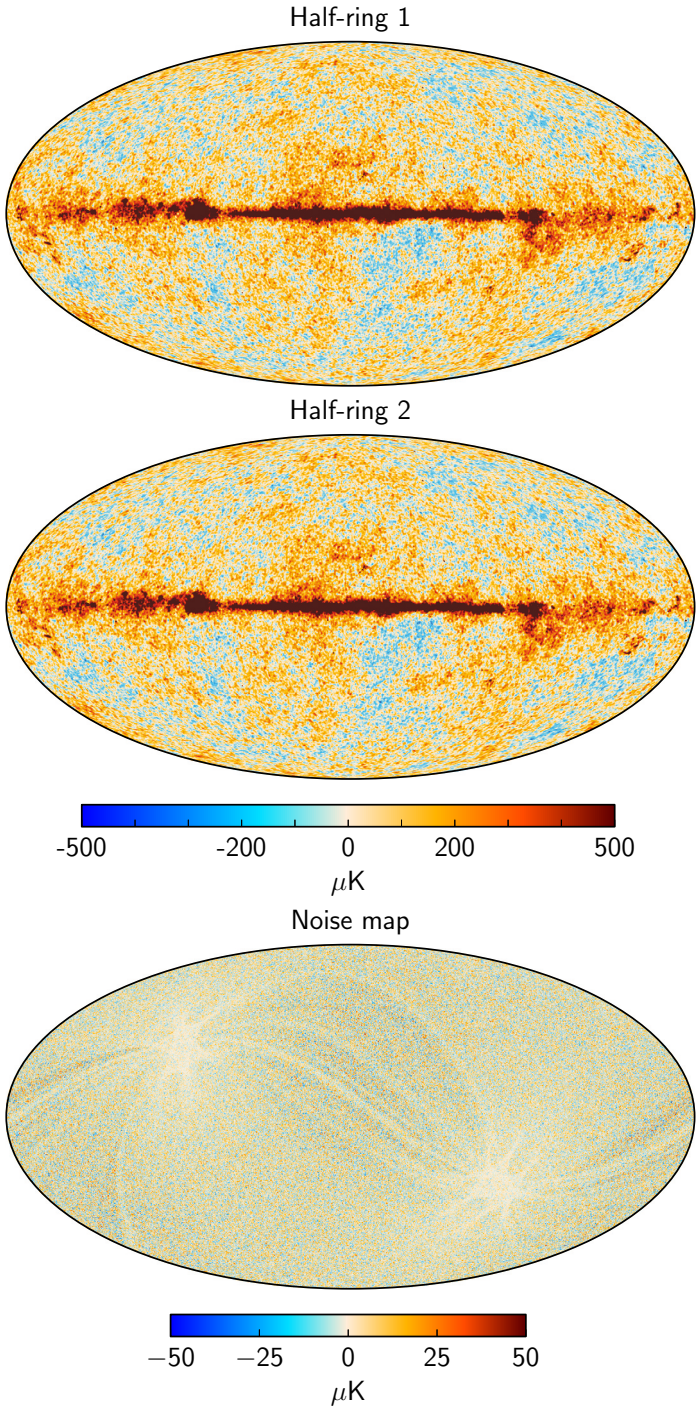

Figure 5.1: *Top & Middle:* Examples of the half-ring maps calculated from the Planck 2015 LFI 70 GHz full mission temperature data. The first and second halves of each pointing period are divided into two separate maps. *Bottom:* Noise map produced from the difference of the two half-ring maps above. The maps are shown in Galactic coordinates, and smoothed with a FWHM = 14′ beam to enhance their visual appearance.

`Madam/TOAST`, a `TOAST`[2] port of `Madam` [115, **II**], to allow for efficient calculations at high performance computing centres[3]. Figure 5.2 illustrates the full mission noise biases derived from the FFP8 simulations for each Planck LFI frequency channel. For comparison, we also show the corresponding estimates from the half-ring maps for the auto-spectra. The two estimates seem to agree broadly, but the half-ring spectra exhibit expectedly large scatter, as they are calculated just from single realisations. Hence, we omit the half-ring noise map cross-spectra from Figure 5.2 altogether, but they would be consistent with $\pm 1\sigma$ regions of the noise MCs.

5.3 Noise covariance matrices

To describe the pixel-pixel correlations of the residual noise, we construct noise covariance matrices (NCVM) in pixel space. The noise covariance matrix is defined as

$$\mathsf{N} = \langle \Delta \boldsymbol{m} \Delta \boldsymbol{m}^{\mathsf{T}} \rangle, \tag{5.5}$$

where $\Delta \boldsymbol{m}$ is the map residual from equation (5.1). The NCVMs will encode the full statistical understanding of the map uncertainty, when the noise is assumed Gaussian with zero mean and signal errors are considered absent. For unbiased map estimate, $\langle \tilde{\boldsymbol{m}} \rangle = \boldsymbol{m}$, equation (5.5) translates to

$$\mathsf{N} = \langle \tilde{\boldsymbol{m}} \tilde{\boldsymbol{m}}^{\mathsf{T}} \rangle - \boldsymbol{m}\boldsymbol{m}^{\mathsf{T}}. \tag{5.6}$$

Inserting the maximum-likelihood map estimate (4.11) above, the noise covariance matrix assumes the form

$$\mathsf{N} = \left(\mathsf{P}^{\mathsf{T}} \mathsf{C}_{\boldsymbol{n}}^{-1} \mathsf{P} \right)^{-1}. \tag{5.7}$$

For generalised destriping, we can replace the time domain noise covariance $\mathsf{C}_{\boldsymbol{n}}$ with the approximation from equation (4.25). The NCVM becomes

$$\mathsf{N} = \left(\mathsf{P}^{\mathsf{T}} \left(\mathsf{F} \mathsf{C}_{\boldsymbol{a}} \mathsf{F}^{\mathsf{T}} + \mathsf{C}_{\boldsymbol{w}} \right)^{-1} \mathsf{P} \right)^{-1}, \tag{5.8}$$

and by applying the Woodbury formula[4] the inverse of the noise covariance matrix can be determined as [115, 116]

$$\mathsf{N}^{-1} = \mathsf{P}^{\mathsf{T}} C_{\boldsymbol{w}}^{-1} \mathsf{P} - \mathsf{P}^{\mathsf{T}} \mathsf{C}_{\boldsymbol{w}}^{-1} \mathsf{F} \left(\mathsf{F}^{\mathsf{T}} \mathsf{C}_{\boldsymbol{w}}^{-1} \mathsf{F} + \mathsf{C}_{\boldsymbol{a}}^{-1} \right)^{-1} \mathsf{F}^{\mathsf{T}} \mathsf{C}_{\boldsymbol{w}}^{-1} \mathsf{P}. \tag{5.9}$$

To construct a noise covariance matrix, we only need as an input the noise estimates, the pointing information, and the baseline length. The different matrices in equation (5.9) are then constructed from these inputs.

5.3.1 Inversion

Implementing equation (5.9) in practice requires an inversion of a symmetric $3N_{\mathrm{pix}} \times 3N_{\mathrm{pix}}$ matrix for a polarisation sensitive experiment. We can write the inverse matrix as an eigen

[2] Time Ordered Astrophysics Scalable Tools (TOAST) package described in `https://theodorekisner.com/software/toast/index.html`.

[3] The work was divided between NERSC and CSC.

[4] $(\mathsf{A} + \mathsf{U}\mathsf{C}\mathsf{V})^{-1} = \mathsf{A}^{-1} - \mathsf{A}^{-1}\mathsf{U}\left(\mathsf{C}^{-1} + \mathsf{V}\mathsf{A}^{-1}\mathsf{U}\right)^{-1}\mathsf{V}\mathsf{A}^{-1}$

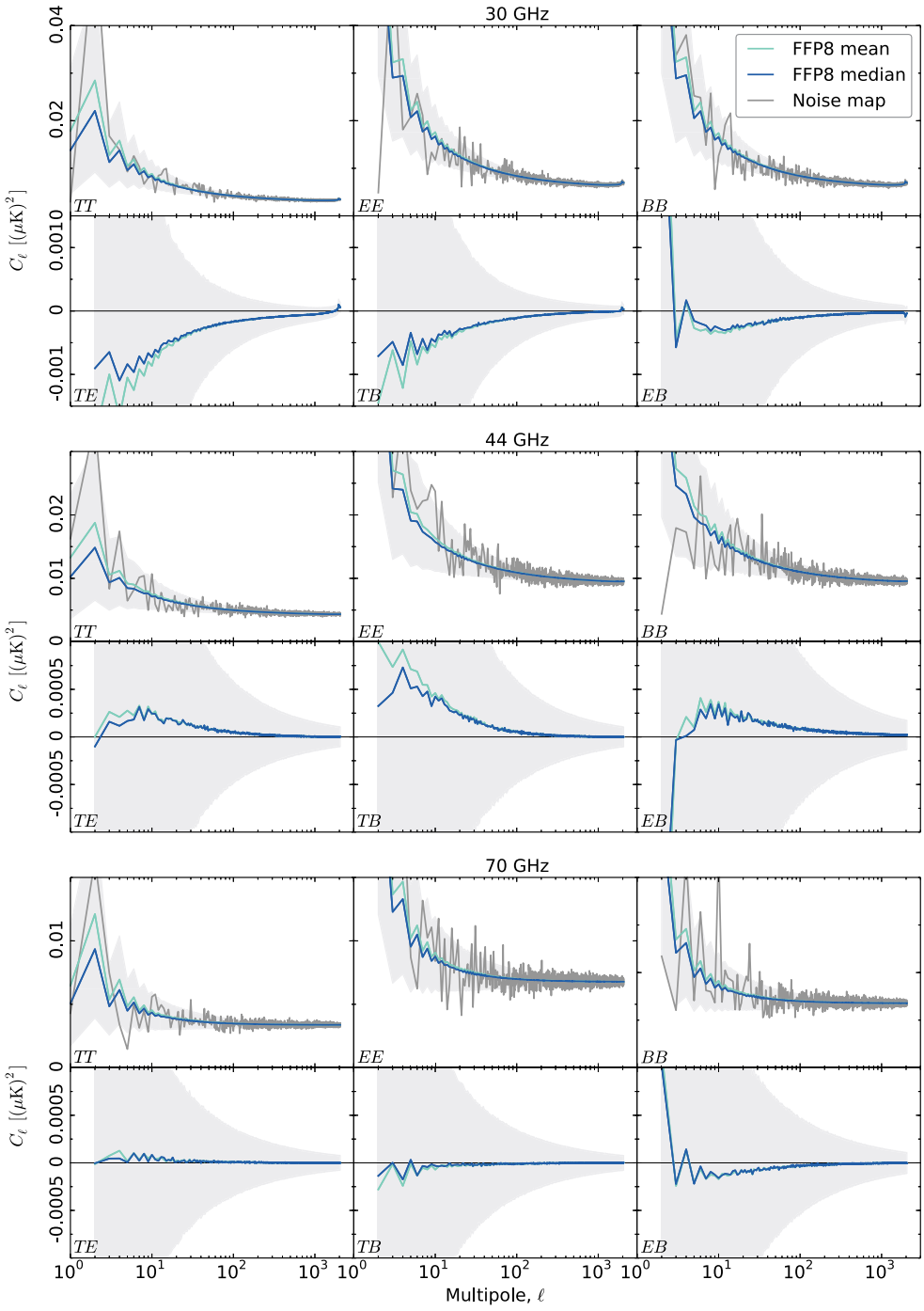

Figure 5.2: Noise bias levels at 30 GHz (*top*), 44 GHz (*middle*), and 70 GHz (*bottom*) from 10 000 FFP8 noise Monte Carlo realisations. The noise MC mean is plotted in cyan, median in blue, and $\pm 1\sigma$ region in light grey. For comparison, we show also estimates from the half-ring maps for the auto-spectra in darker grey. The cross-spectra for the half-ring maps are omitted due to broad scatter, as they are calculated just from single realisations, but they would be consistent with the light grey bands.

decomposition as

$$\mathsf{N}^{-1} = \sum_{i=0}^{3N_{\mathrm{pix}}-1} \frac{1}{\lambda_i} \hat{\boldsymbol{e}}_i \hat{\boldsymbol{e}}_i^{\mathsf{T}}, \tag{5.10}$$

where λ_i are the eigenvalues and $\hat{\boldsymbol{e}}_i$ the corresponding eigenvectors. The inverted matrix is obtained as

$$\mathsf{N} = \sum_{i=0}^{3N_{\mathrm{pix}}-1} \lambda_i \hat{\boldsymbol{e}}_i \hat{\boldsymbol{e}}_i^{\mathsf{T}}. \tag{5.11}$$

However, as the destriping algorithm cannot resolve the monopole of the temperature map, the noise covariance matrix becomes singular. To regularise the matrix, we project out the ill-determined mode corresponding to the smallest eigenvalue λ_0 [116],

$$\mathsf{N}_{\mathrm{reg}} = \sum_{i=1}^{3N_{\mathrm{pix}}-1} \lambda_i \hat{\boldsymbol{e}}_i \hat{\boldsymbol{e}}_i^{\mathsf{T}}. \tag{5.12}$$

The matrix size scales as $N_{\mathrm{pix}}^2 \sim N_{\mathrm{side}}^4$, thus the inversion becomes quickly computationally unfeasible for increasing N_{side}. Therefore, due to resource limitations, we cannot construct the NCVMs at the native map resolution. In practice, we limit the matrices to resolutions of $N_{\mathrm{side}} = 64$ and lower. One notch higher resolution would expand the matrix size yet again by a factor of 16, from 162 GB to nearly 2.6 TB.

5.3.2 Linear operations

As described in Section 4.5, we apply downgrading and smoothing operators, D and S, respectively, to the high-resolution maps when constructing the corresponding low-resolution maps. For consistency, the same operations must be applied to the noise covariance matrices.

For any linear operator L acting on a residual map $\Delta\boldsymbol{m}$,

$$\Delta\boldsymbol{m}_{\mathsf{L}} = \mathsf{L}\Delta\boldsymbol{m}, \tag{5.13}$$

we can write the covariance as

$$\mathsf{N}_{\mathsf{L}} = \langle \Delta\boldsymbol{m}_{\mathsf{L}} \Delta\boldsymbol{m}_{\mathsf{L}}^{\mathsf{T}} \rangle = \mathsf{L}\langle \Delta\boldsymbol{m}\Delta\boldsymbol{m}^{\mathsf{T}} \rangle \mathsf{L}^{\mathsf{T}} = \mathsf{L}\mathsf{N}\mathsf{L}^{\mathsf{T}}. \tag{5.14}$$

And further, decomposing N into its eigenvalues and eigenvectors, the modified noise covariance matrix becomes

$$\mathsf{N}_{\mathsf{L}} = \sum_i \lambda_i \mathsf{L}\boldsymbol{e}_i \boldsymbol{e}_i^{\mathsf{T}} \mathsf{L}^{\mathsf{T}} = \sum_i \lambda_i \left(\mathsf{L}\boldsymbol{e}_i\right)\left(\mathsf{L}\boldsymbol{e}_i\right)^{\mathsf{T}}. \tag{5.15}$$

Thus, as the above formulation justifies, it is sufficient to simply modify the eigenvectors [116].

5.3.3 Regularisation

If the chosen downgrading scheme includes a smoothing operation, this may lead to a singular covariance matrix, where the number of pixels is larger than the number of non-zero eigenvalues. If needed, we regularise the matrices by adding a small amount of white noise to the diagonal of the NCVMs. The level of regularisation noise is chosen to be 2 μK RMS for the Stokes I, and 0.02 μK RMS for the Stokes Q and U at $N_{\mathrm{side}} = 16$ resolution [**VI**].

5.3.4 Visualisation

Each row and column of N is a covariance map of the corresponding pixel. Hence, we can visualise the noise covariance matrices using the standard `HEALPix` tools. We normalise the covariance map into correlation coefficients,

$$\mathrm{Corr}(\Delta m_p, \Delta m_q) \equiv \frac{\langle \Delta m_p \Delta m_q \rangle}{\sqrt{\langle \Delta m_p^2 \rangle} \sqrt{\langle \Delta m_q^2 \rangle}}, \tag{5.16}$$

giving a value between 1 and -1. The correlation coefficient automatically acquires value 1 for the reference pixel. We further set the value in the reference pixel to zero to bring out the finer details of the correlation structure. For each image the reference pixel p is fixed, while q assumes all values between 0 and $N_{\mathrm{pix}} - 1$. A noise covariance matrix is illustrated in Figures 5.5 and 5.6 as an example.

5.3.5 Validation

Having both the half-ring noise maps and the massive set of noise simulations at hand, we can utilise them to study the validity of the noise covariance matrices. Direct insight is achieved through comparing the noise biases and the χ^2 testing.

Validation through noise bias

We can derive an analytic formula for the noise bias of a noise covariance matrix, and compare the prediction with the estimates from the half-ring noise maps and the noise MC simulations. They will reveal us at which angular resolutions the given noise covariance matrix functions properly. We defined the noise bias in equation (5.4) as the expectation value of the angular power spectra of noise only maps. We begin the derivation by applying the definition of angular power spectra from equation (2.14) in practice,

$$N_\ell^{XY} = \langle C_{\ell,\mathrm{noise}}^{XY} \rangle = \frac{1}{2\ell+1} \sum_{m=-\ell}^{\ell} \langle a_{\ell m}^X a_{\ell m}^{Y*} \rangle, \quad \text{where } X, Y = T, E \text{ or } B. \tag{5.17}$$

The spherical harmonic coefficients for a residual noise map can be written as

$$a_{\ell m} = \sum_{i=0}^{3N_{\mathrm{pix}}-1} Y_i^{\ell m} \Delta m_i, \tag{5.18}$$

and the noise bias becomes

$$N_\ell^{XY} = \frac{1}{2\ell+1} \sum_{m=-\ell}^{\ell} \sum_{i,j} Y_i^{X\ell m} N_{ij} Y_j^{Y\ell m*}. \tag{5.19}$$

Finally, we write the noise covariance matrix using the eigen decomposition from equation (5.11). We implement the noise bias calculation as [116]

$$N_\ell^{XY} = \frac{1}{2\ell+1} \sum_{m=-\ell}^{\ell} \sum_{i} \lambda_i \mathrm{Y}_\ell^X \hat{\boldsymbol{e}}_i \left(\mathrm{Y}_\ell^Y \hat{\boldsymbol{e}}_i \right)^\dagger. \tag{5.20}$$

Validation through χ^2 test

Another tool for comparing the residual noise estimates are the χ^2 tests. For each noise map $\boldsymbol{m}$, be it a half-ring noise map or a simulated noise map, we compute the reduced χ^2 value,

$$\chi^2 = \frac{\boldsymbol{m}^\mathsf{T}\mathsf{N}^{-1}\boldsymbol{m}}{N_\mathrm{dof}}, \tag{5.21}$$

where N is the noise covariance matrix, and N_dof is the degrees of freedom. For a polarisation sensitive experiment, the total number of the degrees of freedom is $3N_\mathrm{pix}$, but the presence of ill-conditioned eigenmodes will reduce the degrees of freedom accordingly. For unregularised smoothed noise covariance matrices we take the effective number of the degrees of freedom to equal the number of non-zero eigenvalues. The distribution of reduced χ^2 will peak at 1 for a covariance matrix that models perfectly the properties of given noise maps, and for differing values leaves room for improvements.

5.3.6 Planck LFI noise covariance matrices

The formulation of the noise covariance matrix in equation (5.9) describes the noise correlations of a sky map destriped and binned at equal resolutions using equations (4.19), (4.20), and (4.27). Since we create the maps at a native resolution of $N_\mathrm{side} = 1024$, we should construct the NCVMs at the same resolution and subsequently downgrade both to the target resolution for an exact agreement. This, however, is computationally unfeasible as the matrix size would be a colossal 10 PB. Therefore, we determine the noise covariance matrices at a suitable intermediate resolution, which is not necessarily the target resolution, and afterwards downgrade them to the target resolution. For consistency, we apply the same smoothing and downgrading operations to both the sky maps and the NCVMs. Additionally, the noise covariance matrix algorithm models neither the effect of destriping mask nor horn-uniform weighting, introduced to reduce systematics during the high-resolution map-making. We have performed series of simulations to assess the impact of these simplifications and the effect of different runtime parameters to the quality of noise covariance matrices. We first discuss the lessons learned from the simulations, and later recap the official pipeline and the Planck LFI NCVM results.

We used the FFP8 pipeline [92] to create an additional set of noise MC simulations, but now we let the map-making parameters to vary. We modified the baseline length, the destriping resolution, the weighting scheme, and the inclusion of destriping mask. We chose to perform the simulations for the 30 GHz channel, which required the least computational resources. For all parameter combinations we generated 100 noise-only map realisations. We also produced complementary noise covariance matrices by varying the baseline length and the destriping resolution in the computations. Figures 5.3 and 5.4 summarise the results from the simulations.

In Figure 5.3 the number of idealisations in the pipeline reduces from top to bottom. We include one effect at a time, such that the last panel illustrates a realistic simulation, except for the initial resolution of the NCVM. The starting point in panel A is an idealised case, where both the noise maps and the NCVM have been calculated at resolution $N_\mathrm{side} = 32$ with one sample baselines (0.03125 s). In panels B and C we have downgraded all products to resolution $N_\mathrm{side} = 16$ and regularised them, respectively. As expected, the effects of the downgrading and the regularisation are marginal on the χ^2 results. The baseline length is the key parameter in the noise covariance matrix computations, as seen from panels D–F. Reducing the baseline

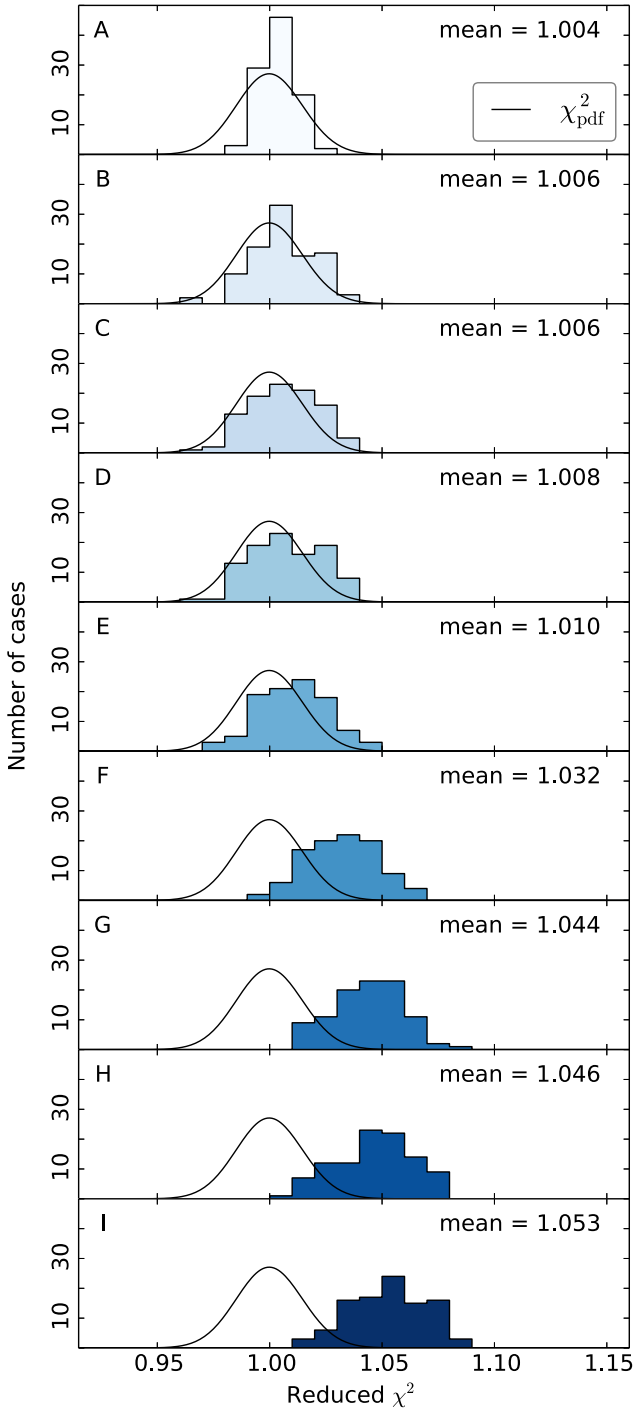

Figure 5.3: Reduced χ^2 statistics for the simulated Planck 2015 LFI 30 GHz full mission data. The level of idealisations decrease from top to bottom, one step at a time.
Panel A. An ideal simulation: both the noise covariance matrix and the noise Monte Carlo simulations are produced with equal parameter settings. The baseline length is 1 sample and the resolution is $N_{\rm side} = 32$.
Panel B. The ideal simulation is downgraded to $N_{\rm side} = 16$ using the official downgrading scheme.
Panel C. The regularisation noise is added to the downgraded products.
Panel D. The baseline length is increased to 8 samples in the noise MC.
Panel E. The baseline length is increased to 2 samples in the NCVM.
Panel F. The baseline length is increased to 8 samples in the NCVM.
Panel G. The destriping and map resolution is increased to $N_{\rm side} = 1024$ in the noise MC map-making.
Panel H. The horn-uniform weighting is applied in the noise MC map-making.
Panel I. The destriping mask is applied in the noise MC map-making. The parameter settings in panel I are equivalent to true LFI map and NCVM production, except for the initial resolution of NCVMs.

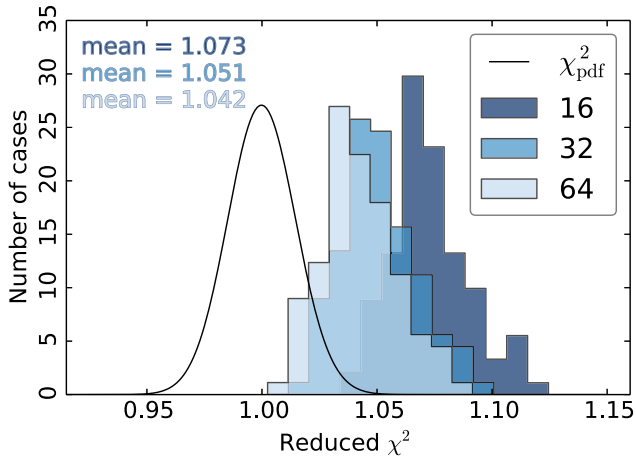

Figure 5.4: Reduced χ^2 statistics for simulated 30 GHz full mission data. The initial resolution of the noise covariance matrix is varied from $N_{\rm side} = 16$ to $N_{\rm side} = 64$.

length in the NCVM calculation below 0.25 s does improve the results, but at the same time computations become more demanding. Panels G–I show the effects of changing the destriping resolution to the realistic value of $N_{\rm side} = 1024$, using the horn-uniform weighting, and including the destriping mask, respectively, in the noise MC simulations. The last two effects contribute less than the baseline length and the destriping resolution.

We examine the impact of the initial resolution of the NCVM further in Figure 5.4, where the initial resolution of the matrix is varied from $N_{\rm side} = 16$ to 64. These reduced χ^2 tests have been calculated with the actual FPP8 simulation set. The highest initial resolution provides the best agreement. Increasing the initial resolution beyond $N_{\rm side} = 64$ is likely to improve results further, but the expected improvement would be small for a huge computational effort.

Based on the simulations, we decided to produce the LFI noise covariance matrices as follows. We used the `Madam/TOAST` implementation of the NCVM formalism, which takes as an input the pointing information and the noise estimates. The FFP8 noise estimates, described in section 3.5.2, were used in the calculations. The output of `Madam/TOAST` consists of the inverse noise covariance matrices defined by equation (5.9), specifically one inverse matrix per radiometer for a given time period. For all LFI frequency channels we used 0.25 second baselines and the matrices were calculated at the highest feasible resolution of $N_{\rm side} = 64$. The individual inverse matrices were merged together to form the actual inverse NCVMs. These inverse matrices were then inverted and subsequently downgraded to the target resolution, $N_{\rm side} = 16$, using the same downgrading scheme as applied to the maps. The noise-weighted downgrading scheme combined with the Gaussian smoothing for the temperature component leads to a singular covariance matrix: the number of pixels in the map is larger than the number of non-zero spherical harmonics after the smoothing operation, resulting in a significant number of zero eigenvalues. We regularise the products by adding a small amount of white noise to matrices. The level of regularisation noise was chosen to be 2 μK RMS for the Stokes I component, and 0.02 μK RMS for the Stokes Q and U at $N_{\rm side} = 16$ resolution. The 70 GHz full mission noise covariance matrix computation took approximately 6 hours of wall-clock

time and 23 000 CPU hours on the Cray XC40 at CSC.

The Planck 2015 data release included noise covariance matrices both for the full mission and the subset of data covering all surveys except 2 and 4. These NCVMs are available from the Planck Legacy Archive. Figure 5.5 illustrates the II, QQ and UU elements of the Planck 2015 LFI 70 GHz full mission noise covariance matrix for five different reference pixels. The reference pixel is located on the north ecliptic pole on the first row, and step by step moves towards the ecliptic, presented on the last row, along a meridian. The strongest correlations are seen with the neighbouring pixels, and along the scanning directions. Moreover, the correlation pattern changes significantly as the reference pixels is altered. Figure 5.6, on the other hand, illustrates the correlation of a single pixel with the rest of the sky as described by the LFI 70 GHz full mission noise covariance matrix. The reference pixel is 1248 in the `HEALPix` nested pixelisation scheme at $N_{\mathrm{side}} = 16$ resolution. The noise covariance matrix has been normalised to show correlation coefficients, and the value in the reference pixel is set to zero to highlight the finer details of the correlation structure.

In the Planck 2015 analysis the LFI noise covariance matrices have been used in the low-ℓ polarisation likelihood along with the corresponding low-resolution maps [95]. The likelihood was based on the LFI 70 GHz low-resolution maps cleaned with the LFI 30 GHz and the HFI 353 GHz data.

5.4 Comparing the residual noise estimates

At low multipoles we have three complementary methods for characterising the residual noise: the noise covariance matrices, the FFP8 noise simulations and the half-ring noise maps. Figures 5.7 and 5.8 compare these estimates against each other. Figure 5.7 shows the noise bias estimates for all methods. As there is only one half-ring noise map realisation, its spectrum shows much stronger variations than the other estimates. All the methods seem to agree broadly. At places the noise bias derived from the noise covariance matrix underestimates the true noise level indicated by the FFP8 simulations. Figure 5.8 illustrates the reduced χ^2 statistics for the Planck 2015 LFI full mission noise covariance matrices. The χ^2 test were calculated for 10 000 FFP8 noise MC realisations, and for comparison with the half-ring noise map also. For the LFI 70 GHz channel, which is the most important for the cosmological parameter estimation, the noise covariance matrix seems to model the residual noise most precisely.

Figures 5.2 and 5.9 compare the high-resolution residual noise estimates: the half-ring noise maps and the FFP8 simulations. The noise biases were found to agree well. Figure 5.9, on the other hand, compares the half-ring noise maps and the FFP8 simulations as a fraction of the white noise level in the high-ℓ region. The mean C_ℓs were calculated for the multipole range $\ell = 1150$–1800. Both the simulations and the half-ring noise maps predict slightly higher noise than the white noise estimates, which indicates that there is some residual $1/f$ noise even in the high-ℓ region. The error bars on the noise simulations include only the statistical variation.

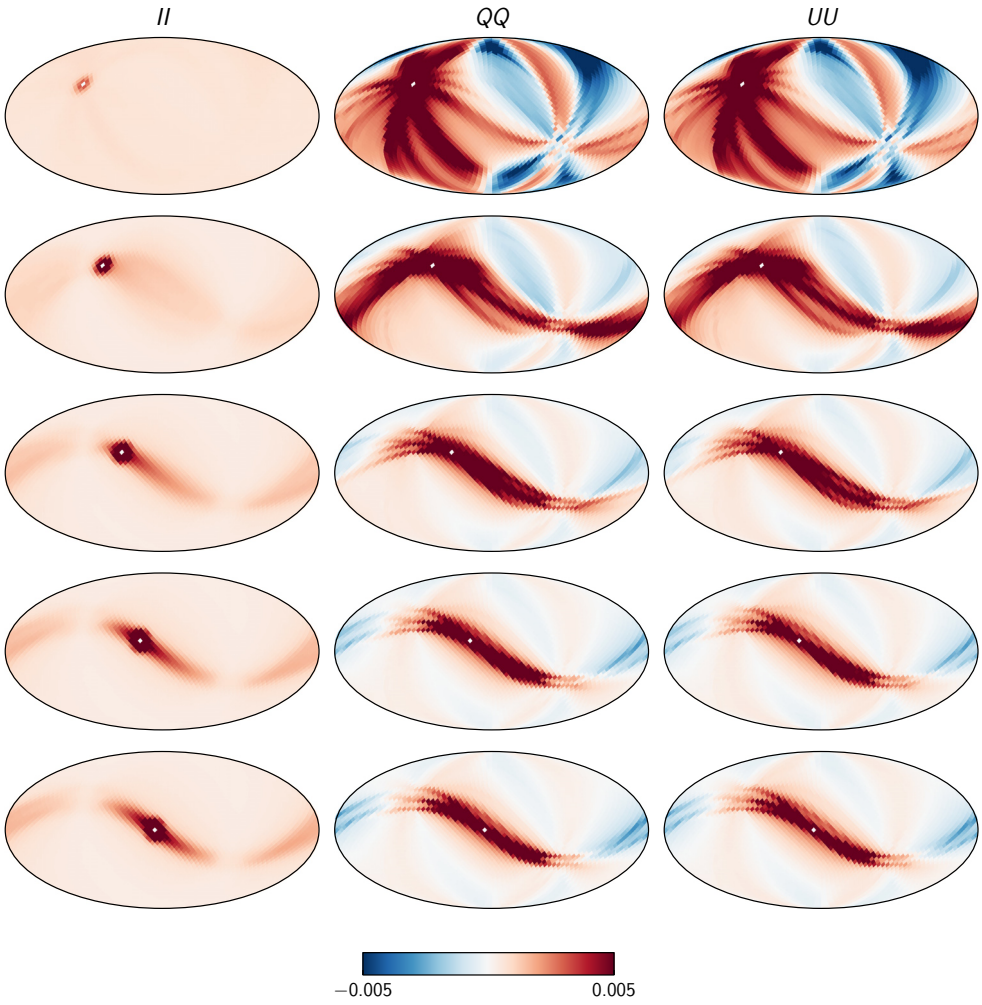

Figure 5.5: The II, QQ and UU elements of the Planck 2015 LFI 70 GHz full mission noise covariance matrix for five different reference pixels (*top* to *bottom*). The noise covariance matrix has been normalised to show the correlation coefficients, and the reference pixel is set to zero to highlight the finer details of the correlation structure. As the reference pixel moves from the north ecliptic pole to the ecliptic, the correlation pattern changes significantly. The noise covariance matrix is shown in Galactic coordinates.

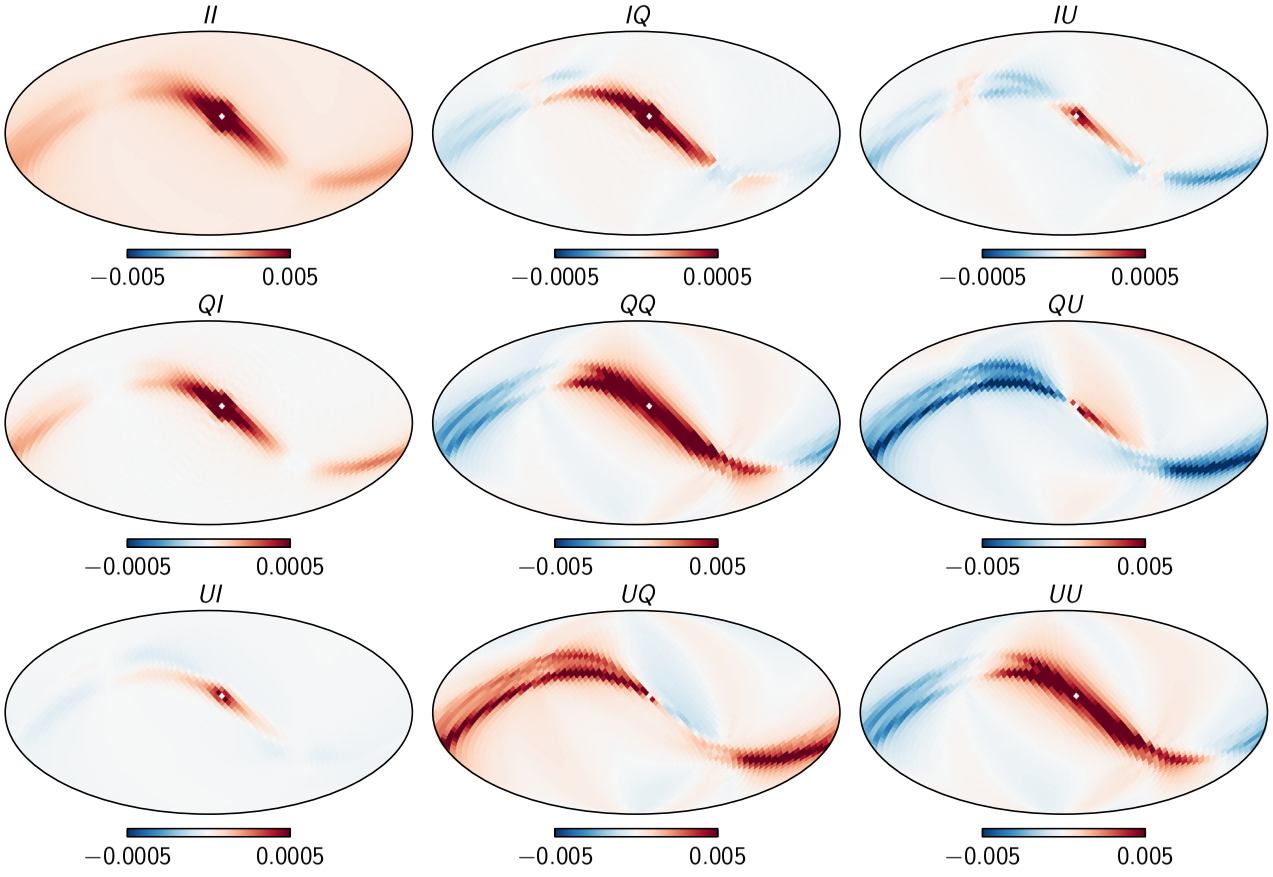

Figure 5.6: The correlation of a single pixel with rest of the sky as described by the Planck 2015 LFI 70 GHz full mission noise covariance matrix. The reference pixel in the `HEALPix` nested pixelisation scheme is 1248. The noise covariance matrix has been normalised to show the correlation coefficients. The value in the reference pixel is set to zero to highlight the finer details of the correlation structure. The noise covariance matrix is shown in Galactic coordinates.

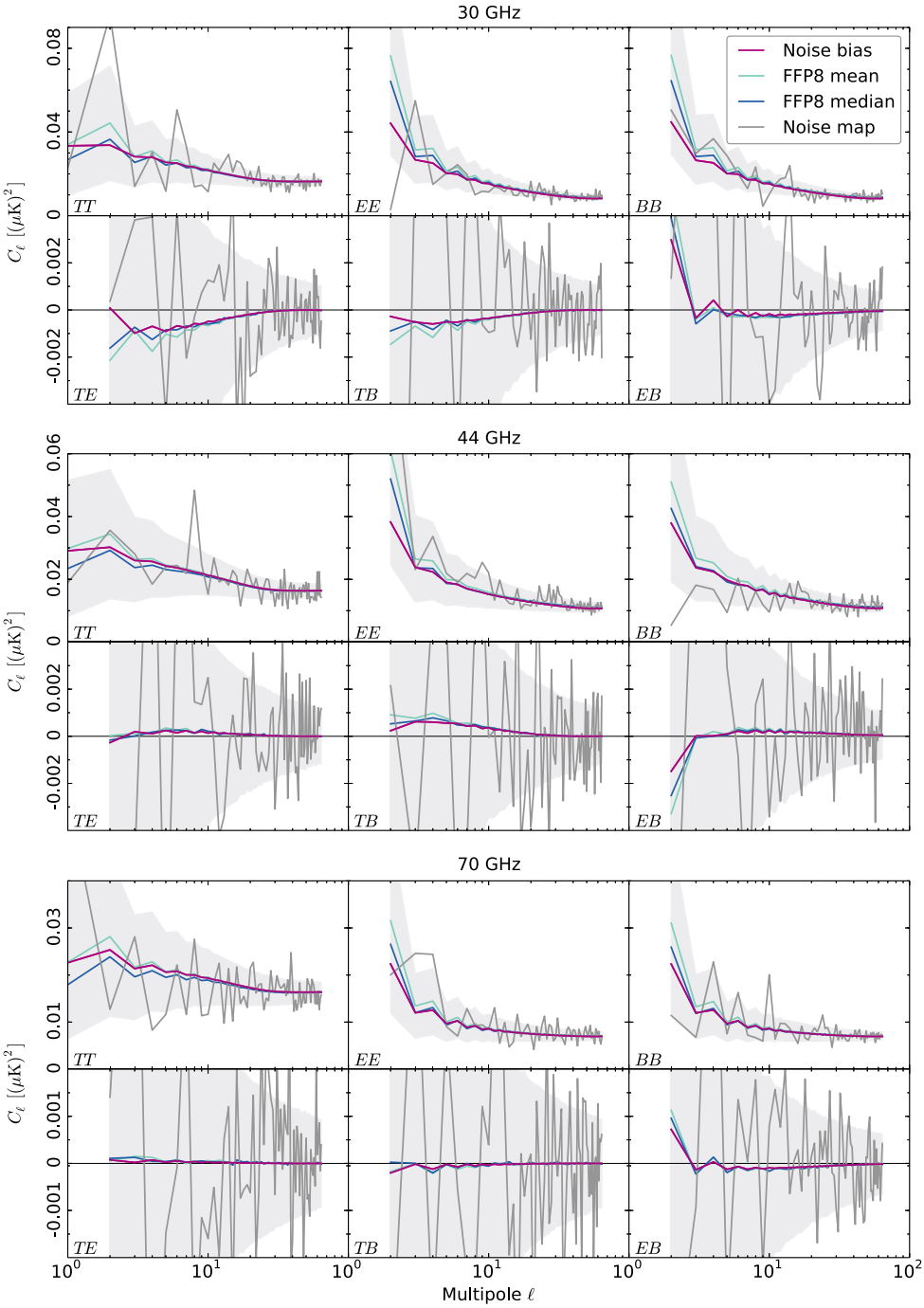

Figure 5.7: Noise bias levels at 30 GHz (*top*), 44 GHz (*middle*), and 70 GHz (*bottom*). The noise biases from the Planck 2015 LFI full mission noise covariance matrices are plotted in purple, the noise MC statistics from 10 000 FFP8 simulations are plotted in cyan (for the mean), blue (median) and lighter grey (±1 sigma region), as well as the estimate from the half-ring noise map in darker grey.

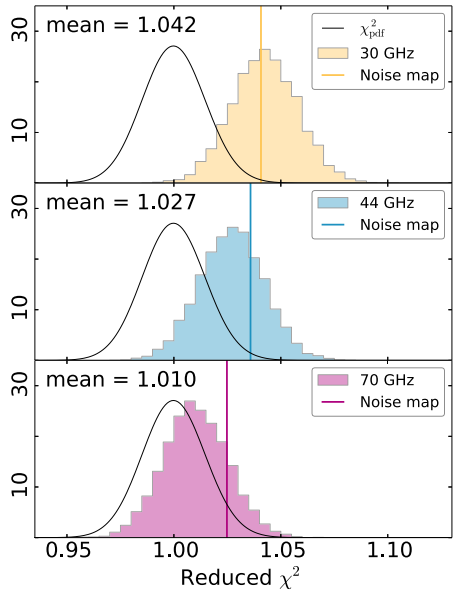

Figure 5.8: Reduced χ^2 statistics for the Planck 2015 LFI full mission noise covariance matrices. The χ^2 test have been calculated for 10 000 FFP8 noise MC realisations. Vertical lines mark the reduced χ^2 value for the half-ring noise maps.

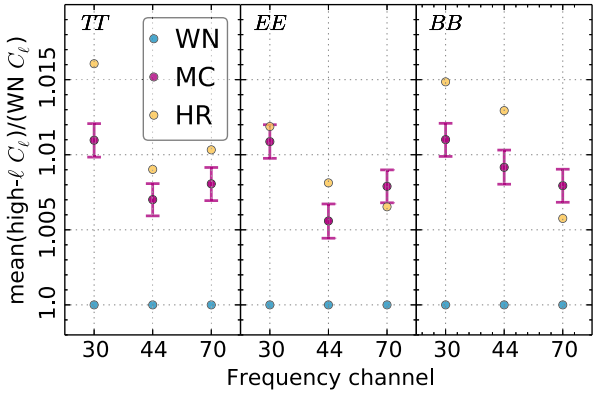

Figure 5.9: Comparing residual noise estimates for Planck 2015 release at high multipoles, as a fraction of white noise level (blue). The orange dots show estimates from the half-ring maps, while the purple dots illustrate the mean of 10 000 FFP8 noise simulations. The error bars include only the statistical variation. For the half-ring maps and the noise simulations the shown values have been calculated as the mean of the noise spectra for the range ℓ = 1150–1800.

Chapter 6

Conclusions

The cosmic microwave background carries a wealth of cosmological information. Planck was the most recent satellite mission to map the microwave sky. Planck's unprecedented combination of sensitivity, angular resolution and frequency coverage with full sky measurements have offered us an unparalleled view of the cosmos. As the precision of measurements has increased tremendously since the first CMB observations, the need for developing sophisticated algorithms to tackle the data analysis work has also been evident. This thesis discussed two main topics in the Planck analysis pipeline: the map-making and the residual noise estimates with emphasis on the noise covariance matrices.

Map-making serves as a crucial step for both data reduction and noise removal, but also allows us to inspect the collected data visually. The presence of correlated low-frequency noise in the Planck data has motivated the destriping approach to the map-making. A destriper models the correlated noise as a sequence of constant offsets, called baselines. For the Planck LFI map-making we have adopted the `Madam` map-maker as our standard tool. `Madam` is built on the generalised destriping principle, which can additionally employ prior information on the noise properties to enhance the accuracy of noise removal. Based on the noise and signal simulations, we chose to destripe the Planck 2015 pre-processed data at the resolution of $N_{\mathrm{side}} = 1024$ using 0.25 second baselines for the Planck LFI 30 GHz channel, and 1 second baselines for the 44 and 70 GHz channels. These values were shown to achieve nearly optimal noise removal, while keeping the signal error under control, provided that a destriping mask was applied. To reduce unwanted systematics further, we also utilised the horn-uniform weighting and flagging. We do not expect major changes in the map-making pipeline for the final round of Planck data analysis.

The estimated maps contain always some degree of residual noise. The analysis steps following the map-making, especially the component separation and the power spectrum estimation, require solid understanding of those residuals. We have three different methods at our disposal. The half-ring noise maps characterise the residual noise directly at the map level, while the noise simulations and the noise covariance matrices model the residual noise based on noise estimates. Noise covariance matrices, describing the pixel-pixel correlations, encode in theory the full statistical information of the residual noise. The Planck 2015 data release was supported by the half-ring noise maps, the FFP8 simulation set containing 10 000 noise maps for each map type, and the set of noise covariance matrices.

The noise covariance matrices at the native map resolution of $N_{\mathrm{side}} = 1024$ would be, how-

ever, of colossal size, and impossible to be utilised in the subsequent analysis steps. Therefore, we provide a low-resolution dataset consisting of low-resolution maps and corresponding noise covariance matrices at a suitable resolution of $N_{\mathrm{side}} = 16$. We chose to downgrade the high-resolution sky maps using the noise-weighted scheme combined with the Gaussian smoothing of the temperature component. The chosen downgrading scheme leaves the corresponding noise covariance matrices singular. Hence, we regularised the problem by adding some white noise to both products. For the Planck legacy release, the downgrading scheme will require a revision. Will the noise-weighted scheme still remain preferable, or does the cosine smoothing perform better? At least we should consider applying the smoothing window to the Stokes Q and U components also.

We used the `Madam/TOAST` implementation to produce the Planck 2015 noise covariance matrices. They were first constructed at an initial resolution of $N_{\mathrm{side}} = 64$ using 0.25 second baselines for all LFI channels. Afterwards we downgraded the matrices to the target resolution with the same downgrading scheme as applied to the maps, including also the regularisation step. In the coming data analysis round decreasing baseline length below 0.25 second, computational resources permitting, would improve results a little. The residual noise estimates from the three methods seem to show good agreement.

The final results from the Planck collaboration are expected in 2016, and improvements are anticipated especially due to treatment of low-ℓ systematics. But already Planck has had a major impact in the fields of cosmology and astrophysics. The 2015 Planck data remains in excellent agreement with the cosmological standard model: the Universe is flat with nearly scale-invariant adiabatic density fluctuations and is composed of dark energy, dark matter, baryons, electrons, neutrinos and photons. If there is new physics to be discovered beyond the ΛCDM model, its signatures in the CMB are very weak and beyond the reach of current datasets. From the future CMB missions we do not expect great advances from the temperature measurements, but detailed studies of the CMB electromagnetic spectrum and the possible discovery of B-mode polarisation would open up new observational frontiers.

Bibliography

[1] A. Einstein. Zur Elektrodynamik bewegter Körper. *Ann. Phys.*, 322:891–921, 1905.

[2] Bureau International des poids et mesures. The International System of Units (SI), 8th edition. http://www.bipm.org/en/publications/si-brochure/, 2006; updated in 2014.

[3] A. A. Penzias and R. W. Wilson. A Measurement of Excess Antenna Temperature at 4080 Mc/s. *Astrophys. J.*, 142:419–421, 1965.

[4] R. H. Dicke, P. J. E. Peebles, P. G. Roll, and D. T. Wilkinson. Cosmic Black-Body Radiation. *Astrophys. J.*, 142:414–419, 1965.

[5] R. K. Sachs and A. M. Wolfe. Perturbations of a Cosmological Model and Angular Variations of the Microwave Background. *Astrophys. J.*, 147:73, 1967.

[6] J. Silk. Cosmic Black-Body Radiation and Galaxy Formation. *Astrophys. J.*, 151:459, 1968.

[7] P. J. E. Peebles and J. T. Yu. Primeval Adiabatic Perturbation in an Expanding Universe. *Astrophys. J.*, 162:815, 1970.

[8] G. F. Smoot, et al. Structure in the COBE differential microwave radiometer first-year maps. *Astrophys. J. Lett.*, 396:L1–L5, 1992.

[9] Planck Collaboration: P.A.R. Ade et al. Planck 2015 results. XIII. Cosmological parameters. *ArXiv e-prints*, arXiv:1502.01589, 2015.

[10] G. Lemaître. Un Univers homogène de masse constante et de rayon croissant rendant compte de la vitesse radiale des nébuleuses extra-galactiques. *Ann. Soc. Sci. Bruxelles*, 47:49–59, 1927.

[11] G. Lemaître. Expansion of the universe, A homogeneous universe of constant mass and increasing radius accounting for the radial velocity of extra-galactic nebulae. *MNRAS*, 91:483–490, 1931.

[12] J. C. Mather, et al. A preliminary measurement of the cosmic microwave background spectrum by the Cosmic Background Explorer (COBE) satellite. *Astrophys. J. Lett.*, 354:L37–L40, 1990.

[13] The Planck Collaboration: J. Tauber et al. The Scientific programme of Planck. *ArXiv e-prints*, astro-ph/0604069, 2006.

[14] G. Gamow. The Origin of Elements and the Separation of Galaxies. *Phys. Rev.*, 74(4): 505–506, 1948.

[15] E. Hubble. A Relation between Distance and Radial Velocity among Extra-Galactic Nebulae. *Proc. Nat. Acad. Sci.*, 15:168–173, 1929.

[16] A. Einstein. Die Feldgleichungen der Gravitation. *Preuss. Akad. Wiss.*, pages 844–847, 1915.

[17] G. Gamow. Expanding universe and the origin of elements. *Phys. Rev.*, 70:572–573, 1946.

[18] R. A. Alpher, H. Bethe, and G. Gamow. The Origin of Chemical Elements. *Phys. Rev.*, 73(7):803–804, 1948.

[19] K. A. Olive et al. Review of Particle Physics. *Chin. Phys.*, C38:090001, 2014.

[20] R. A. Alpher and R. C. Herman. Remarks on the Evolution of the Expanding Universe. *Phys. Rev.*, 75(7):1089–1095, 1949.

[21] D. J. Fixsen and J. C. Mather. The Spectral Results of the Far-Infrared Absolute Spectrophotometer Instrument on COBE. *Astrophys. J.*, 581:817–822, 2002.

[22] A. A. Starobinsky. A new type of isotropic cosmological models without singularity. *Phys. Lett. B*, 91:99–102, 1980.

[23] A. H. Guth. Inflationary universe: A possible solution to the horizon and flatness problems. *Phys. Rev. D*, 23(2):347–356, 1981.

[24] A. D. Linde. A new inflationary universe scenario: A possible solution of the horizon, flatness, homogeneity, isotropy and primordial monopole problems. *Phys. Lett. B*, 108: 389–393, 1982.

[25] A. A. Starobinsky. Dynamics of Phase Transition in the New Inflationary Universe Scenario and Generation of Perturbations. *Phys. Lett. B*, 117:175–178, 1982.

[26] A. H. Guth and S.-Y. Pi. Fluctuations in the New Inflationary Universe. *Phys. Rev. Lett.*, 49(15):1110–1113, 1982.

[27] J. M. Bardeen, P. J. Steinhardt, and M. S. Turner. Spontaneous creation of almost scale-free density perturbations in an inflationary universe. *Phys. Rev. D*, 28(4):679–693, 1983.

[28] V. Bromm and N. Yoshida. The First Galaxies. *Ann. Rev. Astron. Astrophys.*, 49:373–407, arXiv:1102.4638, 2011.

[29] M. Zaldarriaga. Polarization of the microwave background in reionized models. *Phys. Rev. D*, 55:1822–1829, astro-ph/9608050, 1997.

[30] A. Kogut, et al. First-Year Wilkinson Microwave Anisotropy Probe (WMAP) Observations: Temperature-Polarization Correlation. *Astrophys. J. Suppl. Ser.*, 148:161–173, astro-ph/0302213, 2003.

[31] F. Zwicky. Die Rotverschiebung von extragalaktischen Nebeln. *Helv. Phys. Acta*, 6: 110–127, 1933.

[32] V. C. Rubin and W. K. Ford, Jr. Rotation of the Andromeda Nebula from a Spectroscopic Survey of Emission Regions. *Astrophys. J.*, 159:379, 1970.

[33] A. G. Riess et al. Observational evidence from supernovae for an accelerating universe and a cosmological constant. *Astron. J.*, 116:1009–1038, astro-ph/9805201, 1998.

[34] S. Perlmutter et al. Measurements of Omega and Lambda from 42 high redshift supernovae. *Astrophys. J.*, 517:565–586, astro-ph/9812133, 1999.

[35] D. J. Fixsen. The Temperature of the Cosmic Microwave Background. *Astrophys. J.*, 707:916–920, arXiv:0911.1955, 2009.

[36] Planck Collaboration: R. Adam et al. Planck 2015 results. I. Overview of products and scientific results. *ArXiv e-prints*, arXiv:1502.01582, 2015.

[37] M. J. Rees. Polarization and Spectrum of the Primeval Radiation in an Anisotropic Universe. *Astrophys. J. Lett.*, 153:L1– L5, 1968.

[38] J. D. Jackson. *Classical electrodynamics; 3rd ed.* Wiley, New York, NY, 1999.

[39] W. Hu and M. White. A CMB polarization primer. *New Astron.*, 2:323–344, astro-ph/9706147, 1997.

[40] M. Zaldarriaga and U. Seljak. All-sky analysis of polarization in the microwave background. *Phys. Rev. D*, 55(4):1830–1840, 1997.

[41] M. Kamionkowski, A. Kosowsky, and A. Stebbins. Statistics of cosmic microwave background polarization. *Phys. Rev. D*, 55(12):7368–7388, 1997.

[42] Planck Collaboration: P. A. R. Ade, et al. Planck 2013 results. I. Overview of products and scientific results. *Astron. Astrophys.*, 571:A1, arXiv:1303.5062, 2014.

[43] Y. B. Zeldovich and R. A. Sunyaev. The Interaction of Matter and Radiation in a Hot-Model Universe. *Astrophys. Space Sci.*, 4:301–316, 1969.

[44] R. A. Sunyaev and I. B. Zeldovich. Microwave background radiation as a probe of the contemporary structure and history of the universe. *Ann. Rev. Astron. Astrophys.*, 18: 537–560, 1980.

[45] J. E. Carlstrom, G. P. Holder, and E. D. Reese. Cosmology with the Sunyaev-Zel'dovich Effect. *Ann. Rev. Astron. Astrophys.*, 40:643–680, astro-ph/0208192, 2002.

[46] J. C. Mather, D. J. Fixsen, R. A. Shafer, C. Mosier, and D. T. Wilkinson. Calibrator design for the COBE far infrared absolute spectrophotometer (FIRAS). *Astrophys. J.*, 512:511–520, 1999.

[47] M. Kaplinghat, et al. Probing the Reionization History of the Universe using the Cosmic Microwave Background Polarization. *Astrophys. J.*, 583:24–32, astro-ph/0207591, 2003.

[48] M. J. Rees and D. W. Sciama. Large-scale Density Inhomogeneities in the Universe. *Nature*, 217:511–516, 1968.

[49] R. G. Crittenden and N. Turok. Looking for a Cosmological Constant with the Rees-Sciama Effect. *Phys. Rev. Lett.*, 76:575–578, astro-ph/9510072, 1996.

[50] A. Lewis and A. Challinor. Weak gravitational lensing of the CMB. *Phys. Rep.*, 429: 1–65, astro-ph/0601594, 2006.

[51] Planck Collaboration: P. A. R. Ade, et al. Planck 2015 results. XV. Gravitational lensing. *ArXiv e-prints*, arXiv:1502.01591, 2015.

[52] C. L. Bennett, et al. Nine-year Wilkinson Microwave Anisotropy Probe (WMAP) Observations: Final Maps and Results. *Astrophys. J. Suppl. Ser.*, 208:20, arXiv:1212.5225, 2013.

[53] S. Dodelson. *Modern Cosmology*. Academic Press, 2003.

[54] J. Delabrouille and J.-F. Cardoso. Diffuse source separation in CMB observations. *ArXiv e-prints*, astro-ph/0702198, 2007.

[55] C. L. Bennett, et al. First-Year Wilkinson Microwave Anisotropy Probe (WMAP) Observations: Foreground Emission. *Astrophys. J. Suppl. Ser.*, 148:97–117, astro-ph/0302208, 2003.

[56] D. Samtleben, S. Staggs, and B. Winstein. The Cosmic Microwave Background for Pedestrians: A Review for Particle and Nuclear Physicists. *Ann. Rev. Nuc. Par. Sci.*, 57: 245–283, arXiv:0803.0834, 2007.

[57] J. Dunkley, et al. Prospects for polarized foreground removal. In *American Institute of Physics Conference Series*, volume 1141, pages 222–264, arXiv:0811.3915, 2009.

[58] M. López-Caniego, et al. Polarization of the WMAP Point Sources. *Astrophys. J.*, 705: 868–876, arXiv:0909.4311, 2009.

[59] E. K. Conklin. Velocity of the Earth with Respect to the Cosmic Background Radiation. *Nature*, 222:971–972, 1969.

[60] P. S. Henry. Isotropy of the 3 K Background. *Nature*, 231:516–518, 1971.

[61] B. E. Corey and D. T. Wilkinson. A Measurement of the Cosmic Microwave Background Anisotropy at 19 GHz. In *Bulletin of the American Astronomical Society*, volume 8, page 351, 1976.

[62] J. C. Mather. The Cosmic Background Explorer (COBE). *Opt. Eng.*, 21:769–774, 1982.

[63] P. de Bernardis, et al. A flat Universe from high-resolution maps of the cosmic microwave background radiation. *Nature*, 404:955–959, astro-ph/0004404, 2000.

[64] R. Stompor, et al. Cosmological Implications of the MAXIMA-1 High-Resolution Cosmic Microwave Background Anisotropy Measurement. *Astrophys. J.*, 561:L7–L10, astro-ph/0105062, 2001.

[65] E. M. Leitch, et al. Experiment Design and First Season Observations with the Degree Angular Scale Interferometer. *Astrophys. J.*, 568:28–37, astro-ph/0104488, 2002.

[66] C. L. Bennett, et al. The Microwave Anisotropy Probe Mission. *Astrophys. J.*, 583: 1–23, astro-ph/0301158, 2003.

[67] C. L. Bennett, et al. First-Year Wilkinson Microwave Anisotropy Probe (WMAP) Observations: Preliminary Maps and Basic Results. *Astrophys. J. Supp.*, 148:1–27, astro-ph/0302207, 2003.

[68] D. N. Spergel, et al. Three-Year Wilkinson Microwave Anisotropy Probe (WMAP) Observations: Implications for Cosmology. *Astrophys. J. Supp.*, 170:377–408, astro-ph/0603449, 2007.

[69] G. Hinshaw, et al. Five-Year Wilkinson Microwave Anisotropy Probe Observations: Data Processing, Sky Maps, and Basic Results. *Astrophys. J. Supp.*, 180:225–245, arXiv:0803.0732, 2009.

[70] N. Jarosik, et al. Seven-year Wilkinson Microwave Anisotropy Probe (WMAP) Observations: Sky Maps, Systematic Errors, and Basic Results. *Astrophys. J. Supp.*, 192:14, arXiv:1001.4744, 2011.

[71] G. Hinshaw, et al. Nine-year Wilkinson Microwave Anisotropy Probe (WMAP) Observations: Cosmological Parameter Results. *Astrophys. J. Supp.*, 208:19, arXiv:1212.5226, 2013.

[72] D. S. Swetz, et al. Overview of the Atacama Cosmology Telescope: Receiver, Instrumentation, and Telescope Systems. *Astrophys. J. Supp*, 194:41, arXiv:1007.0290, 2011.

[73] J. E. Carlstrom, et al. The 10 Meter South Pole Telescope. *Publ. Astron. Soc. Pacific*, 123:568–581, arXiv:0907.4445, 2011.

[74] J. M. Kovac, et al. Detection of polarization in the cosmic microwave background using DASI. *Nature*, 420:772–787, astro-ph/0209478, 2002.

[75] D. J. Fixsen, et al. The Cosmic Microwave Background Spectrum from the Full COBE FIRAS Data Set. *Astrophys. J.*, 473:576, astro-ph/9605054, 1996.

[76] A. Kogut, et al. The Primordial Inflation Explorer (PIXIE): a nulling polarimeter for cosmic microwave background observations. *J. Cosmol. Astropart. Phys.*, 7:025, arXiv:1105.2044, 2011.

[77] B. Gold, et al. Seven-year Wilkinson Microwave Anisotropy Probe (WMAP) Observations: Galactic Foreground Emission. *Astrophys. J. Suppl.*, 192:15, arXiv:1001.4555, 2011.

[78] J. R. Hinderks, et al. QUaD: A High-Resolution Cosmic Microwave Background Polarimeter. *Astrophys. J.*, 692:1221–1246, arXiv:0805.1990, 2009.

[79] D. Hanson, et al. Detection of B-Mode Polarization in the Cosmic Microwave Background with Data from the South Pole Telescope. *Phys. Rev. Lett.*, 111(14):141301, arXiv:1307.5830, 2013.

[80] Z. D. Kermish, et al. The POLARBEAR experiment. In *Millimeter, Submillimeter, and Far-Infrared Detectors and Instrumentation for Astronomy VI*, volume 8452 of *Proc. of the SPIE*, page 84521C, arXiv:1210.7768, 2012.

[81] The Polarbear Collaboration: P. A. R. Ade, et al. A Measurement of the Cosmic Microwave Background B-mode Polarization Power Spectrum at Sub-degree Scales with POLARBEAR. *Astrophys. J.*, 794:171, arXiv:1403.2369, 2014.

[82] R. W. Ogburn IV, et al. The BICEP2 CMB polarization experiment. In *Millimeter, Submillimeter, and Far-Infrared Detectors and Instrumentation for Astronomy V*, volume 7741 of *Proc. of the SPIE*, page 77411G, 2010.

[83] BICEP2 Collaboration: P. A. R. Ade, et al. Detection of B-Mode Polarization at Degree Angular Scales by BICEP2. *Phys. Rev. Lett.*, 112(24):241101, arXiv:1403.3985, 2014.

[84] J. A. Tauber, et al. Planck pre-launch status: The Planck mission. *Astron. Astrophys.*, 520:A1, 2010.

[85] M. Bersanelli, et al. Planck pre-launch status: Design and description of the Low Frequency Instrument. *Astron. Astrophys.*, 520:A4, arXiv:1001.3321, 2010.

[86] X. Dupac and J. Tauber. Scanning strategy for mapping the Cosmic Microwave Background anisotropies with Planck. *Astron. Astrophys.*, 430:363–371, astro-ph/0409405, 2005.

[87] K. M. Górski, et al. HEALPix: A Framework for High-Resolution Discretization and Fast Analysis of Data Distributed on the Sphere. *Astrophys. J.*, 622:759–771, astro-ph/0409513, 2005.

[88] Planck Collaboration: P. A. R. Ade, et al. Planck 2015 results. III. LFI systematic uncertainties. *ArXiv e-prints*, arXiv:1507.08853, 2015.

[89] Planck Collaboration: R. Adam, et al. Planck 2015 results. VII. HFI TOI and beam processing. *ArXiv e-prints*, arXiv:1502.01586, 2015.

[90] J. P. Leahy, et al. Planck pre-launch status: Expected LFI polarisation capability. *Astron. Astrophys.*, 520:A8, 2010.

[91] J. Delabrouille. Analysis of the accuracy of a destriping method for future cosmic microwave background mapping with the PLANCK SURVEYOR satellite. *Astron. Astrophys. Supp. Ser.*, 127:555–567, 1998.

[92] Planck Collaboration: P. A. R. Ade, et al. Planck 2015 results. XII. Full Focal Plane simulations. *ArXiv e-prints*, arXiv:1509.06348, 2015.

[93] Planck Collaboration: R. Adam, et al. Planck 2015 results. IX. Diffuse component separation: CMB maps. *ArXiv e-prints*, arXiv:1502.05956, 2015.

[94] Planck Collaboration: R. Adam, et al. Planck 2015 results. X. Diffuse component separation: Foreground maps. *ArXiv e-prints*, arXiv:1502.01588, 2015.

[95] Planck Collaboration: N. Aghanim, et al. Planck 2015 results. XI. CMB power spectra, likelihoods, and robustness of parameters. *ArXiv e-prints*, arXiv:1507.02704, 2015.

[96] A. Lewis and S. Bridle. Cosmological parameters from CMB and other data: A Monte Carlo approach. *Phys. Rev. D*, 66(10):103511, astro-ph/0205436, 2002.

[97] Planck Collaboration: P. A. R. Ade, et al. Planck early results. I. The Planck mission. *Astron. Astrophys.*, 536:A1, arXiv:1101.2022, 2011.

[98] BICEP2/Keck and Planck Collaborations: P. A. R. Ade, et al. Joint Analysis of BICEP2/Keck Array and Planck Data. *Phys. Rev. Lett.*, 114(10):101301, arXiv:1502.00612, 2015.

[99] C. G. T. Haslam, C. J. Salter, H. Stoffel, and W. E. Wilson. A 408 MHz all-sky continuum survey. II - The atlas of contour maps. *Astron. Astrophys. Supp. Ser.*, 47:1, 1982.

[100] Planck Collaboration: R. Adam, et al. Planck intermediate results. XXX. The angular power spectrum of polarized dust emission at intermediate and high Galactic latitudes. *Astron. Astrophys.*, 586:A133, 2016.

[101] P. A. R. Ade, et al. Improved Constraints on Cosmology and Foregrounds from BICEP2 and Keck Array Cosmic Microwave Background Data with Inclusion of 95 GHz Band. *Phys. Rev. Lett.*, 116(3):031302, 1510.09217, 2016.

[102] C. Armitage and B. D. Wandelt. Deconvolution map-making for cosmic microwave background observations. *Phys. Rev. D*, 70(12):123007, astro-ph/0410092, 2004.

[103] C. Armitage-Caplan and B. D. Wandelt. PReBeaM for Planck: A Polarized Regularized Beam Deconvolution Map-Making Method. *Astrophys. J. Suppl. Ser.*, 181:533–542, arXiv:0807.4179, 2009.

[104] D. L. Harrison, F. van Leeuwen, and M. A. J. Ashdown. A deconvolution map-making method for experiments with circular scanning strategies. *Astron. Astrophys.*, 532:A55, arXiv:1106.4237, 2011.

[105] E. Keihänen and M. Reinecke. ArtDeco: a beam-deconvolution code for absolute cosmic microwave background measurements. *Astron. Astrophys.*, 548:A110, arXiv:1208.1399, 2012.

[106] J. Borrill. MADCAP - The Microwave Anisotropy Dataset Computational Analysis Package. *ArXiv e-prints*, astro-ph/9911389, 1999.

[107] M. Tegmark. How to Make Maps from Cosmic Microwave Background Data without Losing Information. *Astrophys. J. Lett.*, 480:L87–L90, astro-ph/9611130, 1997.

[108] A. Kogut, et al. Calibration and Systematic Error Analysis for the COBE DMR 4 Year Sky Maps. *Astrophys. J*, 470:653, astro-ph/9601066, 1996.

[109] R. Dünner, et al. The Atacama Cosmology Telescope: Data Characterization and Map-making. *Astrophys. J.*, 762:10, arXiv:1208.0050, 2013.

[110] C. Burigana, et al. A preliminary study on destriping techniques of PLANCK/LFI measurements versus observational strategy. *ArXiv e-prints*, astro-ph/9906360, 1999.

[111] D. Maino, et al. The Planck-LFI instrument: Analysis of the 1/f noise and implications for the scanning strategy. *Astron. Astrophys. Supp. Ser.*, 140:383–391, astro-ph/9906010, 1999.

[112] D. Maino, C. Burigana, K. M. Górski, N. Mandolesi, and M. Bersanelli. Removing 1/f noise stripes in cosmic microwave background anisotropy observations. *Astron. Astrophys.*, 387:356–365, astro-ph/0202271, 2002.

[113] E. Keihänen, H. Kurki-Suonio, T. Poutanen, D. Maino, and C. Burigana. A maximum likelihood approach to the destriping technique. *Astron. Astrophys.*, 428:287–298, 2004.

[114] W. Press, S. Teukolsky, W. Vetterling, and B. Flannery. *Numerical Recipes in Fortran 77: the Art of Scientific Computing. Second Edition*. Cambridge University Press, 1992.

[115] E. Keihänen, H. Kurki-Suonio, and T. Poutanen. MADAM- a map-making method for CMB experiments. *Mon. Not. R. Astron. Soc.*, 360:390–400, astro-ph/0412517, 2005.

[116] R. Keskitalo, et al. Residual noise covariance for Planck low-resolution data analysis. *Astron. Astrophys.*, 522:A94, arXiv:0906.0175, 2010.

[117] Anthony Challinor, et al. All-sky convolution for polarimetry experiments. *Phys. Rev. D*, 62:123002, 2000.

[118] K. Benabed, J.-F. Cardoso, S. Prunet, and E. Hivon. TEASING: a fast and accurate approximation for the low multipole likelihood of the cosmic microwave background temperature. *Mon. Not. R. Astron. Soc.*, 400:219–227, arXiv:0901.4537, 2009.

[119] Planck Collaboration: N. Aghanim, et al. Planck 2015 results. XXII. A map of the thermal Sunyaev-Zeldovich effect. *ArXiv e-prints*, arXiv:1502.01596, 2015.